IMPROVED POSITIVE ELECTRODE MATERIALS FOR Li-ION BATTERIES: EXPLORING THE HIGH SPECIFIC CAPACITY OF $LiCoO_2$ AND THE HIGH RATE CAPABILITY OF $LiFePO_4$

by

Zhaohui Chen

Submitted in partial fulfillment of the requirements
for the degree of Doctor of Philosophy

at

Dalhousie University
Halifax, Nova Scotia
August 2003

Your file Votre référence
ISBN: 0-612-83699-1
Our file Notre référence
ISBN: 0-612-83699-1

DALHOUSIE UNIVERSITY

DEPARTMENT OF PHYSICS AND ATMOSPHERIC SCIENCE

The undersigned hereby certify that they have read and recommend to the Faculty of Graduate Studies for acceptance a thesis entitled "Improved Positive Electrode Materials For Li-Ion Batteries: Exploring The High Specific Capacity Of $LiCoO_2$ And The High Rate Capability Of $LiFePO_4$" by Zhaohui Chen in partial fulfillment for the degree of Doctor of Philosophy.

Dated: August 20, 2003

External Examiner:

Research Supervisor:

Examining Committee:

Departmental Representative:

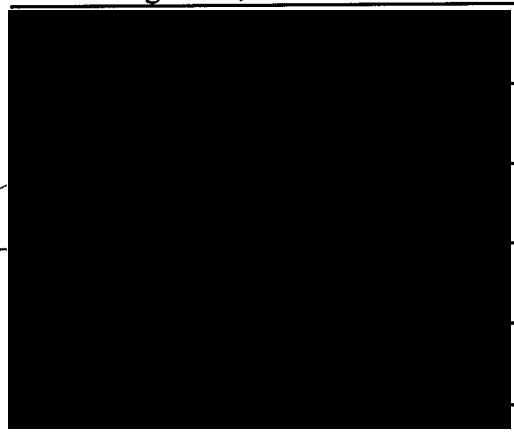

DALHOUSIE UNIVERSITY

DATE: August 20, 2003

AUTHOR: Zhaohui Chen

TITLE: IMPROVED POSITIVE ELECTRODE MATERIALS FOR Li-ION BATTERIES:
EXPLORING THE HIGH SPECIFIC CAPACITY OF $LiCoO_2$
AND THE HIGH RATE CAPABILITY OF $LiFePO_4$

DEPARTMENT OR SCHOOL: The Department of Physics and Atmospheric Science

DEGREE: Ph.D. CONVOCATION: October YEAR: 2003

Permission is herewith granted to Dalhousie University to circulate and to have copied for non-commercial purposes, at its discretion, the above title upon the request of individuals or institutions.

Signature of Author

Table of Contents

List of Figures

List of Tables

Abstract

During the past decade, the search for better electrode materials for Li-ion batteries has been of a great commercial interest, especially since Li-ion technology has become a major rechargeable battery technology with a market value of $3 billion US dollars per year. This thesis focuses on improving two positive electrode materials: one is a traditional positive electrode material—$LiCoO_2$; the other is a new positive electrode material—$LiFePO_4$.

Cho *et al.* reported that coating $LiCoO_2$ with oxides can improve the capacity retention of $LiCoO_2$ cycled to 4.4 V. The study of coatings in this thesis confirms this effect and shows that further improvement (30% higher energy density than that used in a commercial cell with excellent capacity retention) can be obtained. An *in-situ* XRD study proves that the mechanism of the improvement in capacity retention by coating proposed by Cho *et al.* is incorrect. Further experiments identify the suppression of impedance growth in the cell as the key reason for the improvement caused by coating. Based on this, other methods to improve the energy density of $LiCoO_2$, without sacrificing capacity retention, are also developed.

Using an XRD study, the structure of the phase between the O3-phase $Li_{1-x}CoO_2$ ($x>0.5$) and the O1 phase CoO_2 was measured experimentally for the first time. XRD results confirmed the prediction of an H1-3 phase by Ceder's group. Apparently, because of the structural changes between the O3 phase and the H1-3 phase, good capacity retention cannot be attained for cycling $LiCoO_2$ to 4.6 V with respect to Li metal.

An effort was also made to reduce the carbon content in a $LiFePO_4$/C composite without sacrificing its rate capability. It was found that about 3% carbon by weight maintains both a good rate capability and a high pellet density for the composite.

List of Symbols and Abbreviations Used

a, *c* — Lattice Constant

AES — Auger Electron Spectroscopy

DBP — Dibutylpthalate

DEC — Diethylcarbonate

dQ/dV — Differential Capacity

EC — Ethylene Carbonate

EDS — Energy Dispersive Spectrometer

EV — Electric Vehicle

HEV — Hybrid Electric Vehicle

HFP — Hexafluoropropylene

ICP/MS — Inductively Coupled Plasma/Mass Spectrometry

LiBOB — Lithium Bis(oxalato)borate

MCMB — mesocarbon microbeads

NMP — N-methylpyrrolidinone

PVDF — Polyvinylidene Fluoride

SEM — Scanning Electron Microscopy

TEM — Transmission Electron Microscopy

TGA — Thermogravimetric Analysis

v/v — Volumetric Ratio

XRD — X-ray Diffraction

Acknowledgements

It have been a great experience for me to persue my Ph.D. in such a great group and in such an interesting field. In addition to my effort, guidance and help from many individuals were essential to the smooth completion of this thesis.

First of all, I would like to thank Professor Jeff Dahn, my supervisor. It has been a privilege to share excitements and puzzles with such a talented and dedicated scientist through the research. He has widened my view in so many ways. For example, during the last three years, I have learned a how deep insight can be gained from simple experiments; I have learned how important it is to give criticism when deserved; I have also learned how efficient moving can be if I have a helper who is a physicist and a soccer player. Jeff, you are a great supervisor!

Second, I would like to thank members of Dahn Lab. in the past three years. They are Dr. David Stevens, Jennifer Seel, Dr. Luc Beaulieu, Jason Meuller-Neuhaus, Dr. Dean McNeil, Tim Hatchard, Shane Beattie, Dr. Zhonghua Lu, Dr. Kevin Hewitt, Arman Bonakdarpour, Zonghai Chen, Hubert Fortier, Dr. Shugao Zhang, Mike Fleischauer, Dr. Severine Jouanneau, Junwei Jiang, Adam Timmons, Dr. Jun Chen, and Toni Abdo, Aaron Barkhouse, and other summer students. Working with you has been so much fun and there has always been so much to gain. I have learned from you to be open, patient, and helpful. Thank you all for your help.

Third, I would like to thank Professors Richard Dunlap and Sarah Wells for serving as my supervisory committee member. Also, I thank Professors Richard Dunlap and Ian Folkins for helping me in their roles as graduate coordinator and Professor Michael A. Gharghouri for helping me with SEM experiments.

Fourth, I would like to thank staff in the department of physics: Judy Hollett, Anne-Marie Jeffrey, Anne Murphy, Simon Trussler, Alex Feargrieve, and Jim Chisholm.

Special thanks go to Andy George for his continuous technical help and to Barbara Gauvin for her lessons in our lunch time ESL club.

Also, I would like to thank Dalhousie University for providing me with such a great education. And I thank NSERC and 3M corporation for funding the research.

In addition, I would like to thank people from outside of the university, who have helped my family and I. All volunteers through International Student Ministry, Atlantic Inter-Varsity Christian Fellowship, thank you for making us feel at home in Halifax and making this three years so enjoyable for us. There are many names to mention: Monique Watt, Dr. Dorette Pronk, Betty Scholfield, Dr. Steven Martin, David Hopper, Janet Hopper, Susan Page etc.

Finally, I would like to thank my family for their continuous love and support.

Chapter 1 Introduction

1.1 Importance of battery development

Energy storage and information technology are key areas of technological development today. They both demand advanced battery technologies.

Portable devices are becoming cheaper, lighter, smaller, and have increased functionality. More people around the world now enjoy a convenient life style using cellular phones, laptop computers, video cameras, and other devices. This would not have happened if there had been no breakthroughs in information technology or electronic engineering. However, it would be unfair to under-estimate the important contribution of advanced battery technology. Portable devices with increased functionality require batteries of larger energy. However, this energy must be packed efficiently because the size and weight of the devices keeps decreasing to make them more convenient. Therefore, the market demands the maximum energy per unit volume (volumetric energy density) or energy per unit weight (specific energy) of batteries used for portable power.

Environmental pollution and the energy crisis are attracting more attention worldwide. One solution to these problems would be to reduce fossil fuel consumption. Automobiles use about 1/3 of the fossil fuels produced and are a major pollution source. In many developed countries, great effort has been made to reduce automobile fuel consumption and greenhouse gas emission. The recently introduced hybrid electric vehicle (HEV), which combines a small internal combustion engine and a rechargeable battery, has been a big step forward. The HEV has the potential to double the energy efficiency of a normal vehicle. Furthermore, to completely eliminate greenhouse gas

emission and pollution from the vehicle itself, the electric vehicle (EV) has also been proposed and is under development. Both the EV and the HEV need batteries with high energy density, in order to minimize the size and weight of the battery and the automobile.

An enormous amount of research and development has been conducted in the past two decades to search for high energy density batteries. New batteries such as nickel metal-hydride and Li-ion were introduced and have become more popular choices than other technologies, such as Ni-Cd. However, since the demand for better batteries will not end, neither will battery research and development. This thesis describes my efforts to develop and understand better electrode materials for Li-ion batteries.

1.2 Electrochemistry of Li-ion batteries

Li-ion batteries have the largest energy density of all rechargeable batteries and have become the most popular choice as a portable power supply. They are also under development for HEV and EV applications. A Li-ion cell consists of a carbon-based negative electrode (usually graphite), a lithium transition metal oxide positive electrode (usually $LiCoO_2$) and an organic electrolyte with a dissolved lithium salt. During charge, lithium atoms are extracted from the positive electrode material and inserted into the negative electrode material. During discharge, the reverse process takes place. Hence, as shown in Figure1.1, the basic electrochemistry of the cell involves only the transfer of lithium atoms between the two electrodes, the ions through the electrolyte and the corresponding electrons through the external current. The electrochemical charge/discharge reactions can be represented by equations (1) and (2),

At the positive electrode:

$$LiMO_2 \underset{\text{discharge}}{\overset{\text{charge}}{\rightleftharpoons}} Li_{1-x}MO_2 + xLi^+ + xe^- \qquad (1)$$

At the negative electrode

$$C + xLi^+ + xe^- \underset{\text{discharge}}{\overset{\text{charge}}{\rightleftharpoons}} Li_xC \qquad (2)$$

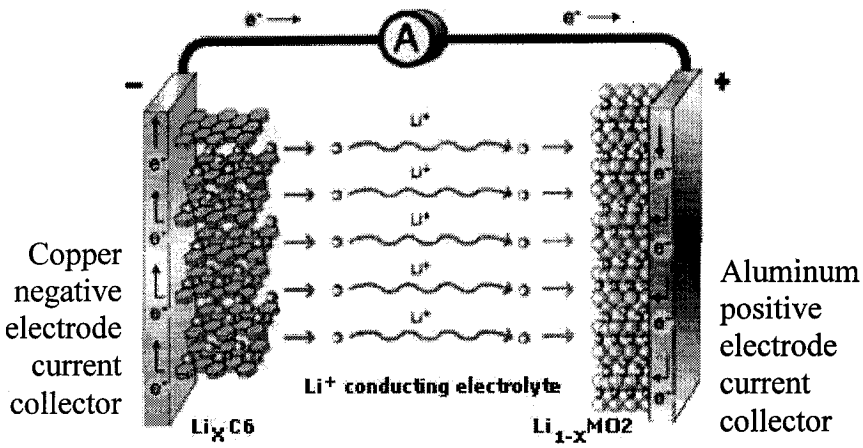

Figure 1.1 Schematic illustration of a Li-ion Cell.
(www.agmbat.co.uk/liiontechnology.html)

1.3 Advantages and disadvantages of Li-ion batteries

As mentioned in 1.2, the specific energy of Li-ion batteries is much larger than those of other rechargeable battery technologies. This is mainly due to the high average cell voltage of about 4 V. Other rechargeable batteries have an average cell voltage between 1.2 and 2 V. Figure 1.2 shows a comparison of the energy density of commercialized rechargeable batteries.

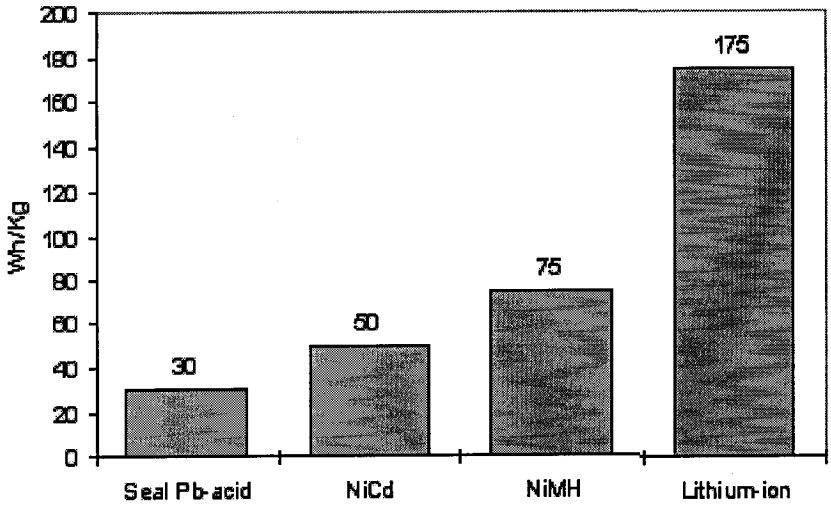

Figure 1.2 Comparison of the specific energy of different types of rechargeable batteries (www.etvi.org/High_Tech/New_Electric_HiTech_right.html).

In addition, Li-ion batteries have other outstanding properties, such as excellent cycle life, high charge/discharge rates, wide operating temperature range, low self-discharge rate and no memory effect.

High cost had been one of the disadvantages of the Li-ion technologies. However, because of the economics of scale, the price for Li-ion batteries has dropped significantly. At present, the cost per Whr for Li-ion is the same as that for Ni-MH and Ni-Cd batteries (Takeshita, 2003). If the price can be lowered further, Li-ion batteries can further dominate the market for small rechargeable batteries.

One disadvantage of Li-ion technology is poor safety of large cells. A Li-ion cell consists, simply speaking, of two active electrodes separated by a polymeric separator, surrounded by an organic electrolyte solution. The active electrodes, in the charged state, have been shown previously to partake in exothermic reactions at elevated temperatures encountered during abuse situations (e.g. crushing) (Matthews, 2000). The heat from

these reactions can be dissipated to the environment for small cells (<2.5Ahr) but larger cells can encounter thermal runaway when heat production exceeds dissipation.

1.4 Trends for positive electrode material development

To expand the Li-ion battery market further, its main disadvantages must be overcome. The positive electrode is partially responsible for the safety and cost of the whole cell. Consequently, researchers have been developing cheaper and safer positive electrode materials, such as $LiMn_2O_4$ (Thackeray *et al.*, 1992), $Li(Co_{1-x}Ni_x)O_2$ (Caurant *et al.*, 1996), $Li[Ni_xLi_{(1/3-2x/3)}Mn_{(2/3-x/3)}]O_2$ (Lu, 2002), $Li[Ni_xCo_{1-2x}Mn_x]O_2$ (Lu *et al.*, 2001), $LiFePO_4$ (Yamada *et al.*, 2001), etc. In addition, surface modification of $LiCoO_2$ has been reported to help increase its energy density without sacrificing cycle life (Cho *et al.*, 2000a). This thesis reports efforts to improve the specific energy of $LiFePO_4$ during high rate cycling and to develop $LiCoO_2$ with higher specific energy and excellent cycling behavior. The following two sections give background information for these two projects.

1.5 Surface coatings on $LiCoO_2$ positive electrode material

$LiCoO_2$ has been used as the dominant positive electrode material by all major Li-ion cell manufacturers because of its good rate capability and cycling stability. The reversible capacity of $LiCoO_2$ is about 140 mAh/g even though its theoretical capacity is 272 mAh/g. Some researchers believe that because of an instability caused by phase transitions and accompanying lattice expansion, the reversible capacity of Li_xCoO_2 is limited to 140 mAh/g or between x=1 and x=0.5 (Wang *et al.*, 1999). If its reversible

capacity can be increased, its energy density will also increase. Then $LiCoO_2$ would be an even more attractive positive electrode material and higher energy density batteries could be made.

J. Cho *et al.* (2000a) first reported that the structural stability of Li_xCoO_2, when cycled to a value of $x<0.5$, could be improved by coating a metal oxide on the surface of $LiCoO_2$ particles. Their papers (Cho *et al.*, 2000a, 2000b, 2001a, 2001b) show that $LiCoO_2$ coated with metal oxides has high reversible capacity (about 170 mAh/g) and improved cycling behavior.

Figures 1.3, 1.4, and 1.5 are from one of Cho *et al.*'s (2001b) paper on coatings. Figure 1.3 shows that the initial capacity of coated $LiCoO_2$ is about 170 mAh/g when cycled between 2.75 and 4.4 V. For the un-coated sample shown in Figure 1.3, the capacity decreases so rapidly that only 100 mAh/g remains after 30 cycles. By contrast, samples coated with oxides by the sol-gel method have much better cycling stability. For the sample coated with ZrO_2, the capacity does not decrease over the first 70 cycles (Cho *et al.*, 2001b). Figure 1.4 shows the change of the lattice constant, c, of these samples during a charge as measured by X-ray diffraction. Figure 1.4 shows that better cycling stability corresponds to smaller lattice expansion along the *c*-axis. For the sample coated with ZrO_2, the unit cell hardly expands at all along the *c*-axis during a charge (Cho *et al.*, 2001b).

There are no diffraction peaks from the metal oxides in the X-ray diffraction patterns of the coated samples. From Auger Electron Spectroscopy (AES) analysis, as shown in Figure 1.5, the concentration of Al (for coating with alumina) decreases with depth from the surface and reaches a depth of about 1 μm. According to Cho *et al.*

(2001b), the coated oxide reacts with $LiCoO_2$ and forms a layer of $LiCo_{1-x}Al$(or Zr, Ti, $B)_xO_2$. This very thin layer of $LiCo_{1-x}Al$(or Zr, Ti, $B)_xO_2$ supposedly suppresses the expansion of Li_xCoO_2 during cycling between 2.75 and 4.4 V. If the oxide used for coating has larger fracture toughness, the surface layer resulting from the coating is assumed to be stronger and then the coating improves the cycling more. The fracture toughness of the oxides decreases as ZrO_2>Al_2O_3>TiO_2>B_2O_3, so that the ZrO_2 coating is the most effective according to Cho *et al.* (2001b). This idea is illustrated by Figure 1.6.

As shown in Figure 1.3, ZrO_2 coating increases the reversible capacity of $LiCoO_2$ by 20% compared to the 140 mAh/g now used. This improvement will have great impact on the Li-ion battery industry.

However, Cho *et al.*'s explanation of the mechanism is difficult to believe (Cho *et al.*, 2001b). According to them, the thin film suppresses the expansion of $LiCoO_2$ during cycling. Normally, Li_xCoO_2 expands by 2.6% along the *c*-axis when x changes from 1 to 0.5. In order to suppress this strain, a stress must be applied to each Li_xCoO_2 particle. In the case of ZrO_2 coating on Li_xCoO_2, the ZrO_2 film must supply the needed stress. Based on Hooke's law, stress is proportional to strain. The ZrO_2 coating cannot supply such a stress unless it also undergoes a strain. Therefore, it is very hard to understand how the strain in Li_xCoO_2 could be completely eliminated by a thin coating. In addition, will $LiCo_{1-y}M_yO_2$ (M=Zr, Al, Ti, B) (if it exists) have the same fracture-toughness as an oxide of M?

Furthermore, $LiCoO_2$ particles do not expand further when charged above 4.2 V. As to the impact of the order-disorder phase transitions, $LiCoO_2$ undergoes a phase transition from a hexagonal phase to a monoclinic phase when charged to 4.2 V. Further

charging results in another phase transition from the monoclinic phase to a hexagonal phase. Does this additional phase transition alone cause the change in the cycling behavior of $LiCoO_2$ when the upper cutoff potential is increased from 4.2 to 4.4 V?

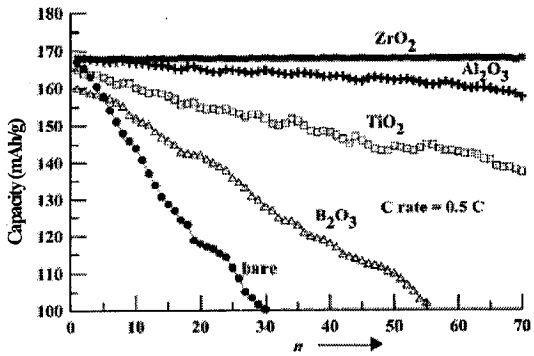

Figure 1.3 Cycle-life performances for ZrO_2, Al_2O_3, TiO_2, B_2O_3 coated, and un-coated (bare) $LiCoO_2$. The cells were cycled between 2.75 and 4.4 V at 21℃ (n: cycle number, x: discharge capacity) (Cho et al., 2001b).

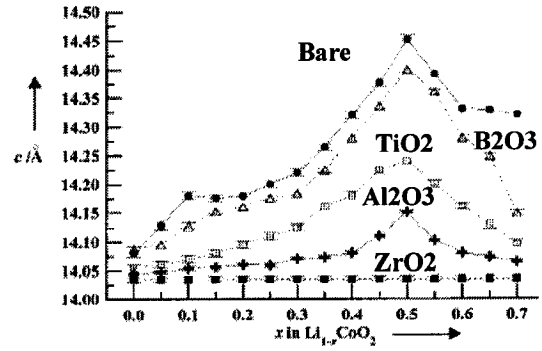

Figure 1.4 Lattice constant c in ZrO_2, Al_2O_3, TiO_2, B_2O_3 coated, and bare $LiCoO_2$ as a function of x in $Li_{1-x}CoO_2$ during the first charge (Cho et al., 2001b).

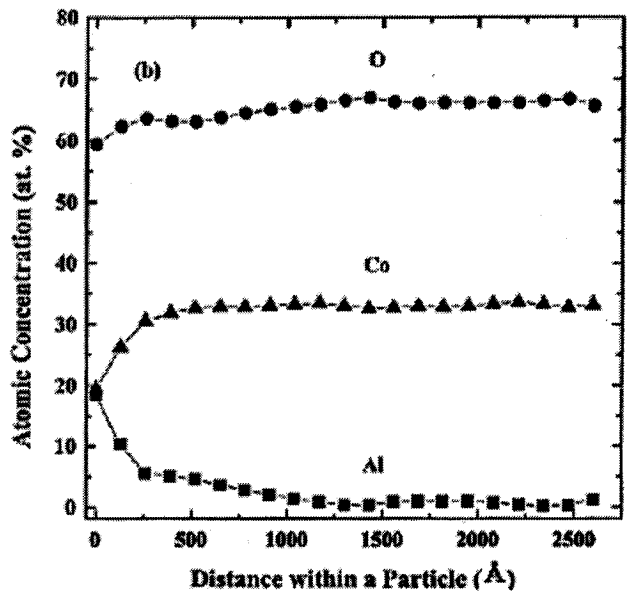

Figure 1.5 AES concentration profiles of an Al_2O_3 coated $LiCoO_2$ particle. The AES analysis was performed with an accelerating voltage of 10 KeV (Cho et al., 2000b).

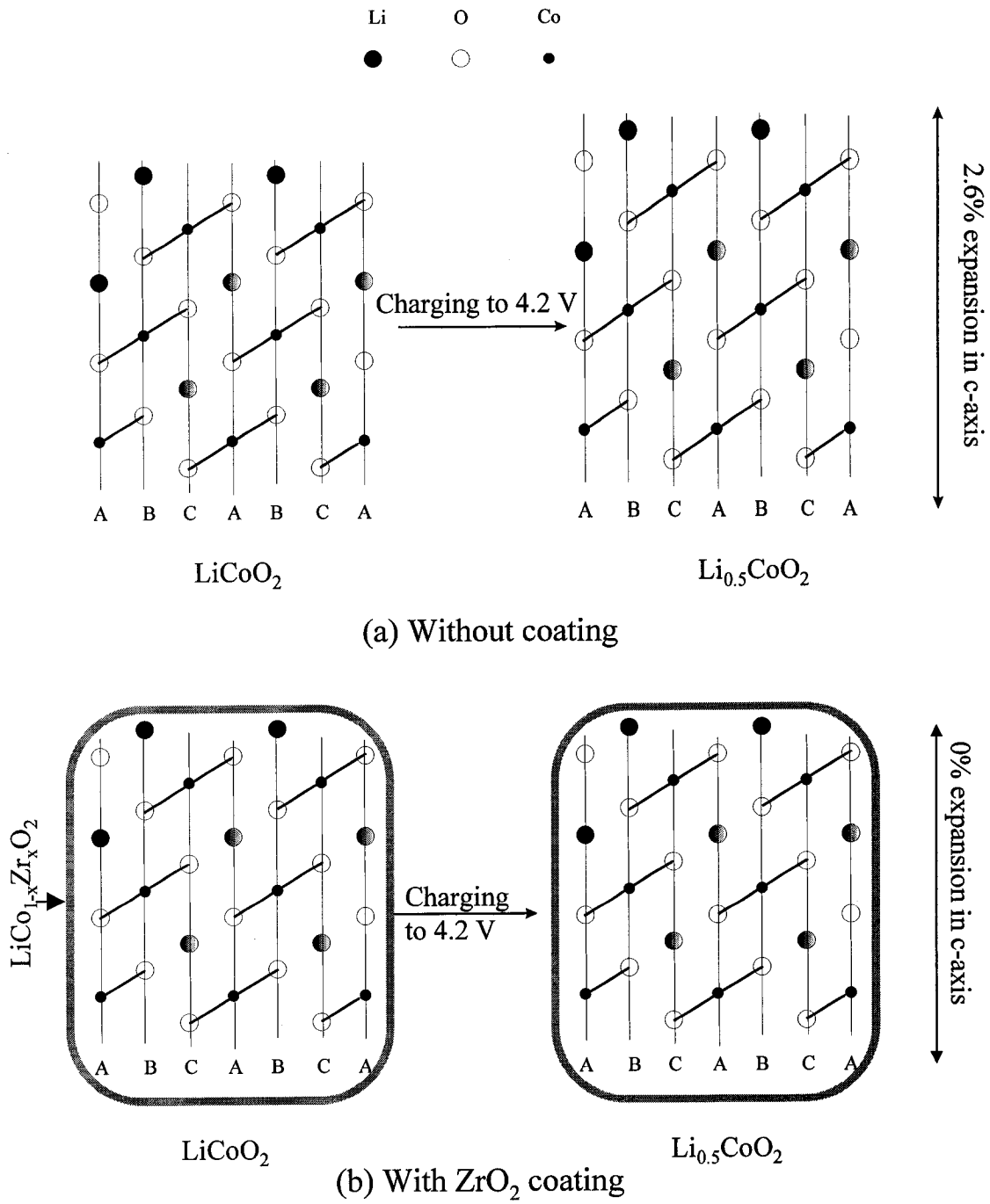

Figure 1.6 a) The expansion of lattice constant c (2.6%) in bare $LiCoO_2$ during charging (Li de-intercalation); b) the suppression of the lattice constant c expansion by a fracture-toughened thin-film metal-oxide coating.

For the reasons mentioned above, lattice expansion cannot be the reason for the poor cycling behavior of $LiCoO_2$ when it is cycled above 4.4 V. A possible reason could be side reactions between the electrolyte and the $LiCoO_2$ surface. Then it makes sense that a thin oxide film could suppress such a side reaction by physically separating the surface from the electrolyte.

After Cho's work, it is useful to explore the possibility of even higher reversible capacity in Li_xCoO_2. A better understanding of the mechanism for the improvement of the cycling behavior of $LiCoO_2$ by metal oxide coatings is also needed. With a better understanding, it may be possible to develop other methods to improve the energy density of Li_xCoO_2 and other positive electrode materials for Li ion batteries.

1.6 Improving the conductivity of $LiFePO_4$

$LiCoO_2$ is relatively expensive and many researchers are working to find a cheap, effective replacement for it. Padhi *et al.* (1997) reported that $LiFePO_4$ could be used as a positive electrode material and showed that it could have a reversible capacity of about 110 mAh/g at a potential of about 3.5 V versus Li metal when cycled using a very low current density. The theoretical capacity of $LiFePO_4$ is 169 mAh/g. Pahdi *et al.* (1997) suggested that the difference between experimental and theoretical capacities is caused by poor diffusion of lithium ions through $LiFePO_4/FePO_4$ interfaces. $LiFePO_4$ is believed to be cheaper and more stable than $LiCoO_2$, because it contains iron rather than cobalt and $FePO_4$ can be found in nature as a mineral. Therefore, efforts to understand and improve its electrochemical performance have continued since their report (Pahdi *et al.*, 1997).

N. Ravet *et al.* (1999) reported that $LiFePO_4$ had a capacity of about 160 mAh/g when cycled at a rate of 160 mA/g at 80°C after coating with about 1 wt% carbon. This

indicates that increasing the conductivity can improve the capacity significantly. This is not unexpected, because $LiFePO_4$ is an insulating phase. More recently, A. Yamada *et al.* (2001) achieved 95% of the theoretical capacity of $LiFePO_4$ using a current density of 0.12 mA/cm^2 at room temperature by sintering it at 550°C to make small particles. They believe that decreasing the particle size is an effective way to overcome the diffusion limitation problems.

Combining the ideas above, H. Huang *et al.* (2001) made $LiFePO_4$/C composites by mixing the raw materials with a carbon gel before sintering. In this composite, $LiFePO_4$ has a particle size of 100-200 nm and there is about 15 wt% carbon in the composite. This composite first demonstrated that $LiFePO_4$ could have excellent rate capability. Even when cycled at a 5C rate, it delivers a capacity of about 120 mAh/g. Huang *et al.* (2001) believe that both particle size minimization and intimate carbon contact are needed to optimize the rate capability of this material.

The diffusion limitation problem and the poor electrical conductivity of $LiFePO_4$ can be overcome by minimizing the particle size and introducing conductive additives. Therefore, it appears $LiFePO_4$ is almost an ideal positive electrode material. However, for practical applications, energy density, in addition to rate capability, is one of the most important characteristics of electrode materials. If the particle size is minimized, then the surface area of the material will be simultaneously maximized. Increasing the surface area will result in larger mass fractions of carbon needed to coat the particles to the same thickness. In Huang's case, 15 wt% carbon was incorporated in the $LiFePO_4$/C composite. Such a large amount of carbon decreases the energy density of the material significantly. Therefore, to make $LiFePO_4$ a suitable positive electrode material for

industrial application, efforts must be made to reduce the amount of carbon in $LiFePO_4$/C composites to a reasonably low level without sacrificing rate capability.

Part of this thesis will focus on coating $LiFePO_4$ with carbon. Some progress has been made mainly based on Ravet *et al.*'s approach (Ravet *et al.*, 2001).

1.7 **Scope of this thesis**

This thesis focuses on improving the electrochemical performance of $LiFePO_4$ and $LiCoO_2$ positive electrode materials for Li ion batteries. First, in Chapter 2, the experimental details of materials synthesis, characterization and electrochemical testing will be described. All the experimental results will be presented and discussed in Chapters 3 to 7. Chapter 3 shows the effects of different carbon coating methods on the capacity of $LiFePO_4$ when discharged at high rates. The effect of the amount of carbon used for coating on the rate capability and density are also studied. Chapter 4 shows the effect of oxide coatings on the capacity retention of $LiCoO_2$ when cycled to 4.5 V, as well as characterization of the coated materials by X-ray diffraction (XRD), Transmission Electron Microscopy (TEM) and Scanning Electron Microscopy (SEM). Chapter 5 focuses on understanding the improvement of the cycling behavior of $LiCoO_2$ after coating. Other methods to decrease the capacity fading are also developed. Chapter 6 shows the effect of SiO_2 addition to $LiPF_6$-based electrolyte on the capacity retention of $LiCoO_2$ in Li metal cells and in Li-ion cells. Chapter 7 describes an experiment identifying a staged phase of Li_xCoO_2 found at about 4.55 V. The importance of this staged phase to charging Li_xCoO_2 to above 4.5 V will be discussed. Conclusions and suggestions for future work will be presented in Chapter 8.

Chapter 2 Experimental Details

2.1 Synthesis of $LiFePO_4$ and coating $LiFePO_4$ with carbon

$LiFePO_4$ was prepared by a solid-state reaction between $FeC_2O_4 \bullet 2H_2O$, $(NH_4)_2HPO_4$ and Li_2CO_3. A stoichiometric mixture of the raw materials was mixed in a hardened stainless steel vial for 16 hrs by ball milling with a Spex-8000 mill. Hardened stainless steel balls were used and the ball to powder ratio was 3:1 by weight. The raw materials were weighed and put into the vial in an argon-filled glove box. The mixed powder was heated to 320°C for 12 hrs in argon to cause it to decompose. The decomposed mixture was then pressed into pellets under a pressure of 3400 kg/cm^2 and sintered at 550°C or a higher temperature in argon for 24 hrs.

Three methods were used to prepare carbon-coated $LiFePO_4$:

Method A — 12 wt% (compared to the $LiFePO_4$ to be coated) of white table sugar was dissolved in a small amount of water. Then $LiFePO_4$ synthesized at 550°C was added to the solution and was ground slowly by hand to make sure that the powder was totally wetted by the sugar solution. The mixture was then heated at 700°C in argon for 4 hrs. Based on the weight loss of sugar heated to 700°C in argon for 4 hrs, 1.00 g of sugar resulted in about 0.23 g of carbon after heating. Therefore, based on the amount of sugar used for the coating, there was about 2.7% carbon by weight in the resulting composite.

Method B — Based on the amount of carbon needed in the final composite, a desired amount of white table sugar was added to the raw materials before mixing. Then the procedure for the synthesis of $LiFePO_4$ was followed. The sintering temperature was

800°C. No additional coating step was used. Under these conditions, 1.00 g of sugar resulted in about 0.18 g of carbon.

Method C — A $LiFePO_4/C$ composite was made by method B with a sintering temperature of 550°C. The composite was then coated with more carbon using the same procedure of method A.

2.2 Coating $LiCoO_2$ with oxides

In this study, two $LiCoO_2$ samples, FMC 010301 and Nippon Chemical Industrial 611061, were coated with different oxides. In addition, five other $LiCoO_2$ samples were also studied. Table 2.1 shows the suppliers of these samples and their Li/Co atomic ratio as determined by Inductively Coupled Plasma/Mass Spectrometry (ICP/MS) at 3M Corp.

Table 2.1 $LiCoO_2$ samples studied

Supplier	Product #	Li-mass %	Co-mass %	Li/Co atomic ratio	Sample used for coating
FMC	00640	7.055	59.05	1.014	No
FMC	00641	6.875	60.05	0.972	No
FMC	00642	6.93	60.7	0.969	No
FMC	00643	7	60.9	0.976	No
FMC	10301	7.095	61.8	0.975	Yes
Nippon Chemical Industrial Co. Ltd.	611061	6.92	59.4	0.989	Yes
Moli Energy	20345	7.19	60.6	1.007	No

To coat $LiCoO_2$ with different oxides, four different coating solutions were used. They were an aqueous solution of $ZrO(NO_3)_2 \cdot xH_2O$ (Alfa Aesar) (17 wt%), zirconium oxide polymeric precursor (Alfa Aesar) diluted with isopropanyl alcohol (40 % v/v), aluminum oxide polymeric precursor (Alfa Aesar), and poly(dimethylsiloxane) $[-SiO(CH_3)_2-]_n$ (Aldrich) diluted with toluene (15 % v/v). Two coating methods were employed.

Method D — First, about 5 g of $LiCoO_2$ was mixed with a desired amount (usually about 5 wt%) of a coating solution by magnetic stirring in an open flask until the mixture was dry. The mixture was then heated at 100°C for 12 hrs to evaporate the solvent in the coating solution. Finally, the heated mixture was heated to 600°C in air for 3 hrs.

Method E — First, 2 g $LiCoO_2$ was mixed with 20 ml coating solution by magnetic stirring for 3 hrs. During the mixing, 0.05 g 3-glycidoxypropyltrimethoxysilane was added as a surfactant. After mixing, the $LiCoO_2$ powder was separated from the coating solution by centrifugation and was then heated at 100°C for 12 hrs to evaporate the solvent in the coating solution. Finally, the mixture was heated to 550°C in air for 3 hrs. The coated sample usually consists less than 2 wt % coating oxide.

2.3 Changing the surface chemistry of $LiCoO_2$ by grinding, heating, or exposure to water

To create fresh surfaces, $LiCoO_2$ was ground in an auto-grinder (Retsch RM-0) for 15 minutes. To clean the surface of $LiCoO_2$, samples were heated in air in a box furnace at 800°C for 12 hrs or at 550°C for 3 hrs. About 5 g $LiCoO_2$ powder was heated

in an alumina boat and cooled to room temperature by removing the boat from the furnace. Gao *et al.* (2002) showed that the cooling rate affects the capacity retention of $LiCoO_2$ after synthesis or after re-heating to 950°C. To investigate this effect of cooling rate on heated $LiCoO_2$, two samples were prepared by heating $LiCoO_2$ to 950°C for 3 hours and were then cooled at different rates. One was slow cooled to room temperature by turning off the furnace. The other sample was removed from the furnace and quickly cooled in air.

To change the surface condition of a heated $LiCoO_2$ sample, about 3 g of heated $LiCoO_2$ was stored in an open flask with about 2 g of water for 7 days. The powder was then heated at 150°C for 12 hours to remove residual water. After all sample preparation, electrodes and cells were always made within a 10 day period.

2.4 Adding fumed oxides to the electrolyte

To investigate the effect of oxide addition to the electrolyte on the capacity retention of $LiCoO_2$, a little (less than 5% by weight) fumed silicon oxide (Alfa Aesar, 99.8%) or fumed aluminum oxide (Alfa Aesar, 99.8%) was added to 1 M $LiPF_6$ in EC/DEC (1:2, v/v). The mixture of fumed oxide and the electrolyte was immediately used to make cells after mixing.

2.5 Electrode and cell making

After synthesis, coating or surface modification by grinding, heating or exposure to water, the rate capability or capacity retention of positive electrode materials was tested in 2325 (23 mm diameter, 2.5 mm thickness) coin cells. Figure 2.1 shows an

exploded view of a lithium coin cell used for electrochemical characterization of the positive electrode materials. The cell stack consists of a working electrode (positive electrode in this study), a microporous polypropylene separator (Celgard 2502), a counter electrode (lithium metal) and an appropriate amount of electrolyte. The separator keeps the positive and negative electrodes from electrically shorting, while allowing lithium ion conduction through the electrolyte contained in its pores. The electrolyte used is 1M $LiPF_6$ in a 33:67 solution by volume of ethylene carbonate (EC)/ diethylcarbonate (DEC) unless specified otherwise. The cell stack is held in place with a spacer and a spring. After the whole cell is assembled, it is crimp-sealed. All cells were assembled in an argon-filled glove box.

On a few occasions, 0.7 M lithium bis(oxalato)borate ($LiB(C_2O_4)_2$, also called LiBOB, Chemetall) in EC:DEC (33:67, v/v) electrolyte was used instead of $LiPF_6$ based electrolyte. As mentioned above, most cells were made with lithium metal as the negative electrode. However, a few Li-ion cells were also made with mesocarbon microbeads (MCMB) as the negative electrode.

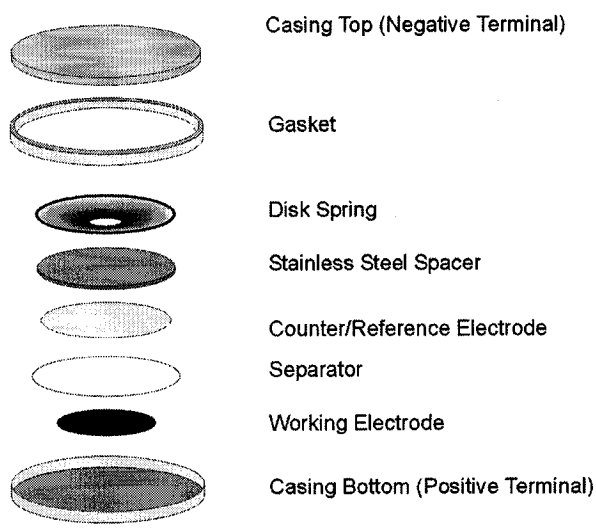

Figure 2.1 An exploded view of a coin type test cell.

To make positive electrodes for coin cells, 85 wt% active electrode material, 7 wt% Super S carbon black (Chemetal Inc.), which provides the electrode with electrical conduction, and 8 wt% polyvinylidene fluoride (PVDF), which acts as a binder, were mixed together in N-methylpyrrolidinone (NMP). The mixed slurry was spread uniformly on a thin aluminum foil using a notch bar spreader. After heating overnight at 110°C in air, the electrode was punched into discs with a diameter of 1.3 cm. A typical electrode disc contains about 10 milligrams active material. Negative electrodes were made in the same way, except that they were spread on a copper foil.

2.6 Cell testing

Cells were charged and discharged between a lower cutoff cell potential and an upper cutoff cell potential with a computer controlled constant-current charger system. Tests were made at a constant temperature of 30.0 + 0.1°C unless specified otherwise. For each positive electrode material, two cells were made and cycled with the same specific current (current per unit mass) to ensure good reproducibility. In this thesis, both mAh/g and C rate are used as the unit of specific current. Using a C/*n* rate, the cell can be fully charged or discharged in *n* hrs. For example, the capacity of $LiFePO_4$ is 160 mAh/g. A C/3 rate corresponds to a specific current of 160/3 mA/g.

During a charge, the potential of the cell rises as energy is added to the cell. The current is stopped when the cell potential reaches the upper cutoff potential. During a discharge, the potential of the cell drops as energy is removed from the cell. The discharge current is stopped when the cell potential reaches the lower cutoff potential. The raw cycling data from the charger system shows the cell voltage versus time.

Specific current multiplied by charging time gives the specific charge capacity (charge capacity of the electrode material per unit mass). By the same calculation, one can obtain the specific discharge capacity. From the cell voltage versus time, one can calculate the voltage versus capacity stored in the cell. This is called a voltage curve. Figure 2.2 shows the voltage curve for a single charge/discharge cycle of a $LiCoO_2$ electrode.

From the potential versus capacity data, differential capacity versus potential data can be generated. An in-house program, Datamangler, by D. A. Stevens was used to calculate differential capacity versus cell potential and capacity versus cycle number based on raw data from the charger systems. Figure 2.3 shows the differential capacity versus cell potential curve for a single cycle of a $LiCoO_2$ electrode. In addition to the voltage curve and the differential capacity versus cell potential curve, the capacity versus cycle number curve will be used to show the capacity retention of electrode materials in the following chapters.

As mentioned in 1.4, the rate capability of $LiFePO_4$ and the capacity retention of $LiCoO_2$ were of most interest in this study. To measure the rate capability of a $LiFePO_4$ electrode sample, a cell containing the electrode was first charged to 4.0 V at 53 mA/g and then trickle charged to 4.0 V using a current of 0.8 mA/g. The cell was then discharged to 2.5 V at specified rates ranging from 0.1C to 5C. Specific currents and specific capacities were calculated based on the mass of $LiFePO_4$, not $LiFePO_4$ and carbon used for coating, in the electrode. To increase the specific capacity of $LiCoO_2$, it was typically charged to 4.5 V and discharged to a lower cutoff potential of 3.6 V. To test

the capacity retention of $LiCoO_2$, it was cycled using a current of 46.7 mA/g. Normally, each full charge-discharge cycle took about 8 hrs.

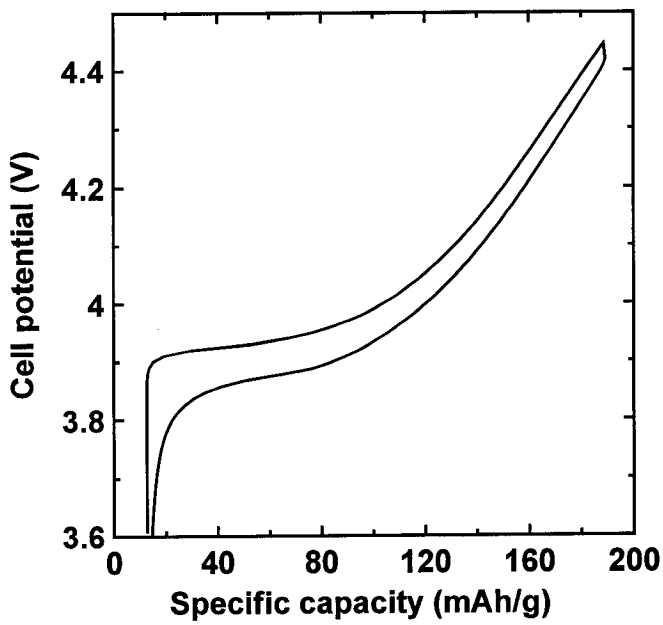

Figure 2.2 Voltage curve for a cycle of a $LiCoO_2$ electrode.

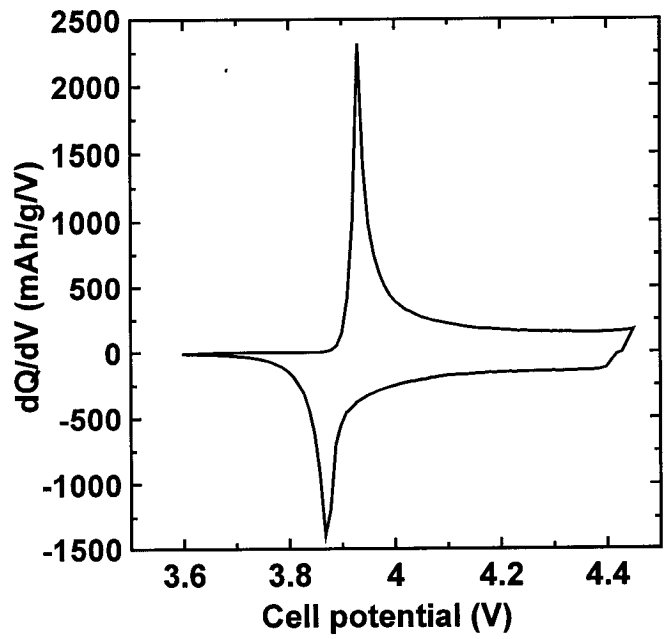

Figure 2.3 Differential capacity vs. cell potential for a cycle of a $LiCoO_2$ electrode.

2.7 X-ray diffraction (XRD)

Powder XRD was used to determine the structure of the electrode materials, the oxides used for coating, and the coated electrode materials. Both Cullity (1967) and Warren (1969) describe powder XRD in detail.

The diffractometers used were Siemens D5000 or D500 diffractometers. Both have a copper target X-ray tube and a diffracted beam monochromater. A flat stainless steel holder with a rectangular well in the center was used to hold the powder samples. X-ray scattering angle ranges were between 10° and 90° with a step size of 0.05°. The count time was 5 seconds/step for a sample containing a single phase. For $LiCoO_2$ coated with oxide, a very long count time (180 seconds/step) was used to obtain XRD patterns showing weak peaks from the coated oxide as well as peaks from $LiCoO_2$. When the amount of available powder was too small to fill the well in the stainless steel holder, a zero background holder was used. This is a single crystal silicon wafer cut along the 510 plane. The silicon 510 plane has a structure factor of zero, so it does not produce Bragg scattering.

To investigate the structural changes in an electrode material, XRD was performed on a working electrode during charge or discharge (Dahn *et al.*, 1981 and Richard *et al.*, 1997). This is called *in-situ* X-ray diffraction. To determine the structure of a charged electrode, the charged electrode was taken out of the cell for X-ray diffraction. This is called *ex-situ* X-ray diffraction. Both *in-situ* and *ex-situ* XRD use the same principles as powder XRD, except that the sample used is an electrode instead of a powder. The preparation of *in-situ* and *ex-situ* samples is described below.

In-situ XRD — The cell for the *in-situ* XRD measurement is similar to the standard coin cell except that the bottom of the cell was replaced with an identical can but with a circular hole (17.5 mm in diameter) machined into it. A circular beryllium disc (22.6 mm in diameter) was then sealed on the inside of this can with a pressure sensitive adhesive (Roscobond). Beryllium has a low specific absorption to X-rays so that it allows the x-ray beam to penetrate to the positive electrode in an *in-situ* XRD cell.

An electrode that is coated on aluminum foil cannot be used in an *in-situ* XRD experiment because the aluminum foil, which would be placed between the electrode materials and the beryllium, will absorb a considerable amount of X-rays. To solve this problem, a Bellcore "plastic" electrode was used (Godz *et al.*, 1994).

To make a Bellcore plastic electrode, a slurry was prepared by mixing 500 mg of electrode material, 50 mg of Super S carbon black, 125 mg of polyvinylidene difluoride(PVDF)/hexafluoropropylene(HFP) (88/12 by weight) binder (Kynar Flex 2801), 200 mg of dibutylpthalate (DBP) plasticizing agent, and 1500 mg of acetone as the solvent. Then the mixed slurry was spread uniformly onto a glass plate using a notch bar spreader. After the acetone evaporated, the positive electrodes were punched into 1.3 cm diameter discs and washed three times with anhydrous diethyl ether to extract the DBP plasticizer. After heating at 110 °C for 12 hrs, the electrode is ready to use for cell assembly.

To make an *in-situ* XRD cell, a Bellcore plastic electrode was centered on the beryllium disc. The rest of the cell is constructed as described previously. After the cell was made, it was placed in a specially designed holder which is then mounted in the diffractometer. The depth of the well of the holder was machined such that the positive

electrode inside the cell would align with the goniometer axis. Figure 2.4 shows an *in-situ* XRD cell and an *in-situ* cell in the holder. Figure 2.5 shows a *in-situ* XRD cell in the holder inside the Siemens D5000 diffractometer with wires connecting the cell to a charger system.

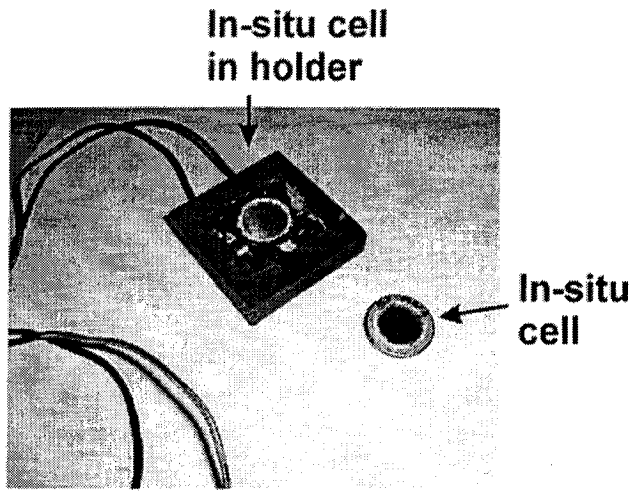

Figure 2.4 Picture of an in-situ XRD cell and a cell mounted in the holder.

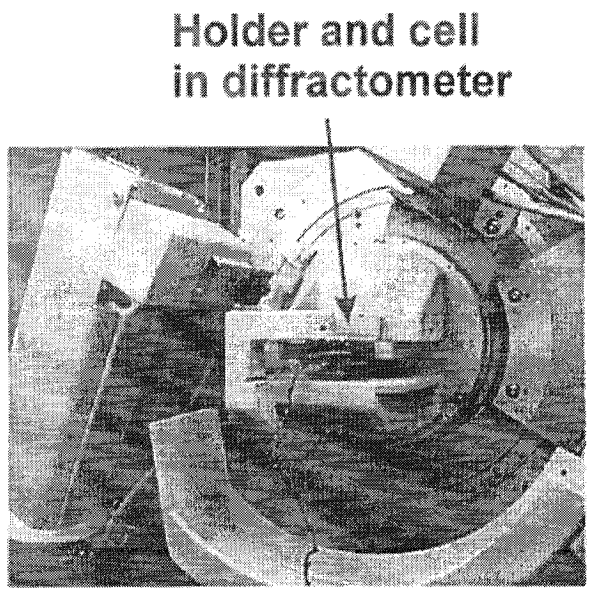

Figure 2.5 Picture of the in-situ cell and holder mounted in the Siemens D5000 diffractometer.

To perform an *in-situ* XRD experiment, the charge of the cell and the first XRD scan were started at the same time. The speed of the XRD scans and the rate of charging or discharging was determined so that, during a charge or discharge, enough scans were taken to show the details of the structural changes of the electrode material. Typically, each XRD scan took about 2 hrs and a charge or discharge took about 30 hrs or longer.

Ex-situ XRD — In an XRD pattern obtained by *in-situ* XRD, there are peaks from the Be window. This makes it difficult to obtain quantitative information about the crystal structure of the electrode material by Rietveld refinement (Rietveld, 1967). To determine the structure of an electrode material at a certain state of charge, the *ex-situ* XRD technique was used. A cell made with a Bellcore electrode as the positive electrode and Li metal as the negative electrode was charged to the desired potential. The current was then stopped for 30 minutes. After this pause, a current of 75% of the previous current was used to charge the cell to the same potential and then the current was stopped for another 30 minutes. This cycling regime was repeated twelve times. After this charging, the cell was opened in a helium-filled glove box. The positive electrode was removed from the cell and sealed in a helium-filled sample holder equipped with an aluminized mylar window (Obrovac, 2001). The carbon black and polymeric binder in the electrode contribute weakly to the diffraction signal. The XRD pattern obtained from the *ex-situ* XRD experiment is dominated by the charged electrode material.

2.8 Morphology and composition study using electron microscopy

Electron Microscopes are used to investigate the morphology and composition of solids on a very fine scale (Goldstein *et al.*, 1992; Reimer, 1984). Two scanning electron

microscopes, a JSM-35CF from JEOL Ltd. and a S-4700 from Hitachi, and a transmission electron microscope (FEI Tecnai-12) were used to study the morphology of the positive electrode materials. Transmission Electron Microscopy (TEM) images of coated and un-coated materials were taken with the FEI Tecnai-12 microscope working at 80 KeV. The Energy Dispersive Spectrometer (EDS) attached to the JEOL scanning electron microscope was also used to study the elemental distribution on the surface of coated $LiCoO_2$ particles.

2.9 Measurement of Electrode Density

Both volumetric energy density and specific energy are important for an electrode material. The volumetric energy density is determined by multiplying the specific energy by the density of the material. Therefore, a high-density material is desirable. The so-called pellet density of the oxides was measured since it is closely related to the achievable electrode density. Pellet density was obtained by making 8 mm diameter pellets with approximately 500 mg of powder under a pressure of 3400 kg/cm^2. The thickness and diameter of the pellet after pressing was measured and the density was then calculated. The error is estimated to be ± 0.08 g/cm^3.

2.10 Thermogravimetric Analysis (TGA)

Thermogravimetric Analysis measures the change in weight of a sample as a function of increasing temperature. TGA measurements were used to study the decomposition of the coating precursors in air. A TA Instruments TGA 51

Thermogravimetric Analyzer was used for these measurements. The scan rate was 5 °C per minute.

Chapter 3 Carbon coating on $LiFePO_4$

3.1 Importance of reducing the amount of carbon used for coating $LiFePO_4$

According to Huang *et al.* (2001), both small particle size and intimate carbon contact are essential to ensure good rate capability of the $LiFePO_4$/C composite. A large amount of carbon in the $LiFePO_4$/carbon composite decreases the energy density of the material significantly, since carbon is inactive and bulky. Bulk carbon has a density of 2.2 g/cm^3 which is only 61% of the density of $LiFePO_4$ (3.6 g/cm^3). Thus, the added carbon will impact the volumetric energy density of $LiFePO_4$/C composites more severely than the specific energy.

Figure 1 shows the effect of the amount of carbon in the $LiFePO_4$/C composite on the theoretical energy density of the composite, assuming a 3.5 V average potential. As the amount of carbon is increased from 0 to 15 wt%, the volumetric energy density decreases by 22% from 2.1 Wh/cm^3 to 1.6 Wh/cm^3. The specific energy decreases by 15% from 0.57 Wh/g to 0.48 Wh/g over the same range. As shown by Yamada *et al.* (2001), $LiFePO_4$ (without carbon) has a larger specific energy than both $LiCoO_2$ and $LiMn_2O_4$ and a larger volumetric energy density than $LiMn_2O_4$. If these advantages are to be maintained, the amount of carbon in $LiFePO_4$/C composites should be minimized.

Theoretically, to minimize the amount of carbon, the maximum particle size that provides acceptable rate capability for normal use should first be found. Particles may not need to be nano-particles. Once the particle size is known, the corresponding surface area to be covered by carbon can be determined. Second, an effective method of coating carbon on the surfaces of the particles to minimize the total amount of carbon is needed.

Ravet *et al.* (1999, 2001) have shown that only 1 wt% carbon can improve the rate capability significantly at 80°C. The authors do not, however, report the electrochemical performance of their carbon-coated $LiFePO_4$ at room temperature.

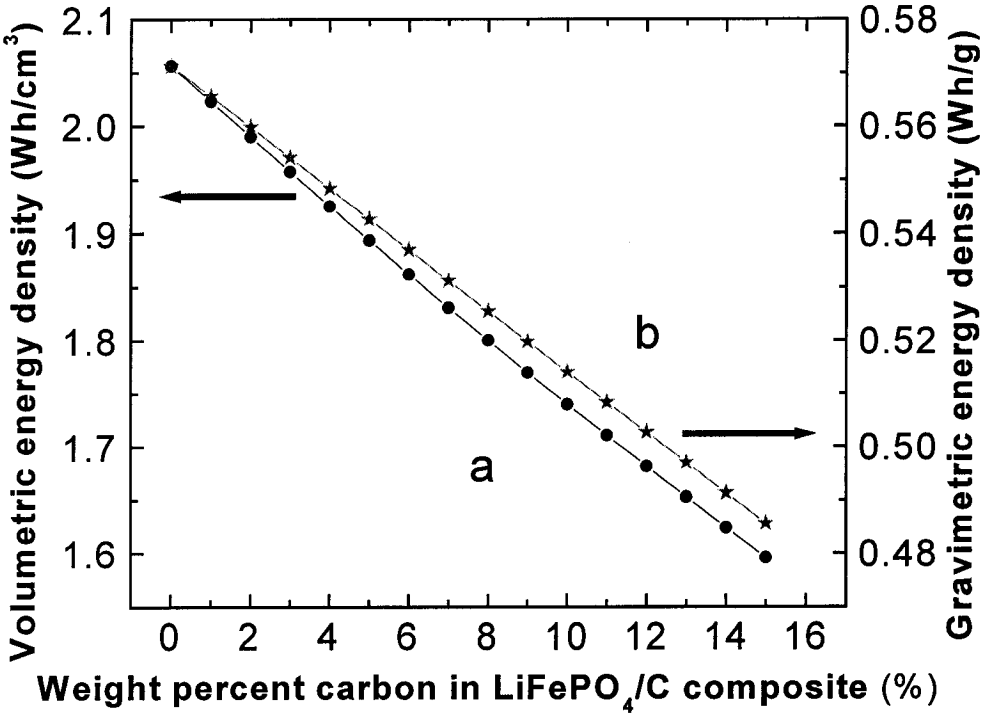

Figure 3.1 Theoretical effect of the amount of carbon in $LiFePO_4$/C composites on (a) volumetric and (b) gravimetric energy density of the composite.

Ravet *et al.* (1999, 2001) reported two ways to coat carbon: mixing $LiFePO_4$ powder with sugar solution and heating the mixture at 700°C, or synthesizing $LiFePO_4$ with some organic material added before heating. For convenience, we call these two methods method A and method B respectively. In this study, method A, method B and their combination, called method C here, were used to improve the rate capability of $LiFePO_4$ at room temperature. Details of these methods have been given in 2.1. In addition, the effect of the amount of carbon used in method B was also studied.

3.2 Effect of carbon coating

Several different sintering temperatures from 400°C to 800°C were used to synthesize $LiFePO_4$. A single phase of $LiFePO_4$ could be synthesized with a sintering temperature of 550°C or higher. As pointed out by Yamada *et al.* (2001), the particle size increases as the sintering temperature increases. The same trend was observed in our experiments. Figures 3.2a and 3.2b show the SEM images of $LiFePO_4$ sintered at 800°C and 550°C, respectively. $LiFePO_4$ sintered at 800°C has a particle size of several μm while $LiFePO_4$ sintered at 550°C has an average particle size below 1 μm.

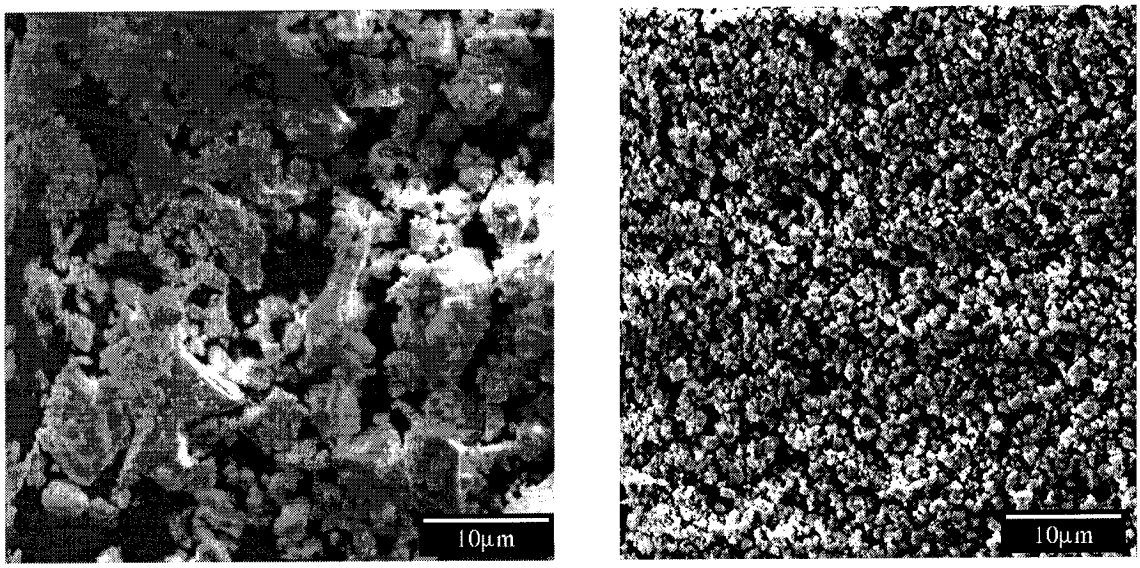

(a) **(b)**

Figure 3.2 SEM images of $LiFePO_4$ sintered at (a) 800℃ and (b) 550℃.

Yamada claimed that $LiFePO_4$ sintered at 550°C has the best rate capability and delivers a capacity of 160 mAh/g at a current density of 0.12 mA/cm^2 (Yamada *et al.*, 2001). Since he did not give the actual mass of $LiFePO_4$ in the electrode, this current density could not be converted to specific current that is predominantly used in this study.

Based on his recommendation, $LiFePO_4$ sintered at 550°C was used to study the effect of carbon coating.

Figure 3.3 shows TEM images of $LiFePO_4$ sintered at 550°C coated with 2.7 wt% carbon. Figure 3.3 (a) shows that the particles are smaller than 1 μm. Each particle is attached to something that has a weaker contrast and is believed to be carbon. With a larger magnification, Figure 3.3(b) shows the intimate contact between a $LiFePO_4$ particle and the carbon attached to it. The color of $LiFePO_4$ turned from white to gray after coating. With such a coating of carbon, the conductivity of a $LiFePO_4$ composite should be improved.

Figure 3.4 shows the voltage curve of $LiFePO_4$ sintered at 550°C with or without a carbon coating. Figure 3.4(a) shows that un-coated $LiFePO_4$ delivers a specific capacity less than 20 mAh/g even with a small specific current (2 mA/g). Its poor rate capability is caused by its poor conductivity. Figure 3.4(b) shows that after coating with 2.7 wt% carbon using method A, $LiFePO_4$ delivers a reversible capacity of about 145 mAh/g with a specific current of 16 mA/g. Apparently, by improving the surface conductivity of $LiFePO_4$, carbon coating improves the rate capability of $LiFePO_4$.

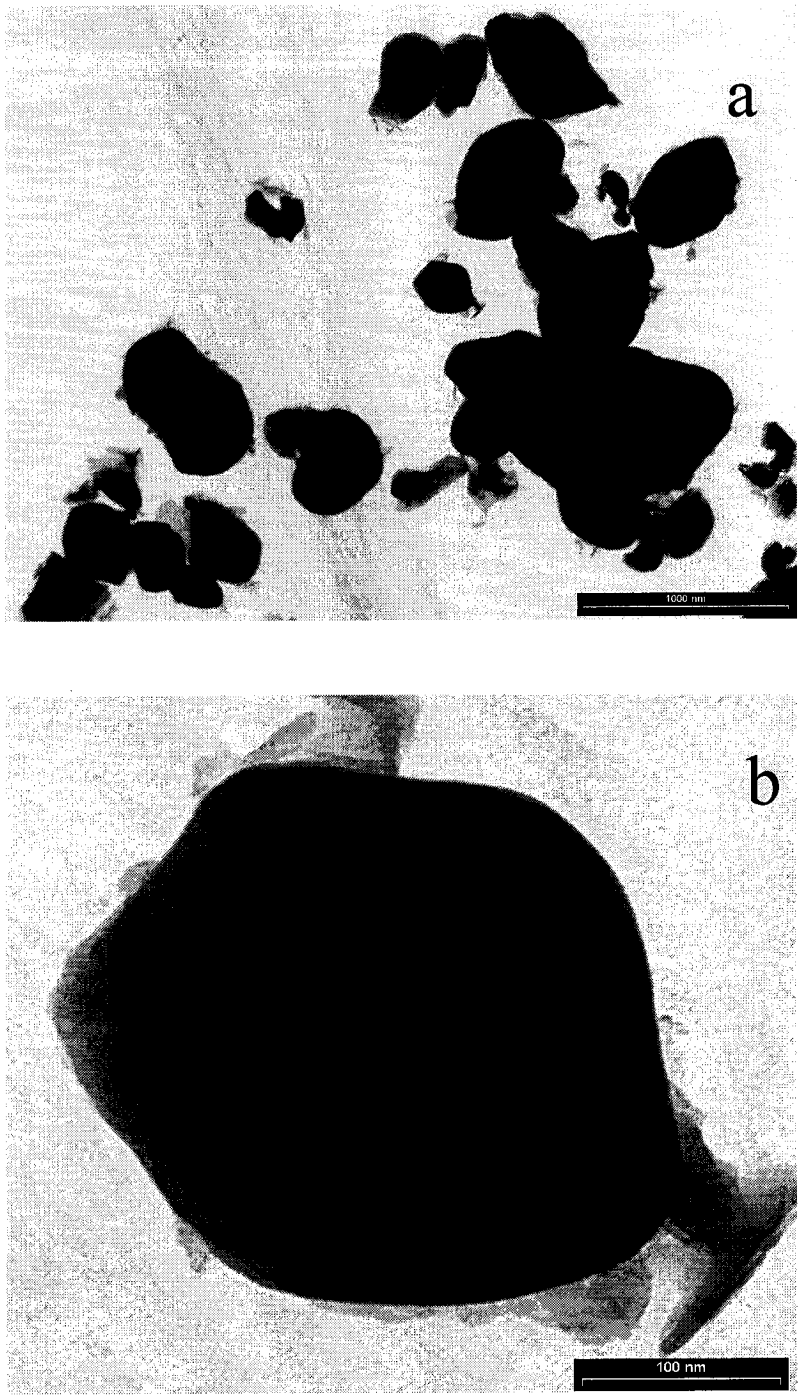

Figure 3.3 TEM images of $LiFePO_4$ sintered at 550℃ coated with 2.7 wt% carbon.

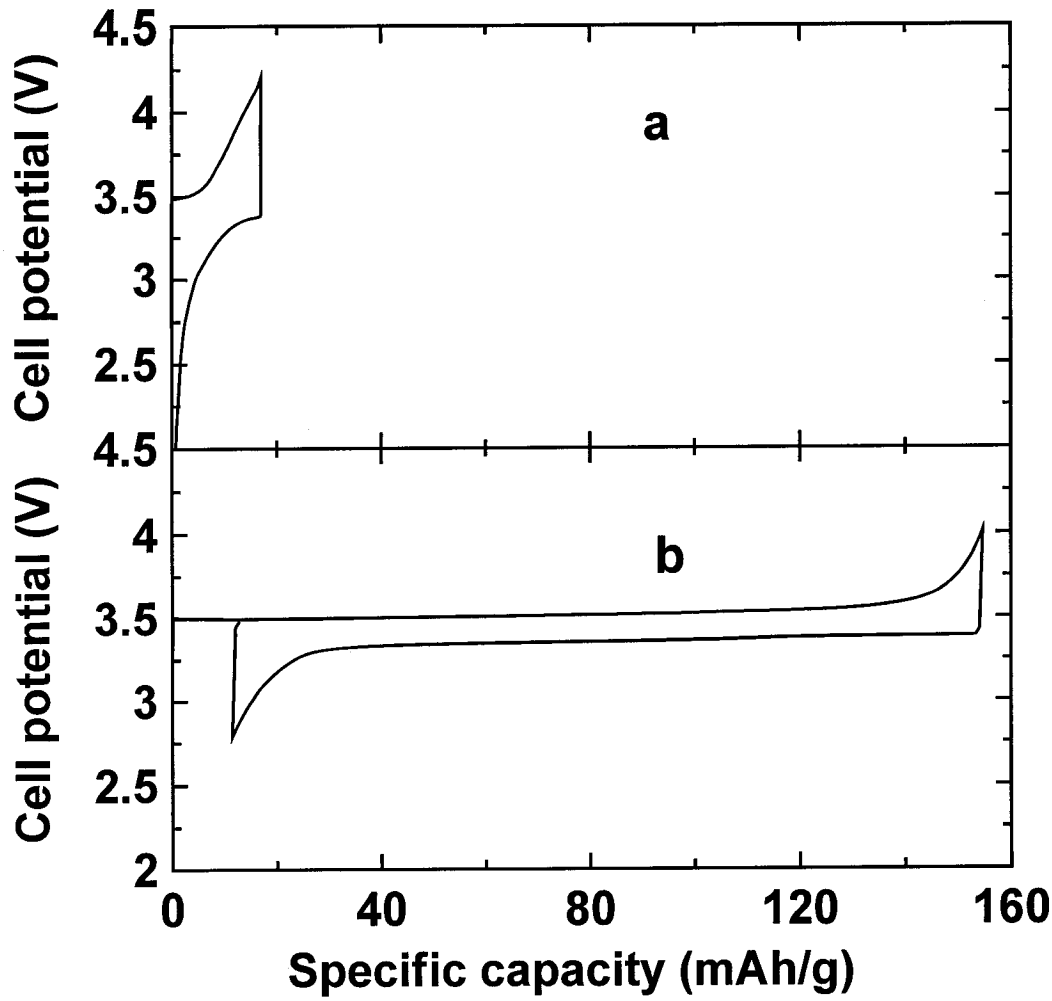

Figure 3.4 Voltage curve of the first cycle of $LiFePO_4$ sintered at 550℃ (a) without and (b) with 2.7 wt% carbon coating.

3.3 Comparison between synthesis methods A, B and C

The rate capability of $LiFePO_4$ samples made by methods A, B and C, were compared. Using method A, a sample was sintered at 550°C and coated with 2.7 wt% carbon. Using method B, 20.0 % by weight of sugar (compared to the weight of the resultant $LiFePO_4$) was added to the raw material before the first heating. Thus, a $LiFePO_4$/C composite with 3.5 wt% carbon was made. Using method C, the final

material had 6.2 wt% carbon in the composite. For convenience, these three samples will be called samples A, B and C respectively.

Figure 3.5 shows the specific capacity versus specific current for Li/$LiFePO_4$ cells made from samples A, B and C. For comparison, the specific capacity versus current of the $LiFePO_4$/C composite reported by Huang *et al.* (2001) is also plotted in the figure. The comparison data was obtained from Figure 3 of a paper by Huang *et al.* (2001) where a 2.8 V cutoff was used. Huang *et al.* (2001) did not specify the current used to charge the cell before discharging.

As shown in Figure 3.5, all three samples have good rate capability. They all have specific capacities larger than 120 mAh/g even at a 2C rate. However, sample C has the best rate capability. It has a specific capacity of 125 mAh/g even at a 5C discharge rate. Discharge curves for sample C are shown in Figure 3.6. Our 32 channel cycling unit is primarily designed for high precision, low rate work and only examines each cycler channel once every 2.5 minutes. This is why there are only a few data points for the 5C discharge. However, this does not affect the specific capacity measurement between 4 V and 2.8 V. Sample B has a better rate capability than sample A. Compared with our materials, Huang *et al.*'s material has a slightly higher specific capacity except at a 5C rate (Huang *et al.*, 2001).

Figure 3.7 shows the fraction of the capacity obtained at a particular discharge rate to that obtained at 0.1 C for the materials described in Figure 3.5. Figure 3.7 shows that samples B and C have better rate capabilities than Huang's material while sample A still shows the poorest rate capability.

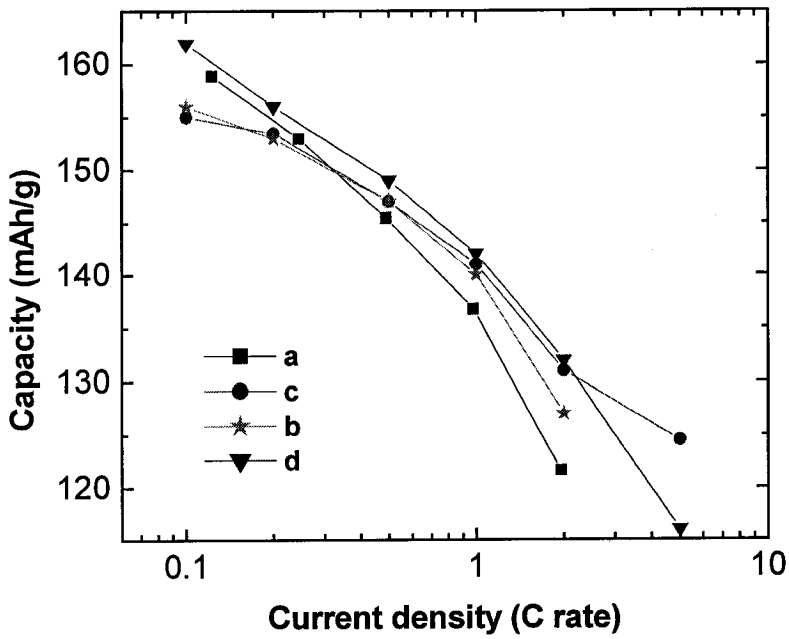

Figure 3.5 Specific capacity of (a) sample A, (b) sample B, (c) sample C, and (d) material reported by Huang et al. (2001) at different specific currents with a lower cutoff voltage of 2.8 V (C-rate was taken to be 160 mA/g) (Chen Z. H. and Dahn J. R., 2002a).

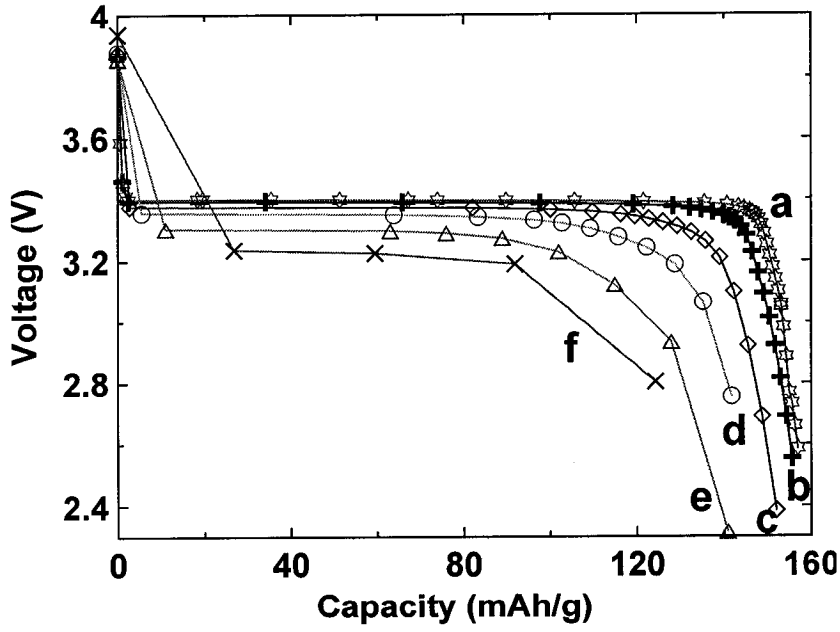

Figure 3.6 Voltage versus capacity of Li/LiFePO$_4$ cells using sample C at various discharge rates: (a) 0.1 C, (b) 0.2 C, (c) 0.5 C, (d) 1 C, (e) 2 C, and (f) 5 C rate (C-rate was taken to be 160 mA/g) (Chen Z. H. and Dahn J. R., 2002a).

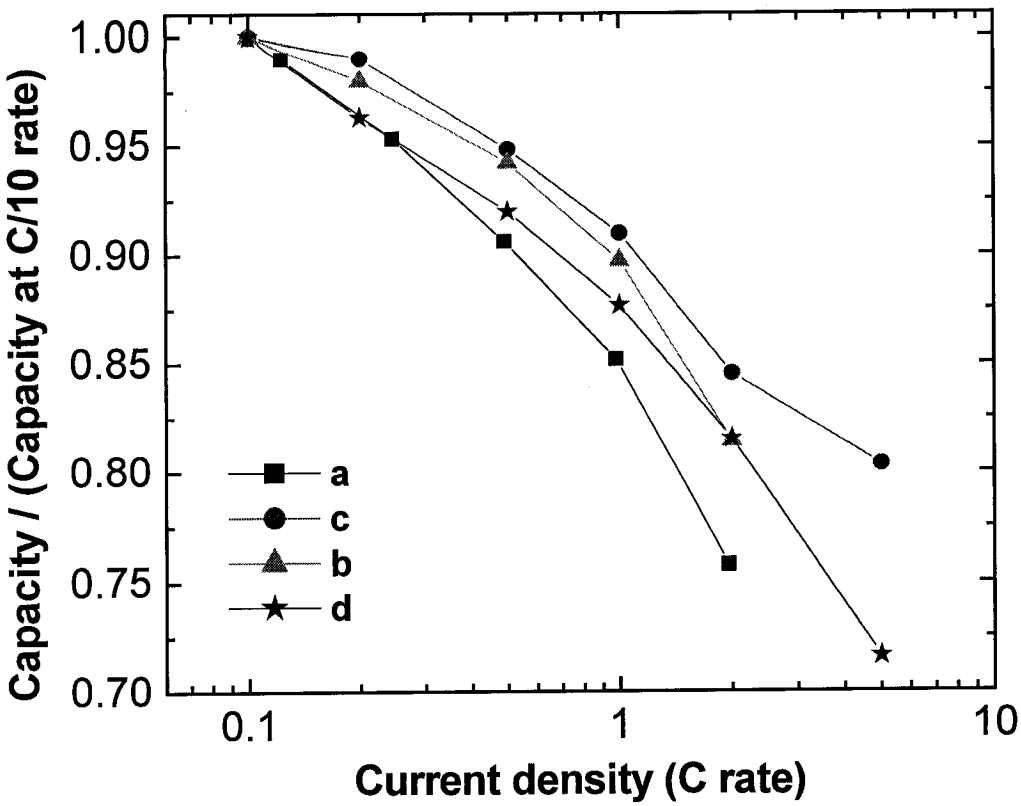

Figure 3.7 Relative specific capacity of (a) sample A, (b) sample B, (c) sample C, and (d) material reported by H. Huang et al. (2001) at different specific currents with a lower cutoff voltage of 2.8 V. For this figure the capacity at 0.1C was set to 1.

Based on Figures 3.5 and 3.7, it is clear that sample B has better rate capability than sample A. Figure 3.8 shows TEM images of $LiFePO_4$ coated with method B. Figure 3.8a shows that sample B has primary particles of about the same size as sample A. These form agglomerates having different sizes. Compared with $LiFePO_4$ coated by method A shown in Figure 3.3, $LiFePO_4$ coated with method B is more uniformly covered with carbon. The particles are also connected to each other by carbon. With these images one can describe the two samples as follows: In sample B, particles have an almost uniform particle size and are well covered by carbon. In sample A small particles form agglomerates in the first heating step, before coating. The surface tension of the sugar

solution makes it difficult for the sugar solution to penetrate into the very fine channels within the agglomerates during the coating process. Then, after coating, the agglomerates may only be coated on the surface of the agglomerate, and not inside.

Figures 3.5 and 3.7 show that sample B has a very good rate capability. Figure 3.8 shows that this material has a uniform small particle size and all the particles are well coated with carbon. This indicates that method B is more effective than method A for improving the rate capability of $LiFePO_4$. Even though method C gives a slightly better rate capability, sample C contains more carbon which reduces volumetric energy density. Furthermore, method C is more complicated than method B. Method B was studied further as detailed below.

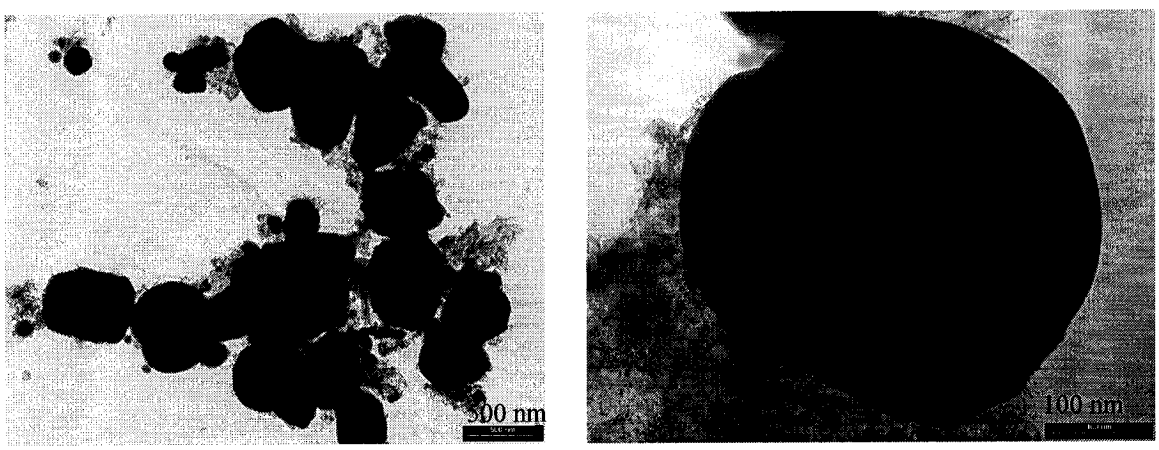

Figure 3.8 TEM images of $LiFePO_4$ coated with method B.

3.4 Effect of the amount of carbon on $LiFePO_4$ made by method B

During the decomposition and sintering in method B, the sugar is converted to carbon that acts as a conductive additive and also controls the particle growth. A carbon gel added during synthesis by Huang *et al.* (2001) served a similar purpose. By changing the amount of sugar, one can control the particle size and conductivity of the material and therefore affect the rate capability of $LiFePO_4$. The effect of the amount of carbon on the properties of materials synthesized by method B was therefore investigated.

Six samples were made by method B with 0, 2.5 wt%, 5 wt%, 15 wt%, 20 wt% and 40 wt% sugar added before heating, respectively. For these samples, the ball milling time during mixing of the reactants was 2 hours. The resultant amount of carbon present in these six samples after heating is about 0, 0.4 wt%, 0.9 wt%, 2.7 wt%, 3.5 wt% and 6.7 wt% respectively. Figure 3.9 shows the specific capacities of the six samples at different discharge rates with a 3.0 V cutoff. As the carbon content of the composite increased, the specific capacity of the $LiFePO_4$ phase was found to increase for all discharge rates assessed.

Figure 3.10 shows the discharge capacities of the six samples measured at a 2C rate at 30°C and at 55°C with a lower cutoff of 3.0 V. Figure 3.9 shows that the capacity at 2C increases dramatically when the amount of carbon increases from 0 to 0.9 wt% for cells operated at both 30°C and 55°C. Above 0.9 wt%, the capacity still increases as the amount of carbon increases, but at a much slower rate.

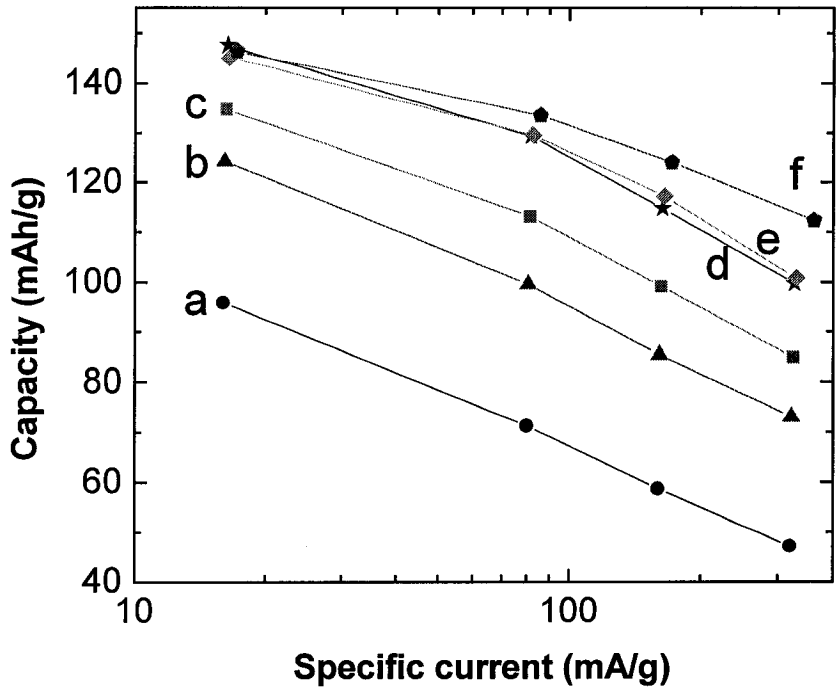

Figure 3.9 Specific capacities of $LiFePO_4$/C composites made by method B with (a) 0, (b) 0.4 wt%, (c) 0.9 wt%, (d) 2.7 wt%, (e) 3.5 wt%, and 6.7 wt% carbon at different discharge rates with a lower voltage cutoff of 3 V.

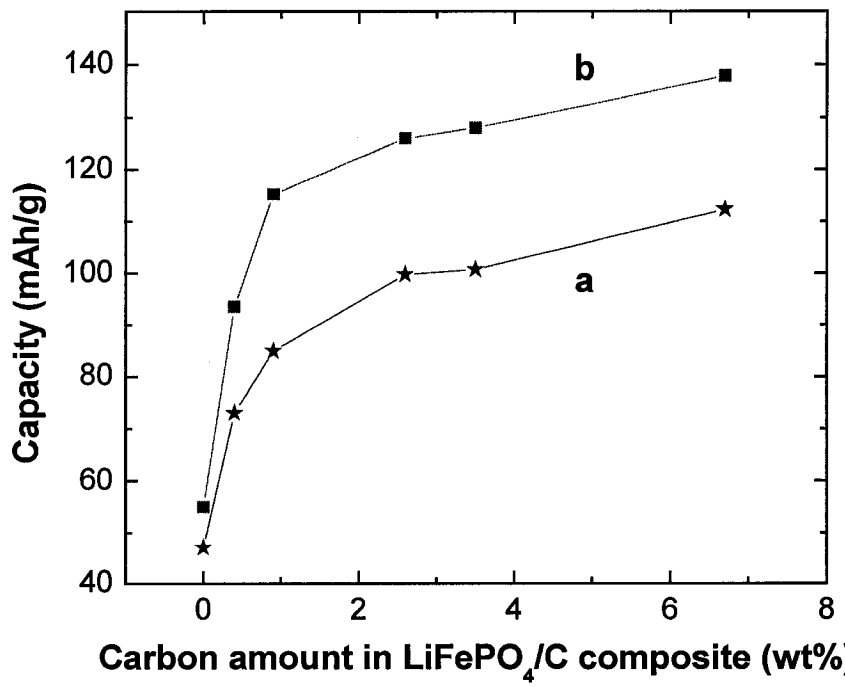

Figure 3.10 Specific capacities versus carbon content of the six $LiFePO_4$/C composites at a 2C discharge rate (a) at 30 ℃ (b) 55 ℃.

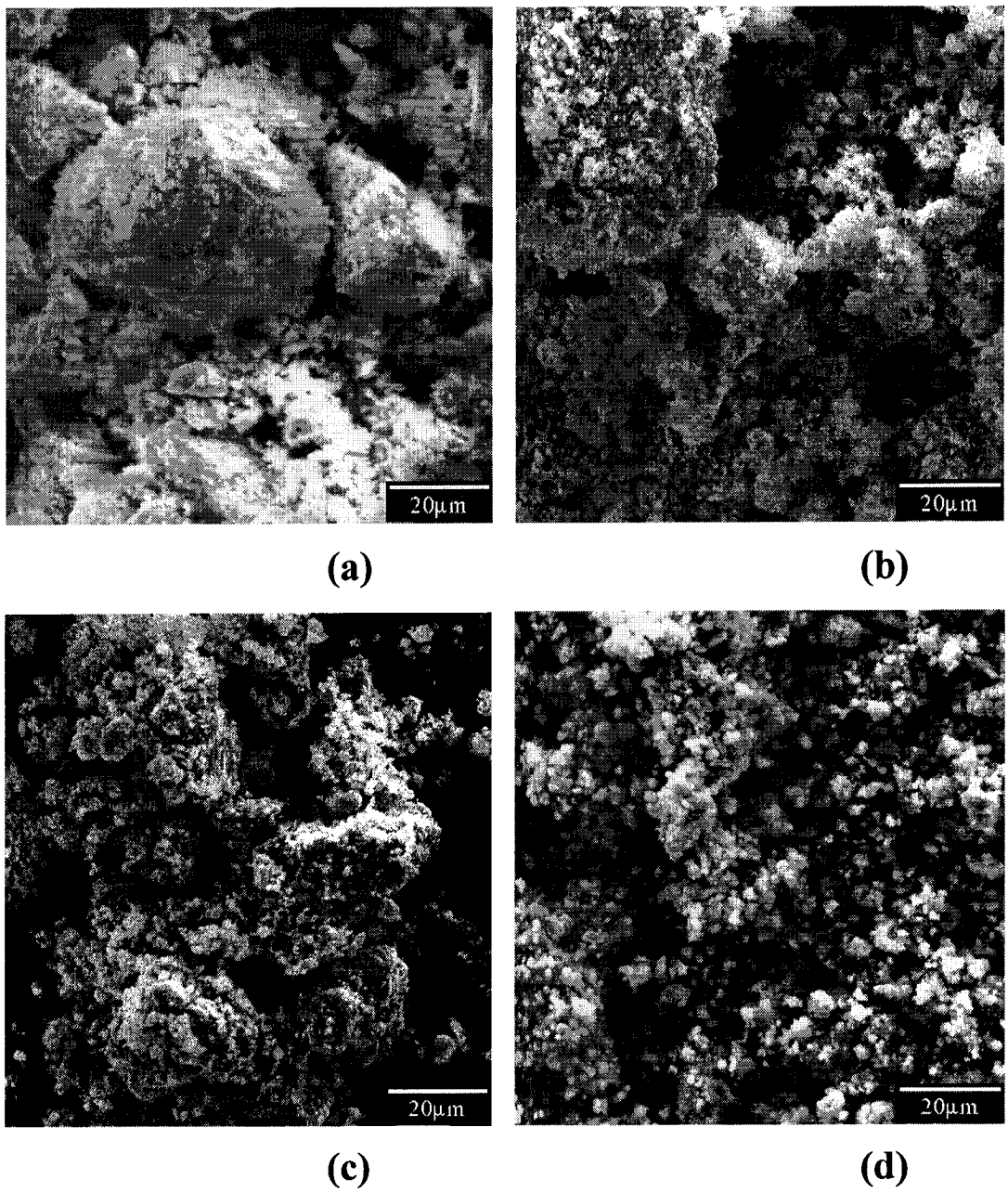

Figure 3.11 SEM images of the $LiFePO_4$/C composites made by method B with (a) 0 wt%, (b) 0.4 wt%, (c) 0.9 wt%, and (d) 2.7 wt% carbon (Chen Z. H. and Dahn J. R., 2002a).

Figure 3.11 shows SEM images of the samples with 0, 0.4 wt%, 0.9 wt% and 2.7 wt% carbon. One can clearly see that the particle size decreases as the amount of carbon

increases. Therefore, there is clear evidence that adding sugar during the first heating dramatically slows the particle growth.

From Figure 3.10, it is clear that even a very small amount of carbon in the $LiFePO_4$/C composite (less than 1 wt%) can improve the rate capability significantly. This indicates that method B is an effective method to improve the rate capability of $LiFePO_4$. According to the results of pellet density measurements, $LiFePO_4$ coated with 3.5 wt% carbon or less has a pellet density of 2.68±0.08 g/cm^3, the same as that of the pure $LiFePO_4$. This indicates that up to 3.5 wt% carbon does not cause a significant decrease of electrode density. For the other two samples with higher carbon content, the measurement of pellet density was not successful by the same method because a pellet could not be made from the powder under such a pressure.

Yamada *et al.* (2001) showed that $LiFePO_4$ reacts very weakly with electrolyte at elevated temperatures compared to other common electrode materials. A similar result was obtained with sample A (MacNeil *et al.*, 2002). Therefore $LiFePO_4$ coated with carbon may be suitable for large cell applications. For these large cells, operating temperatures are commonly near 55°C, at least if cell cooling is accomplished by radiator methods. In such an application, the composite with about 3 wt% carbon may be a good choice because it has a sufficient capacity (about 130 mAh/g) at a 2C rate at 55°C without causing the electrode density to decrease. We believe that the rate capability of $LiFePO_4$ can be improved even further by using a liquid-based method to mix organic additives with the raw materials prior to the heating step, rather than solid sugar as in method B.

3.5 Capacity retention of $LiFePO_4$ coated with carbon

Good capacity retention is also essential to an electrode material for commercial applications. According to Huang *et al.* (2001), the capacity of their $LiFePO_4$/C composite with 15 wt% C faded by only 8 % after 800 cycles at a 5C rate. Figure 12 shows excellent capacity retention of sample C. The electrode was charged at a C/3 rate to 4V and discharged at a 1C rate to 3V. After 1000 cycles, it still delivered more that 80 % of its initial capacity. Thus $LiFePO_4$ coated with 6.2 wt% C has excellent cycling behavior as well as good rate capability, which is also indicated by the initial capacity of more than 140 mAh/g at such a rapid cycling rate. This excellent cycling behavior and rate capability, together with its excellent safety properties make $LiFePO_4$ coated with carbon a very attractive cathode material.

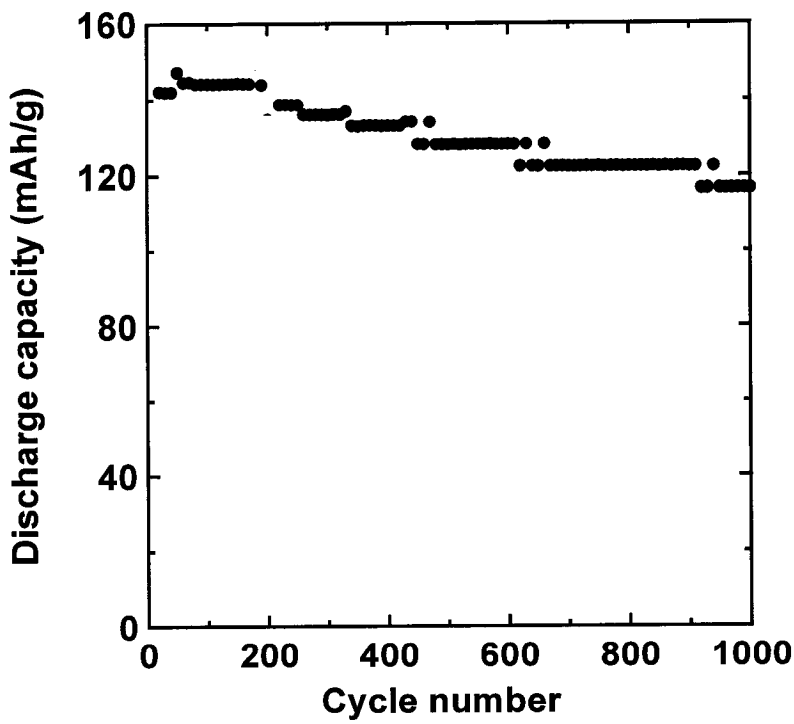

Figure 3.12 Discharge capacity versus cycle number for sample C with a 1C discharge rate.

3.6 Summary

A $LiFePO_4$/C composite (3.5 wt% carbon), synthesized by adding sugar during the initial heating of the reactants, had comparable rate capability to material with 15 wt% carbon reported by H. Huang *et al.* (2001) recently. When sugar is added before heating, the particles are of uniform size and are well coated by carbon. These characteristics apparently promote good rate capability. The presence of 3.5 wt% carbon or less does not cause a decrease in pellet density. With the excellent rate capability and capacity retention shown above, in addition to its excellent safety properties, $LiFePO_4$ coated with carbon will definitely be a good choice as a positive electrode material for certain applications, such as large Li-ion cells for hybrid electric vehicles or electric vehicles.

Chapter 4 $LiCoO_2$ coated with oxides

4.1 Introduction

Cho *et al.* (1999, 2000a, 2000b, 2001a, and 2001b) reported that $LiCoO_2$ coated with a metal oxide surface layer delivers 20% more capacity if charged to 4.4 V instead of 4.2 V. The coated $LiCoO_2$ was shown to give excellent capacity retention even when cycled to 4.4 V. Similar improvements obtained by coating $LiCoO_2$ with metal oxides were reported by other researchers soon afterwards (Wang *et al.*, 2002a and 2002b; Liu *et al.*, 2002; Kannan *et al.*, 2002). The improvement in the capacity retention of coated $LiCoO_2$ cycled to high potentials is significant as reported. However, the improved cycling behavior may still not be able to meet the cycle life requirements (more than 500 cycles) for some commercial applications.

The capacity retention of an electrode material depends strongly on the lower cutoff potential and the discharge rate used for cycling. If the capacity loss is primarily caused by an increase in ohmic impedance of the cell, then low cutoff potentials, like 2.5 V, which are far below the average potential of the majority of the discharge, will give improved capacity retention compared to high lower cutoff potentials (like 3.6 V). In the literature, relatively low lower-cutoff potentials have been used to evaluate the capacity retention of coated $LiCoO_2$. In Cho *et al.*'s papers (1999, 2000a, 2000b, 2001a, and 2001b), a lower cutoff potential of 2.75 V was used. Similarly, in Wang's papers (Wang *et al.*, 2002a and 2002b), 2.5 V was used as the lower cutoff. With the increased lower-cutoff potential (like 3.3 V versus Li) that is required by battery packs in portable electronics, the cycling behavior of the coated materials may be worse than that reported

(Cho *et al.*, 1999, 2000a, 2000b, 2001a, and 2001b; Wang *et al.*, 2002a and 2002b; Liu *et al.*, 2002). Here, a lower cutoff potential of 3.6 V was selected so that impedance growth, and its impact on capacity retention, could be detected with great sensitivity.

Cho *et al.* (2001b) believe that the coating layer serves as a mechanical constraint to prevent the Li_xCoO_2 lattice from expanding and contracting during charge/discharge cycling. Other researchers also believe that oxide coating improves the capacity retention of $LiCoO_2$ by improving its structural stability even though other factors, such as physically separating the $LiCoO_2$ surface from the electrolyte, contribute as well (Wang *et al.*, 2002a and 2002b; Liu *et al.*, 2002; Kannan *et al.*, 2002).

Two commercial samples of $LiCoO_2$ were coated with ZrO_2, Al_2O_3, and SiO_2 so that the differences in performance between the different metal oxide coatings could be established. Table 4.1 shows the starting material, coating precursor and coating method used for each sample. The coated $LiCoO_2$ samples and the control sample were cycled between 3.6 V and 4.5 V versus Li metal using a specific current of 47 mA/g.

Table 4.1 Coated samples studied in this chapter

Starting material	Coating method	$ZrO(NO_3)_2 \bullet xH_2O$	ZrO_2 polymeric precursor	Al_2O_3 polymeric precursor	Poly(dimethylsil-oxane) $[-Si(CH_3)_2O-]_n$
$LiCoO_2$ 010301	Method D	Sample D	Sample E		
$LiCoO_2$ 611061	Method D		Sample F	Sample G	Sample H
$LiCoO_2$ 010301	Method E		Sample I	Sample J	Sample K

4.2 FMC $LiCoO_2$ 010301 coated with ZrO_2

4.2.1 Morphology of FMC $LiCoO_2$ 010301

According to Cho *et al.* (2001b), $LiCoO_2$ coated with ZrO_2 has excellent capacity retention when cycled to 4.4 V. To verify their results, FMC $LiCoO_2$ 010301 was coated with ZrO_2. The morphology of un-coated FMC $LiCoO_2$ 010301 was studied by electron microscopy. Figure 4.1a shows that this $LiCoO_2$ sample has a primary particle size of about 1μm. The primary particles are seen to form clusters. The TEM image in Figure 4.1b shows that the surface of this un-coated $LiCoO_2$ is smooth.

4.2.2 Precursor for ZrO_2 coating

Since the coating precursors used by Cho *et al.* (2001b) were synthesized by Samsung Inc. and are not commercially available, two other coating precursors, zirconium oxide polymeric precursor and an aqueous solution of $ZrO(NO_3)_2 \cdot xH_2O$, were used.

To determine the temperature at which the precursors will be completely decomposed, the precursors were studied by TGA. Figure 4.2 shows the weight loss of the precursors versus temperature for heating at a rate of 5 °C per minute in air. It is clear that they both completely decompose above 500 °C. After decomposition, $ZrO(NO_3)_2 \cdot xH_2O$ gives 42 wt% ZrO_2 and zirconium oxide polymeric precursor gives 31 wt% ZrO_2.

Figure 4.3 shows the XRD patterns of the solid that remains after decomposition of the precursors. According to Figure 4.3a, the remains from the decomposition of $ZrO(NO_3)_2 \cdot xH_2O$ consist of two phases: monoclinic ZrO_2 and tetragonal ZrO_2. Figure

4.3b shows that Zirconium oxide polymeric precursor decomposes to a single tetragonal phase of ZrO_2.

4.2.3 Physical Characterization of $LiCoO_2$ 010301 coated with ZrO_2

By method D, which was described in 2.2, two samples were prepared by coating FMC $LiCoO_2$ 010301 with the two precursors respectively. For convenience, the sample coated with $ZrO(NO_3)_2 \cdot xH_2O$ is called sample D. The sample coated with zirconium oxide polymeric precursor is called sample E. Both samples were studied by XRD, TEM, SEM and EDS to confirm that the metal oxide was successfully coated on the surface of the $LiCoO_2$ powder.

4.2.3.1 Characterization of $LiCoO_2$ 010301 coated with ZrO_2 by XRD

To identify the phases present in the samples, slow scan x-ray diffraction, taking 40 hours for each sample, was performed. Figure 4.4 shows the x-ray diffraction patterns of both samples D and E. In order to make the peaks from ZrO_2 more visible, the intensity in Figures 4a and 4b was plotted on a logarithmic scale. For comparison, Figure 4.4c shows a diffraction pattern of nanocrystalline tetragonal ZrO_2 that was obtained by heating the zirconium oxide polymeric precursor at 550°C for 3 hours. In Figures 4.4a and 4.4b, besides dominant peaks from $LiCoO_2$, there are four weak, broad peaks from tetragonal ZrO_2. This demonstrates that the coating material exists in the form of nanocrystalline tetragonal ZrO_2 in both samples D and E. The mass percentage of ZrO_2 is about 4% and 7% in samples D and E, respectively.

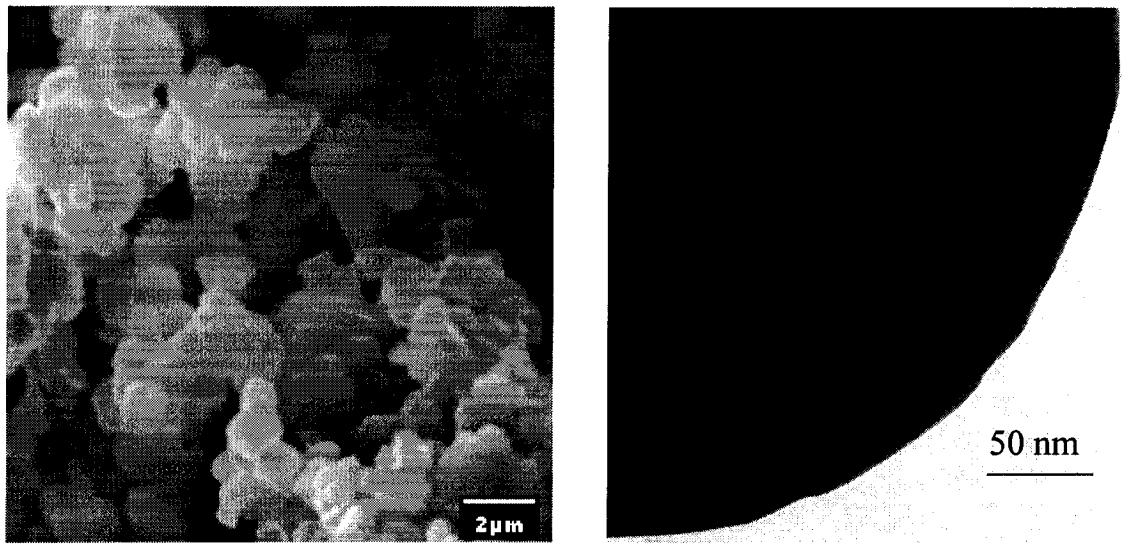

(a) (b)

Figure 4.1 (a) A SEM image (b) a TEM image of FMC $LiCoO_2$ 010301

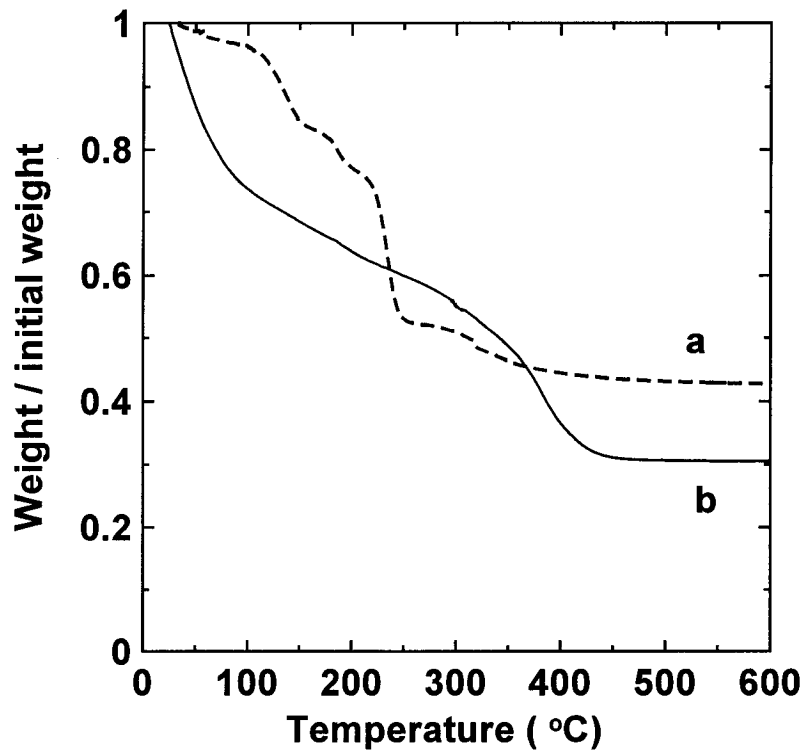

Figure 4.2 Relative weight versus temperature of (a) $ZrO(NO_3)_2 \bullet xH_2O$ and (b) zirconium oxide polymeric precursor heated in air at a rate of 5 °C per minute.

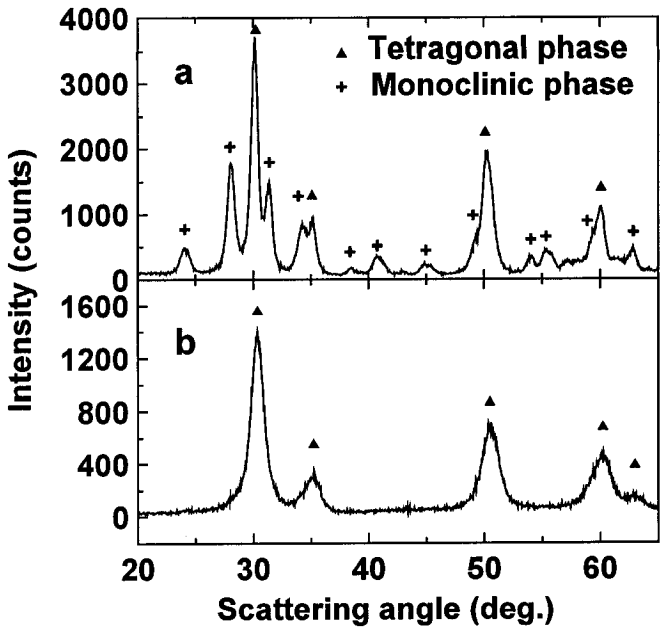

Figure 4.3 XRD pattern of the solid remaining after the decomposition of (a) $ZrO(NO_3)_2 \bullet xH_2O$ and (b) zirconium oxide polymeric precursor.

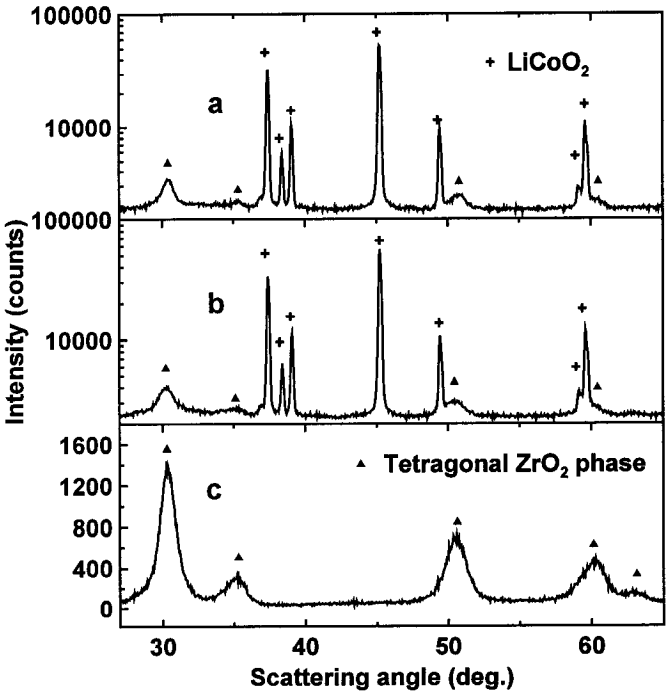

Figure 4.4 XRD pattern of (a) sample D, (b) sample E and (c) nanocrystalline ZrO_2 from the decomposition of zirconium oxide polymeric precursor (Chen Z. H. and Dahn J. R., 2002b).

These results disagree with Cho's observation (2001b). Cho *et al.* could not find evidence for the existence of ZrO_2 in XRD patterns of their coated $LiCoO_2$. Two hour diffraction patterns taken on our samples, which have been shown to contain nanocrystalline ZrO_2, did not show clear evidence for the weak ZrO_2 peaks due to poor signal to noise ratios. Thus it is quite likely that had Cho *et al.* done careful slow scan diffraction on their samples, that they would have observed nanocrystalline ZrO_2. Instead, they assumed that the coated material reacted with $LiCoO_2$ and formed a layer of $LiZr_xCo_{1-x}O_2$ on the surface of the particle (2001b). However, such a $LiZr_xCo_{1-x}O_2$ phase may not exist since it has never been reported.

4.2.3.2 Characterization of $LiCoO_2$ 010301 coated with ZrO_2 by SEM and EDS

A SEM study shows that samples D and E have about the same primary particle size as $LiCoO_2$ 010301. This indicated that the particles of $LiCoO_2$ did not grow during the heating process of the coating. The purpose of coating is to change the surface of $LiCoO_2$ while keeping its original bulk properties. Hopefully, the surface of each particle in both samples D and E has been modified by coating.

With the Hitachi SEM S-4700, the coated layers on both samples D and E were easily observed. Figure 4.5a shows that the un-coated $LiCoO_2$ has a very clean surface. This agrees with the TEM observations in Figure 4.1b. After coating with ZrO_2, the morphology of the surfaces of $LiCoO_2$ particles has been changed completely. As shown in Figure 4.5b, $LiCoO_2$ particles in sample D are covered by a rough layer. There are also some small particles or flakes between $LiCoO_2$ particles. Even though most of the surfaces of $LiCoO_2$ in sample D are coated by such a layer, the coating is not perfectly

continuous and homogeneous. For example, part of the surface of the particle in the middle of Figure 4.5b seems uncovered, especially the facet facing right on the right side. Figure 4.5c shows that sample E has a very similar morphology to sample D, except that the coating covers more surfaces of the $LiCoO_2$ particles. This is probably because there is 3 wt% more ZrO_2 in sample E than in sample D.

A large part of the coating in both samples D and E seems to be a loose layer formed by nano-particles of a size of about 20 nm. According to the XRD study, both samples D and E contain nanocrystalline ZrO_2. Thus, the coating in Figures 4.5b and 4.5c is probably a layer of ZrO_2 nano-particles.

To further verify that samples D and F are well coated with ZrO_2, EDS was used. An EDS spectrum collected with sample D shows a major signal from Co and a minor signal from Zr. Figure 4.6 shows the EDS dot maps of sample D. Figure 4.6a shows the morphology of a relatively large $LiCoO_2$ particle and other smaller particles around it. Figure 4.6b shows the distribution of Co on the surface of the particles. As expected, Co is evenly distributed on all the particles. Based on the Co distribution and the strong intensity of the EDS signal, each particle in Figure 4.6a is a $LiCoO_2$ particle. Figure 4.6c shows an even distribution of Zr on the particles of $LiCoO_2$. Such an even distribution of Zr indicates that ZrO_2 particles were well coated onto the surface of each $LiCoO_2$ particle. A similar result was obtained for sample E.

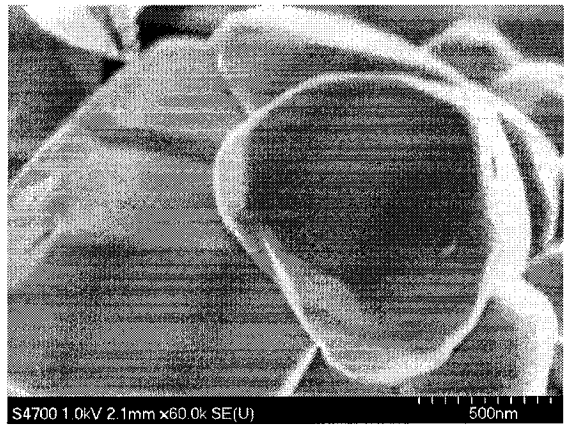

(a)

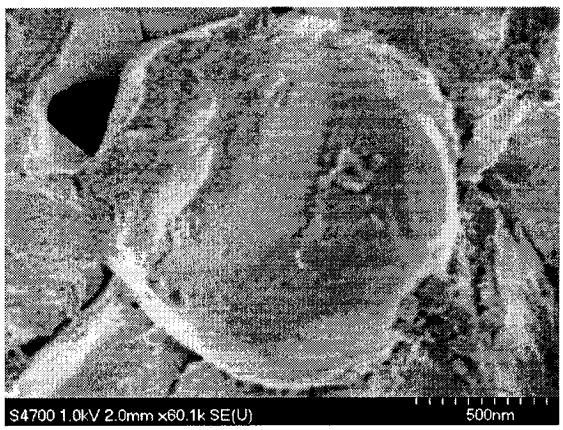

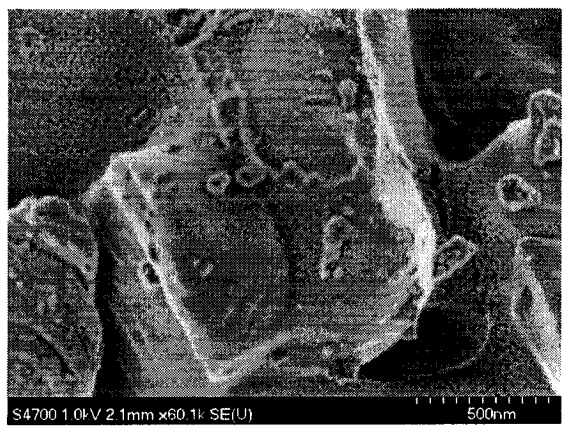

(b) (c)

Figure 4.5 A SEM image of (a) $LiCoO_2$ 010301, (b) sample D, and (c) sample E.

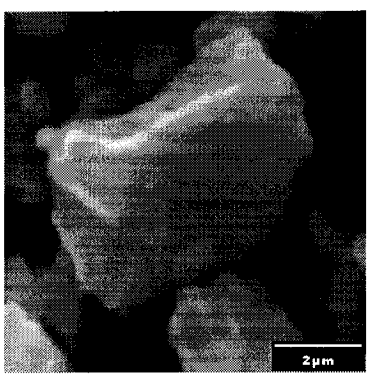

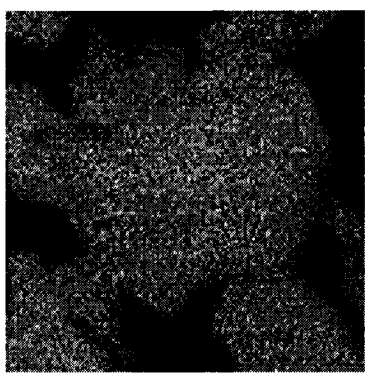

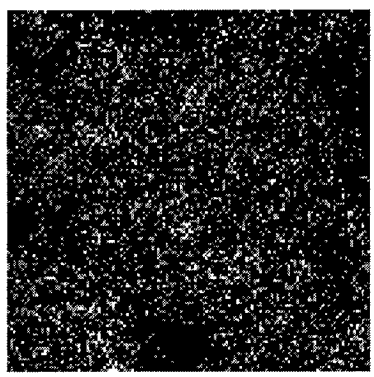

(a) (b) (c)

Figure 4.6 (a) A SEM image of sample D; (b) Co distribution on the surface of particles shown in (a); (c) Zr distribution on the surface of particles shown in (a).

4.3.2.3 TEM characterization of $LiCoO_2$ 010301 coated with ZrO_2

Figure 4.7a clearly shows a layer of nano-particles on the surface of a $LiCoO_2$ particle in sample D. The nano-particles are ZrO_2, based on the above study by XRD and EDS. Figure 4.7b more clearly shows the ZrO_2 particles which have an average size of about 30 nm. Figure 4.8 shows that the morphology of sample E is similar to that of sample D, except that the size of the ZrO_2 particles on the surface of a $LiCoO_2$ particle is smaller, about 10-15 nm. This further confirms that the coating layer observed by SEM in Figures 4.5b and 4.5c is a layer of nano-particles. Thus for both samples D and E, the original smooth surface of $LiCoO_2$ is indeed covered by ZrO_2 nano-particles after coating with ZrO_2.

For both samples, there are some clusters formed by nano-particles which are not on the surfaces of $LiCoO_2$ particles. For example, there are two such clusters in the left side of the $LiCoO_2$ particle in Figure 4.8a. Such excess oxide is also observed by SEM as in Figure 4.5.

4.2.4 Cycling behavior of coated samples

Figure 4.9 shows capacity versus cycle number for samples D, E and the un-coated $LiCoO_2$, 010301. Data sets a and b in Figure 4.9 show the results for the control cells that contain un-coated $LiCoO_2$. When $Li/LiCoO_2$ cells are cycled to only 4.3 V, there is very little capacity loss versus cycle number. However, when the upper cutoff is raised to 4.5 V, the cell with un-coated $LiCoO_2$ exhibits rapid capacity loss, in agreement with previous reports (Wang *et al.*, 2002a and 2002b; Liu *et al.*, 2002; Kannan *et al.*, 2002). Data sets c and d in Figure 4.9 show results for the coated samples D and E, respectively. Apparently, the cells with ZrO_2-coated $LiCoO_2$ show a dramatic

improvement in capacity retention when charged to 4.5 V, obtaining over 170 mAh/g (data set c in Figure 4.9) and over 150 mAh/g after 140 cycles (data set d in Figure 4.9). Since the mass used to calculate the specific capacity of samples D and E is the total mass including both active $LiCoO_2$ and the coating material, ZrO_2, rather than $LiCoO_2$ only, the initial capacity of the coated material is lower than un-coated $LiCoO_2$. However, samples, D and E have much better cycling behavior. This confirms that coating with ZrO_2 improves the cycling behavior of $LiCoO_2$, as reported by Cho *et al.* (2001b).

Sample E has lower capacity than sample D. This is partially because sample E has 3% more ZrO_2 which is electrochemically inactive. In addition, as an insulating powder, more ZrO_2 causes larger impedance in the electrode. With a larger impedance, the electrode may deliver less capacity when it is charged/discharged with a specific current of 47 mA/g.

To investigate the dependence of the capacity retention of ZrO_2 coated $LiCoO_2$ on upper cutoff potential, sample E was cycled with upper cutoff potentials of 4.4, 4.5, 4.6 and 4.7 V respectively. Figure 4.10 shows that, with an upper cutoff potential of 4.4 V or 4.5 V, sample E has an excellent cycling behavior. However, with an upper cutoff potential of 4.6 V or 4.7 V, the capacity fading is unacceptable for industrial applications. Thus, for the testing of other coated materials, 4.5 V was used as the upper cutoff potential.

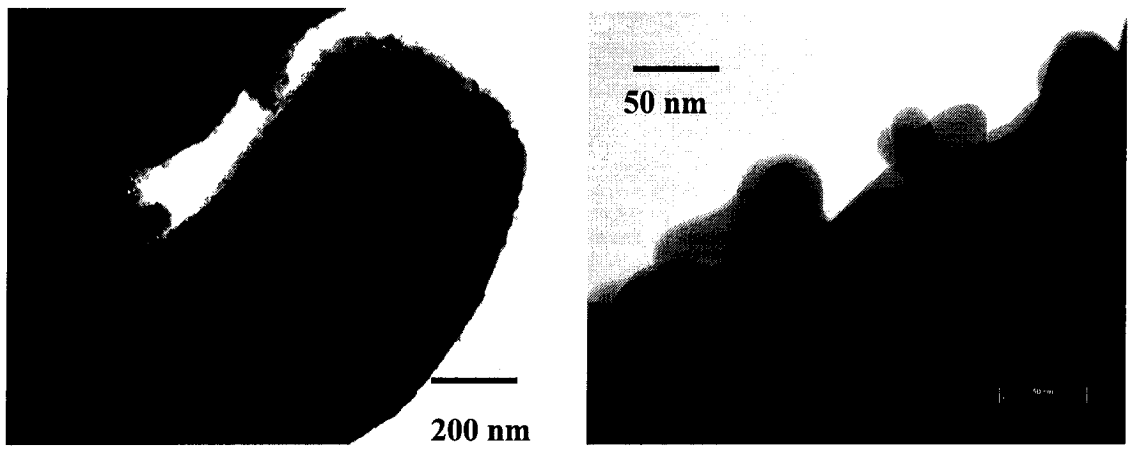

(a) (b)

Figure 4.7 TEM images of sample D with two different magnifications.

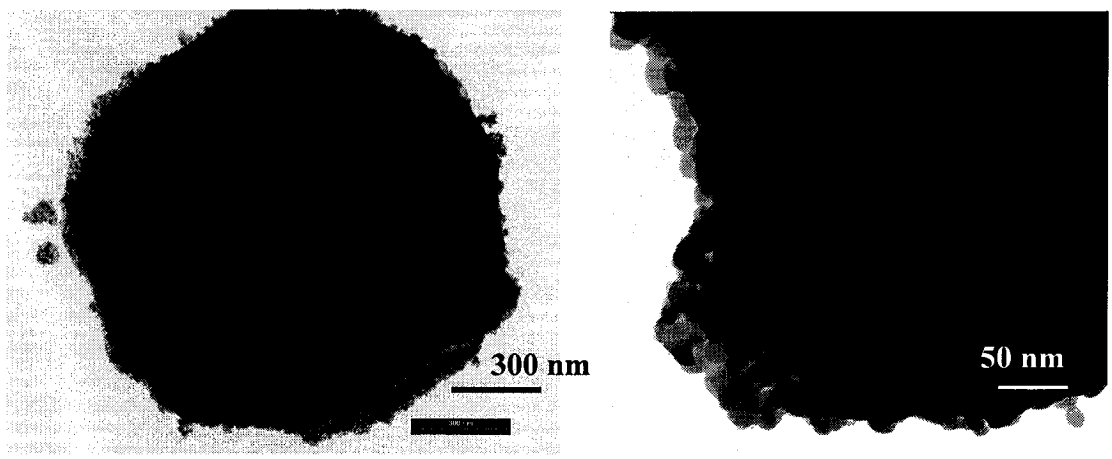

(a) (b)

Figure 4.8 TEM images of sample E with two different magnifications (Chen Z. H. and Dahn J. R., 2002b).

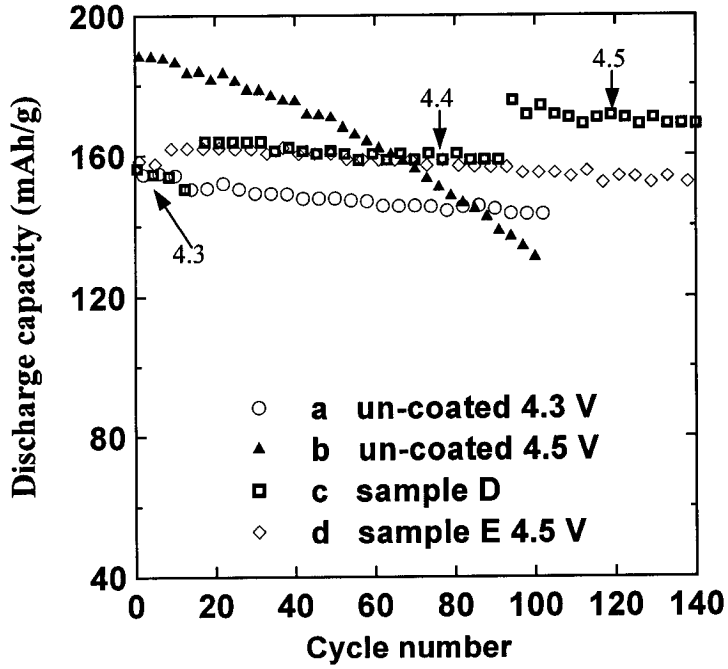

Figure 4.9 Discharge capacity versus cycle number for (a) FMC $LiCoO_2$ 010301 with an upper cutoff of 4.3 V, (b) FMC $LiCoO_2$ 010301 with an upper cutoff of 4.5 V, (c) sample D with an upper cutoff of 4.3 V, then 4.4 V, and finally 4.5 V, and (d) sample E with an upper cutoff of 4.5 V (Chen Z. H. and Dahn J. R., 2002b).

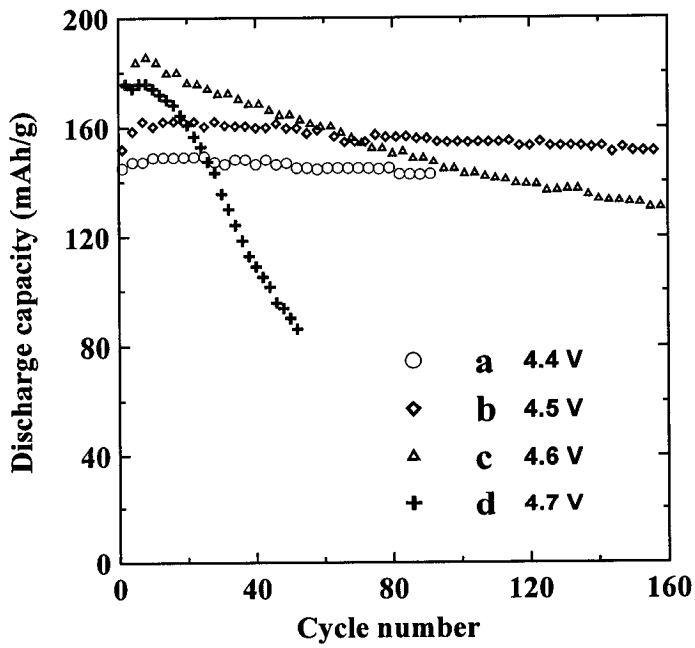

Figure 4.10 Discharge capacity versus cycle number for sample E with an upper cutoff of (a) 4.4 V, (b) 4.5 V, (c) 4.6 V, and (d) 4.7 V.

4.3 $LiCoO_2$ 611061 coated with ZrO_2, Al_2O_3, SiO_2

4.3.1 Morphology of $LiCoO_2$ 611061

To verify that coating also improves $LiCoO_2$ samples from other suppliers, $LiCoO_2$ 611061 from Nippon Chemical Industrial Co. Ltd. was coated with oxides. Compared to $LiCoO_2$ 010301 from FMC, $LiCoO_2$ 611061 has a larger particle size, which varies from about 3 μm to 10 μm. SEM and TEM studies show the surface of $LiCoO_2$ 611061 is also smooth.

4.3.2 Coating precursors

As reported by Cho *et al.* (2001b), the effect of coating on the capacity retention of $LiCoO_2$ depends on the fracture toughness of the oxide used for coating since the coating layer improves the capacity retention of $LiCoO_2$ by preventing $LiCoO_2$ lattice expansion and contraction during cycling. In this study, three oxides were coated onto $LiCoO_2$ 611061 separately with method D. Besides the zirconium oxide polymeric precursor, two other polymeric precursors: aluminum oxide polymeric precursor, and poly(dimethylsiloxane) ($[-SiO(CH_3)_2-]_n$) were used. Figure 4.11 shows that both precursors decompose completely in air above 500°C. Poly(dimethylsiloxane) produces about 35 wt% silicon dioxide after decomposition but the aluminum oxide polymeric precursor gives only about 3.7 wt% aluminum oxide. To compensate for this, the aluminum oxide polymeric precursor was used directly as a coating solution, and Poly(dimethylsiloxane) was diluted by toluene with a 15/85 Poly(dimethylsiloxane)/toluene volume ratio before coating.

XRD experiments were performed on the products from the decomposition of the precursors in air. Figure 4.12a shows that the XRD pattern of the solid resulting from the

decomposition of poly(dimethylsiloxane) has a broad hump centered at 22°. The pattern looks the same as Figure 4.12b, which is a XRD pattern for amorphous fumed SiO_2. Thus, this precursor becomes amorphous SiO_2 after decomposition. Similarly, Figure 4.13 shows that aluminum oxide polymeric precursor becomes amorphous after decomposition.

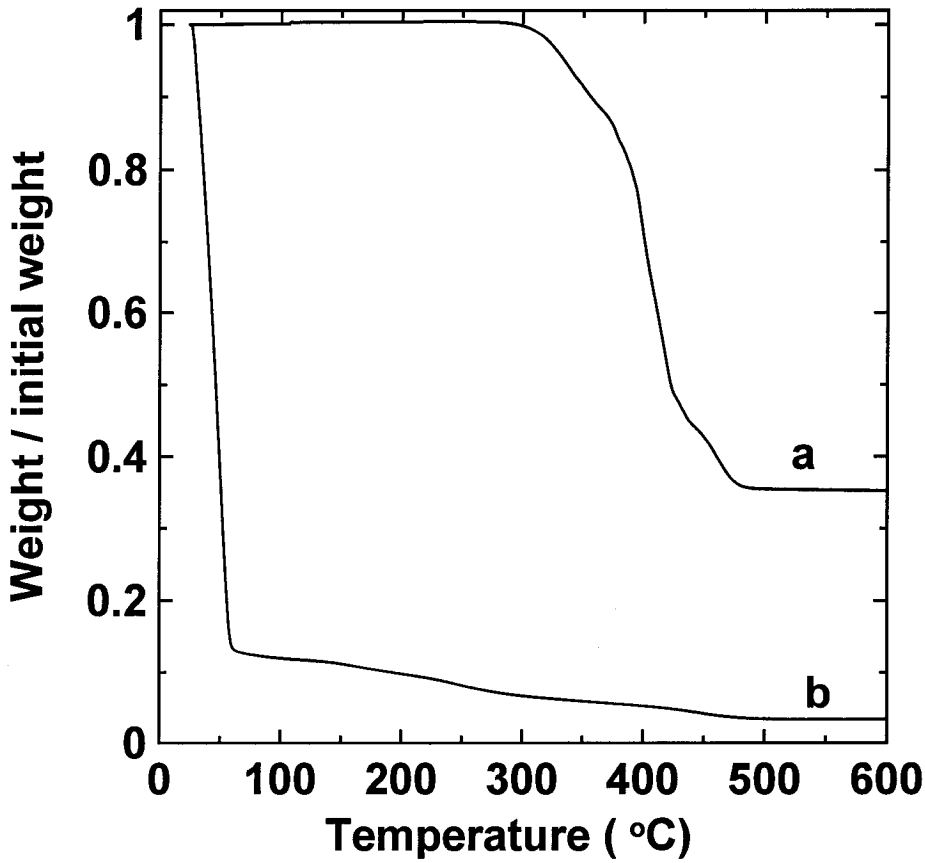

Figure 4.11 Relative weight versus temperature of (a) poly(dimethylsiloxane and (b) aluminum oxide polymeric precursor heated in air at a rate of 5 °C per minute.

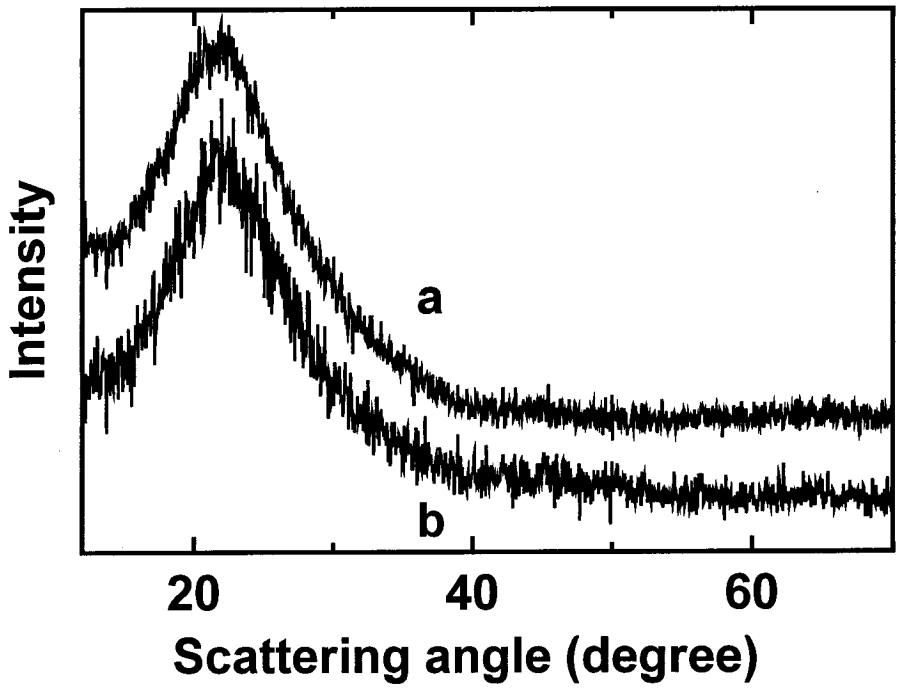

Figure 4.12 XRD pattern of (a) solid remaining from decomposition of poly(dimethylsiloxane) and (b) fumed SiO_2.

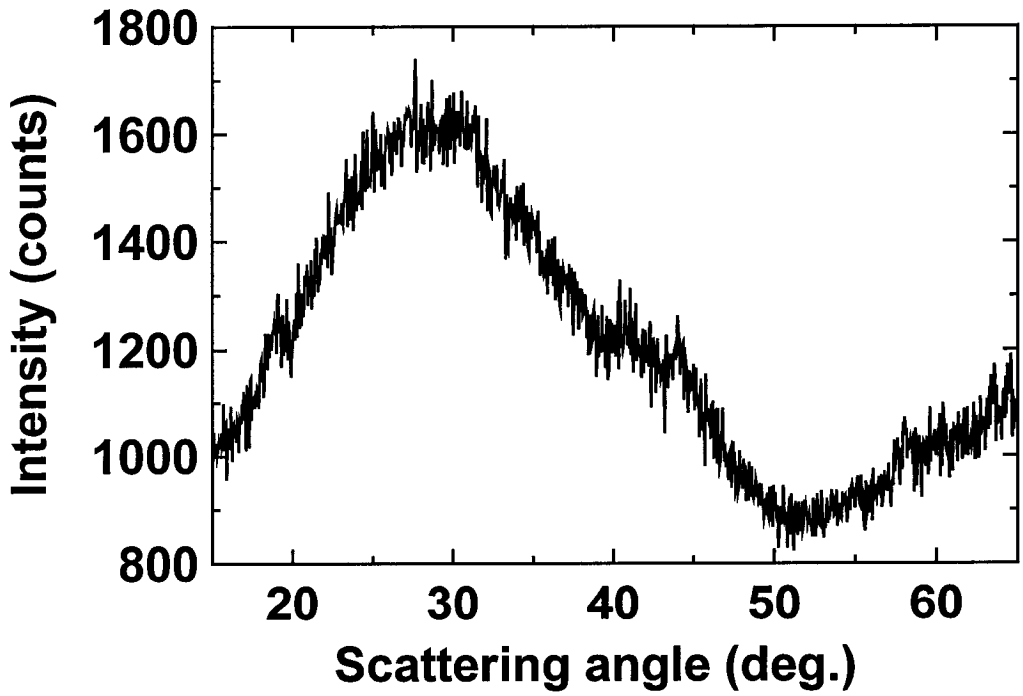

Figure 4.13 XRD pattern of solid remaining from decomposition of aluminum oxide polymeric precursor.

4.3.3 Physical Characterization of $LiCoO_2$ 611061 coated with oxides

4.3.3.1 XRD characterization of coated $LiCoO_2$ 611061

Three samples were prepared by coating $LiCoO_2$ 611061 with the three coating solutions separately. For convenience, the samples that were coated with zirconium oxide polymeric precursor, aluminum oxide polymeric precursor, and poly(dimethylsiloxane) are called samples F, G, and H, respectively. There is 5.5 wt% ZrO_2, 1.5 wt% Al_2O_3, and 1.5 wt% SiO_2 in samples F, G, and H respectively.

Slow XRD scans were taken for samples F, G, H and $LiCoO_2$ 611061. Figure 4.14 shows the XRD patterns for these four samples. The y-axes in Figure 4.14 use a logarithmic scale. In Figure 4.14b, there are three small, broad peaks from ZrO_2 in addition to the dominant peaks from $LiCoO_2$. This indicates that coating $LiCoO_2$ with zirconium oxide polymeric precursor results in nano-particles of ZrO_2 in sample F. However, unlike in sample E, both monoclinic and tetragonal ZrO_2 phases are present in sample F instead of only the tetragonal ZrO_2 phase.

Figures 4.14c and 4.14d look the same as Figure 4.14a. Thus, by XRD study, it is not certain that either Al_2O_3 or SiO_2 were coated onto $LiCoO_2$ 611061 in samples G and H. Since poly(dimethylsiloxane) and aluminum oxide polymeric precursor decompose to amorphous oxides, which are difficult to detect by XRD when the weight percentage is small, it is possible that the coating resulted in amorphous SiO_2 or Al_2O_3 on the surfaces of $LiCoO_2$ 611061 particles.

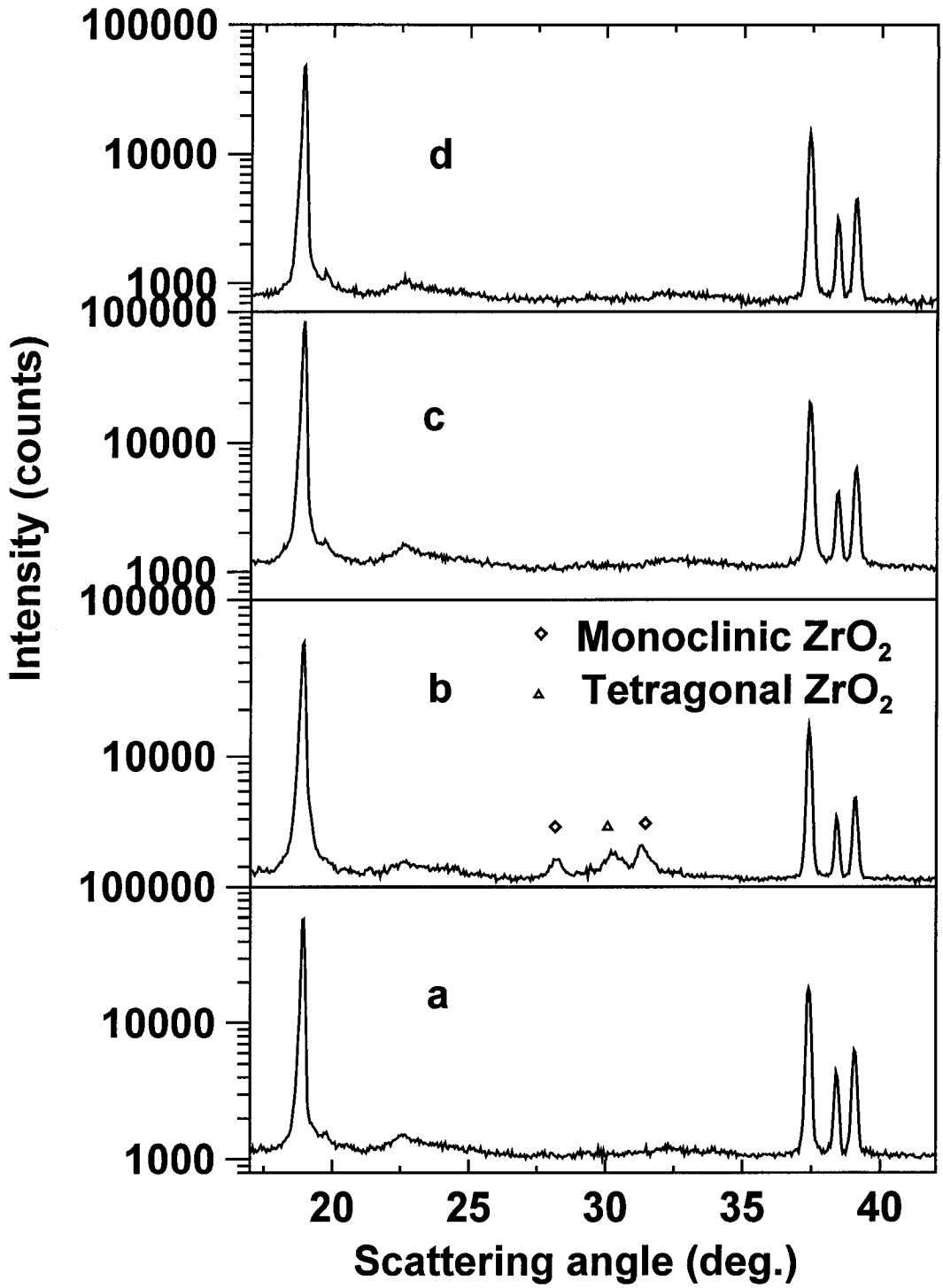

Figure 4.14 XRD pattern of (a) $LiCoO_2$ 611061, (b) sample F, (c) sample G, and (d) sample H.

4.3.3.2 Characterization of coated $LiCoO_2$ 611061 by TEM, SEM and EDS

Figure 4.15 shows SEM images of the four samples. Like $LiCoO_2$ 010301, $LiCoO_2$ 611061 has a very clean looking surface. In all three coated samples, $LiCoO_2$ particles are covered by the corresponding oxide. Besides the coating, there are also extra oxide particles or flakes lying on or around the $LiCoO_2$ particles. Such a morphology is similar to that of samples D and E.

EDS dot mapping results for samples G and H show a homogeneous distribution of Co in both samples. Figure 4.16b shows an even distribution of Al on the surface of particles in sample G. Figure 4.17b shows an even distribution of Si on the surface of particles in sample H. Hence, in both samples G and H, the $LiCoO_2$ particles are well coated with oxide even though there is also excess oxide present.

Using the TEM, clear images of the surfaces of samples G and H were obtained. Figures 4.18a and 4.18b show that, for both samples the coatings cover almost the whole surface of the $LiCoO_2$ particles except for the lower left corner of the particle in 4.18a. However, the coated layer on the surface of both samples does not look like a continuous, smooth, strong layer. Similar to the SEM results, for both samples excess coating oxide, not intimately covering $LiCoO_2$, was observed by TEM.

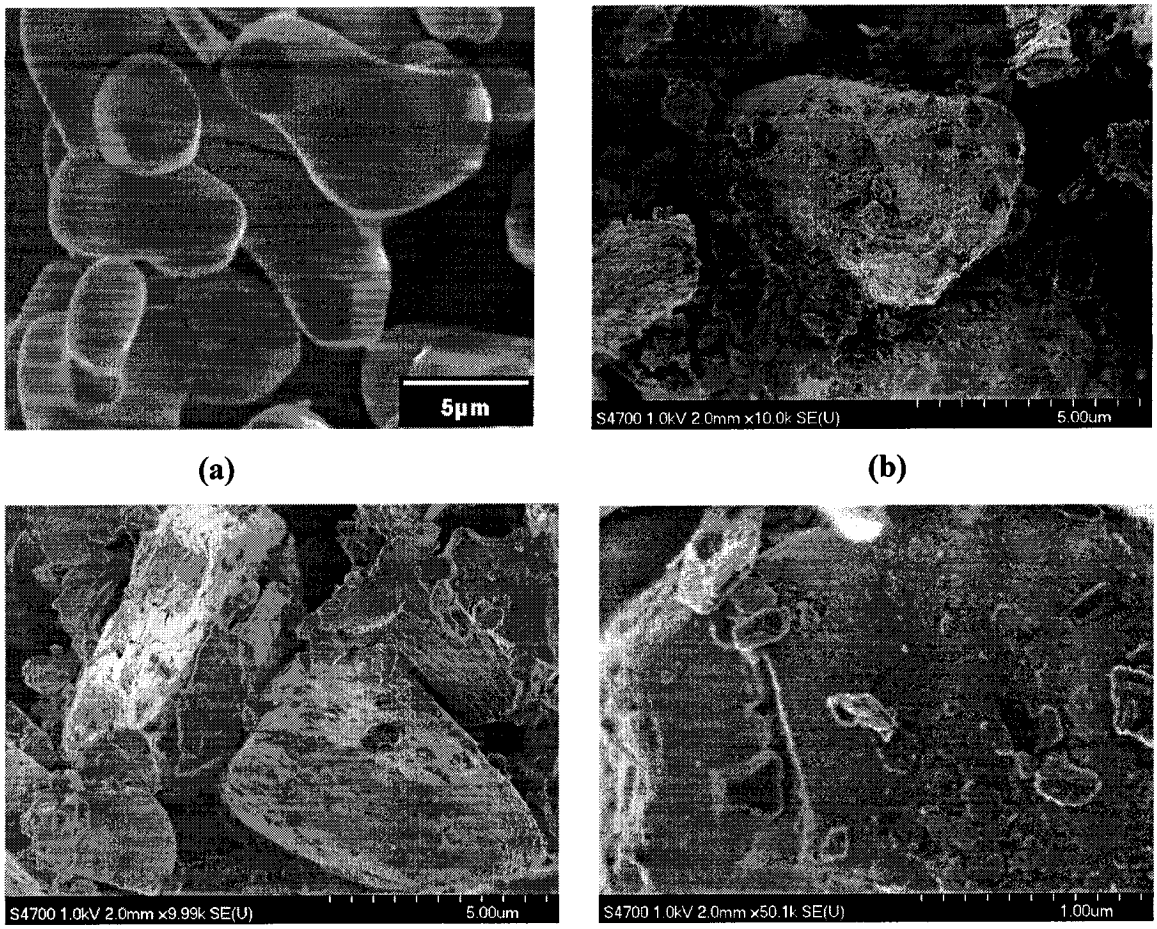

(a) (b)

(c) (d)

Figure 4.15 A SEM image of (a) $LiCoO_2$ 611061, (b) sample F, (c) sample G, and (d) sample H.

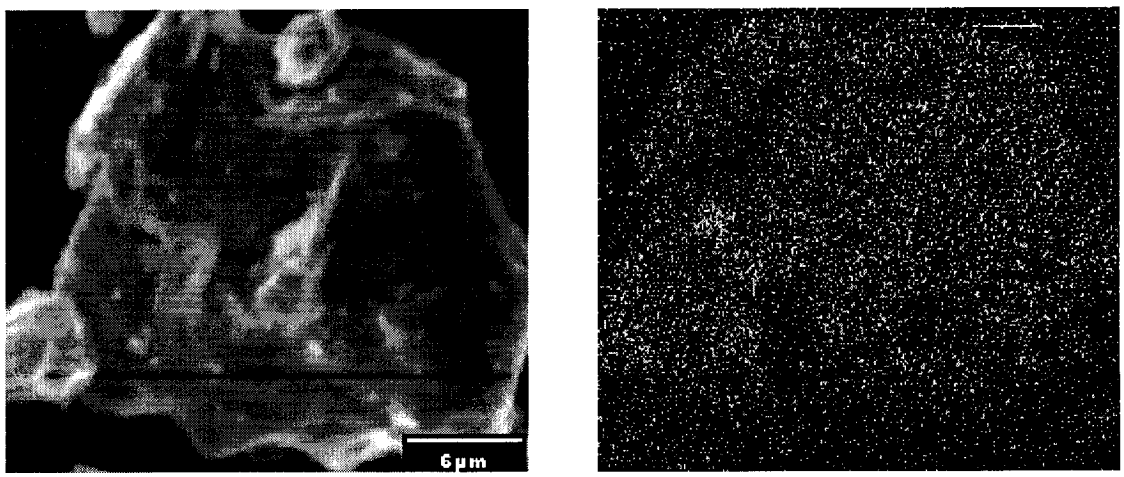

(a) (b)

Figure 4.16 (a) A SEM image of sample G and (b) Al distribution on the surface of $LiCoO_2$ particles shown in (a).

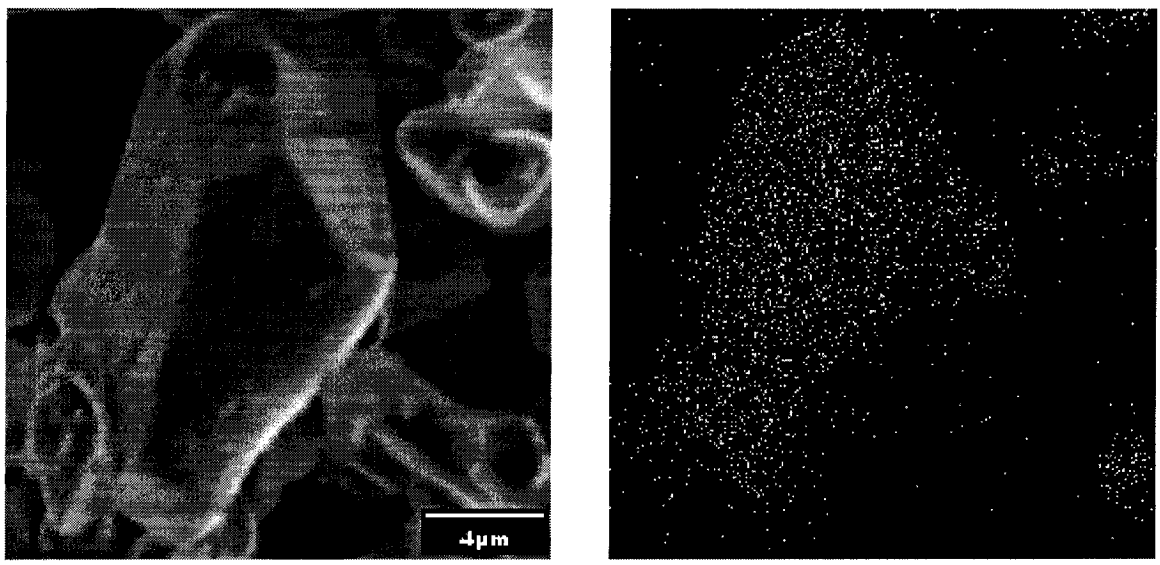

(a) (b)

Figure 4.17 (a) A SEM image of sample H and (b) Si distribution on the surface of $LiCoO_2$ particles shown in (a).

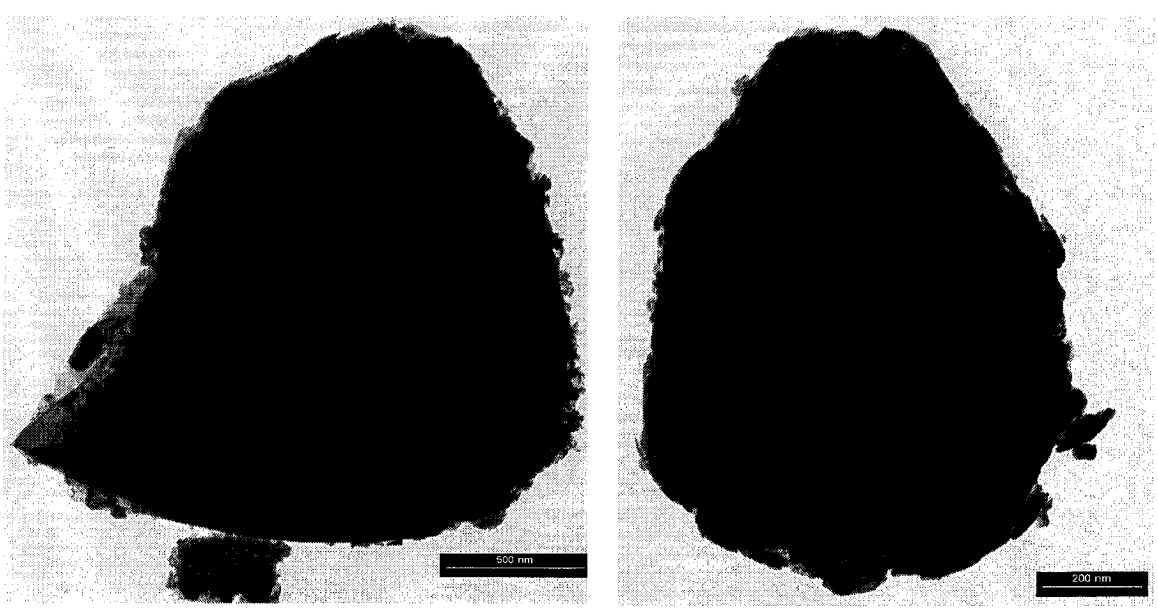

(a) (b)

Figure 4.18 A TEM image of a particle in (a) sample G and (b) sample H.

4.3.4 Electrochemical characterization of coated $LiCoO_2$ 611061

Figure 4.19 shows that samples F, G, and H have much better capacity retention than un-coated $LiCoO_2$ 611061 when cycled to 4.5V. Sample G, which was coated with Al_2O_3, has the best cycling behavior. $LiCoO_2$ 611061 has a lower capacity than $LiCoO_2$ 010301 when cycled to 4.5V. This lower capacity is probably due to the larger impedance of the material.

From the five coated samples D, E, F, G, and H, it is clear that coating with any one of the three oxides improves the capacity retention of $LiCoO_2$ when cycled to 4.5V, and that $LiCoO_2$ coated with ZrO_2 is not necessarily the material with the best capacity retention.

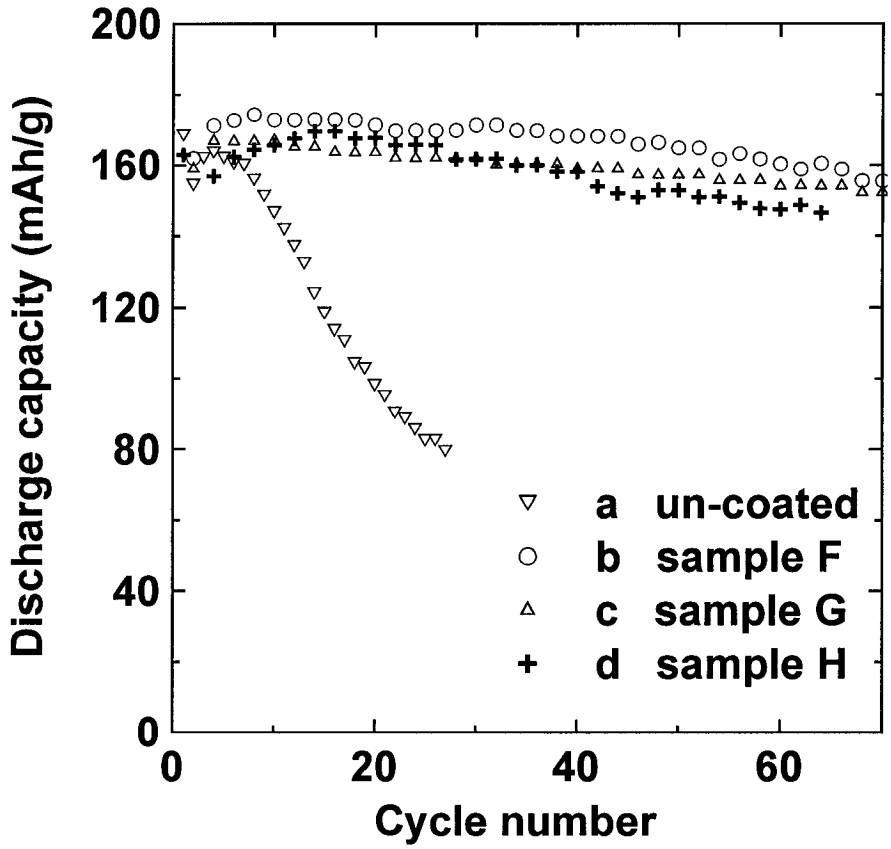

Figure 4.19 Discharge capacity versus cycle number for (a) un-coated $LiCoO_2$ 611061, (b) sample F, (c) sample G, and (d) sample H with an upper cutoff of 4.5 V.

4.4 $LiCoO_2$ 010301 coated with ZrO_2, Al_2O_3 and SiO_2 by method E

All the coatings shown above have a loose appearance and do not seem very strong. Excess coating oxide was observed in each coated sample. To make better coatings, method E was used. Using method E, $LiCoO_2$ 010301 was coated with the three oxides using the three coating solutions used in 4.3. In this method, excess coating solution was used to get good coverage by the coating solution on each $LiCoO_2$ particle. A surfactant was added during the mixing to improve intimate contact between the $LiCoO_2$ surface and the polymer in the coating precursor. After mixing, excess coating solution was removed by centrifugation. For convenience, the samples coated with ZrO_2, Al_2O_3, and SiO_2 are called samples I, J and K respectively.

4.4.1 Physical Characterization of $LiCoO_2$ 010301 coated with oxides

4.4.1.1 XRD characterization of $LiCoO_2$ 010301 coated with oxides

Figure 4.20 shows the XRD patterns of the three coated $LiCoO_2$ samples and $LiCoO_2$ 010301. The intensity in Figure 4.20 is plotted with a logarithmic scale to allow weak peaks, if any, from the coated oxides to be observed. In the XRD pattern of sample I ($LiCoO_2$ coated with ZrO_2), besides the dominant peaks from $LiCoO_2$, one can see a small broad peak at about 30 degrees. This Bragg peak is the (111) peak from tetragonal ZrO_2, indicating that the coating procedure resulted in nanocrystalline ZrO_2 in the coated material. By contrast, the XRD patterns of samples J and K, coated with Al_2O_3 and SiO_2 respectively, appear to be the same as that of un-coated $LiCoO_2$. The coating may be amorphous, as in samples F and G.

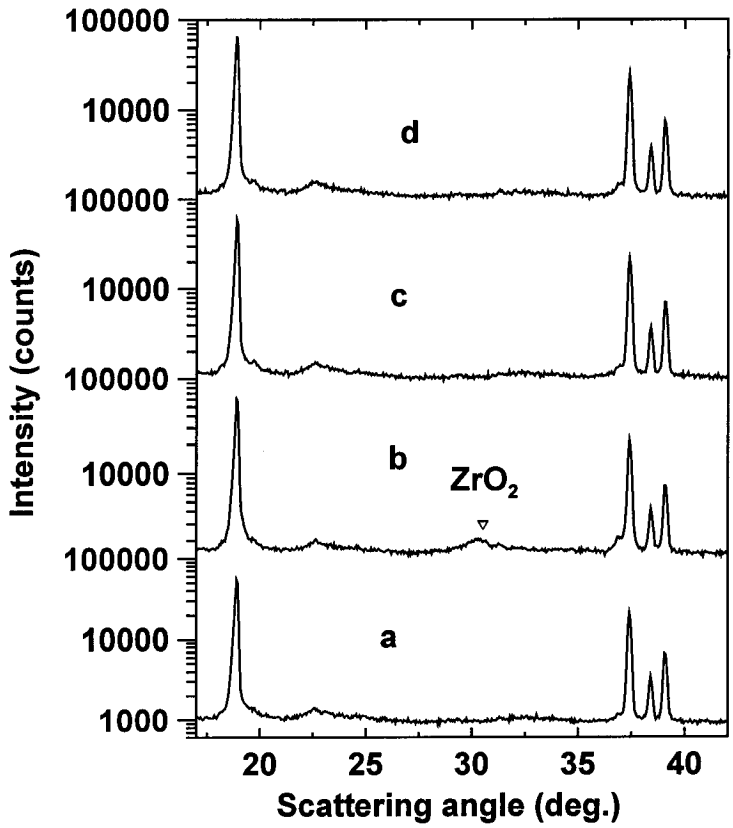

Figure 4.20 XRD pattern of (a) $LiCoO_2$ 010301, (b) sample I, (c) sample J, and (d) sample K (Chen Z. H. and Dahn J. R., 2003a).

4.4.1.2 TEM characterization of $LiCoO_2$ 010301 coated with oxides

Figure 4.21a shows that after coating, the surface of sample I is covered with particles with a diameter of about 10 nm. The coating layer appears rough. TEM images of samples J and K show smooth surfaces similar to those of $LiCoO_2$ 010301 before coating. Figure 4.21b shows an example particle of sample K. Since method E was used for samples G and H to make a better coating, with adhesion promoter and centrifugation, a very smooth and continuous oxide layer should have coated the surface of the $LiCoO_2$ particles in both samples. However, based on XRD and TEM studies, one can not conclude that oxide was successfully coated onto the surface of $LiCoO_2$ in samples J and K.

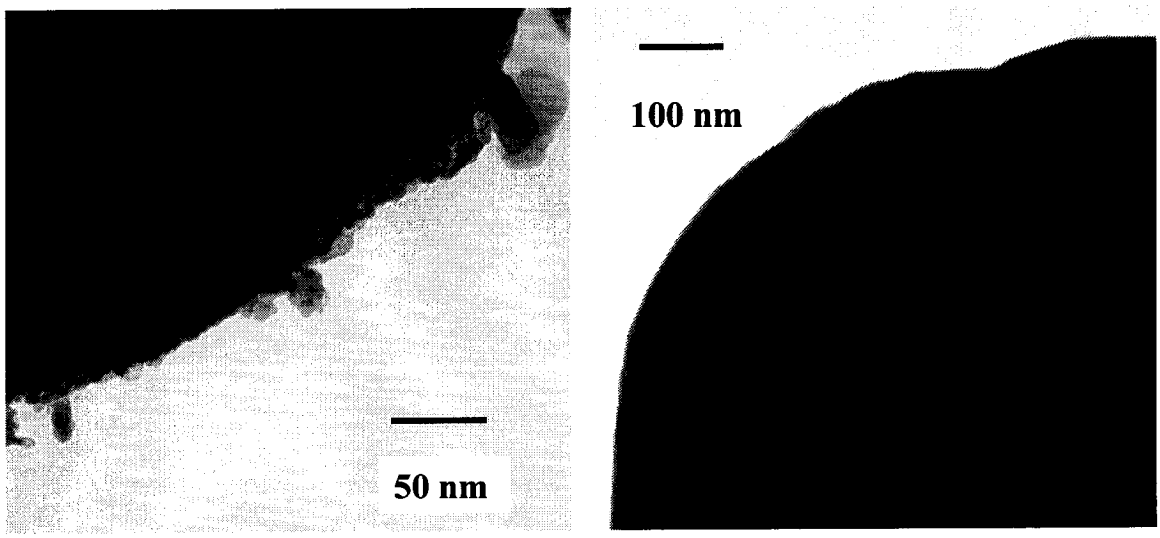

(a) **(b)**

Figure 4.21 A TEM image of (a) sample I and (b) sample K.

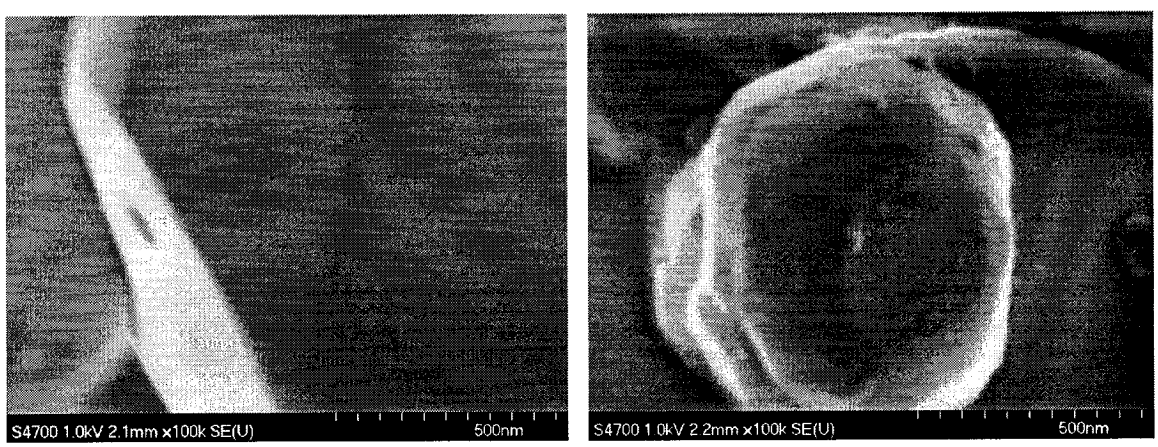

(a) **(b)**

Figure 4.22 A SEM image of (a) sample J and (b) sample K.

4.4.1.3 SEM and EDS dot mapping characterization of $LiCoO_2$ 010301 coated with oxides

Similar to TEM results, a smooth particle surface was observed by SEM for samples J and K. Figure 4.22a shows that the surface of sample J is as smooth as that of $LiCoO_2$ 010301, which is shown in Figure 4.5a. Figure 4.22b shows that sample K has a fairly clean surface except for some small bumps scattered on the surface.

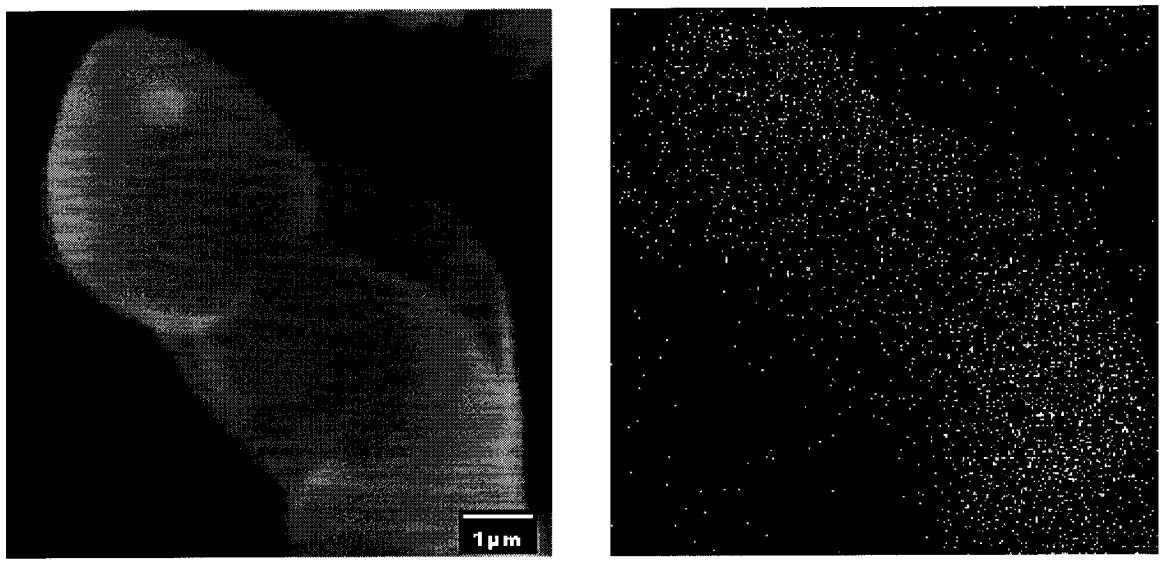

(a) **(b)**

Figure 4.23 (a) A SEM image of sample K and (b) EDS dot map of Si on the particles shown in (a) (Chen Z. H. and Dahn J. R., 2003a).

EDS dot mapping was then used to verify whether there was any Si or Al on the surface of the two coated samples. Figure 4.23a shows an SEM image of sample K, $LiCoO_2$ particles coated with SiO_2. Figure 4.23b shows an even distribution of Si on the surfaces of the particles. EDS dot mapping of sample J also shows an even distribution of Al on the surface of the $LiCoO_2$ particles. Figures 4.12a and 4.13 show that poly(dimethylsiloxane) and aluminum oxide polymeric precursor become amorphous

after decomposition and Bragg peaks from SiO_2 or Al_2O_3 are not found in $LiCoO_2$ coated with these materials (Figure 4.20). Coating on $LiCoO_2$ 610611 for samples G and H resulted in amorphous Al_2O_3 and SiO_2 flakes on $LiCoO_2$ surface as shown by SEM (Figure 4.15 c and 41.5 d). With the same precursor and the same heating temperature, coatings on $LiCoO_2$ 010301 for samples J and K possibly also resulted in amorphous Al_2O_3 and SiO_2 on the $LiCoO_2$ surface rather than the formation of $LiAl_xCo_{1-x}O_2$ or $LiSi_xCo_{1-x}O_2$ as proposed by Cho *(Cho et al., 2000b)*.

Since smooth surfaces of samples J and K were observed with TEM and SEM, the coating layer must be a very smooth layer on the surface of $LiCoO_2$. In samples J and K, excess coating oxides were eliminated. Therefore, method E did result in a better coating than method D for coating with SiO_2 and Al_2O_3.

4.4.2 Electrochemical characterization of $LiCoO_2$ 010301 coated with oxides

Electrochemical characterization can verify whether materials coated by method E really have higher capacity and better capacity retention as hoped. Figure 4.24 shows the capacity versus cycle number for samples I, J, K, and $LiCoO_2$ 010301. Even with a lower cutoff potential of 3.6 V, the capacity retention of any one of the coated $LiCoO_2$ samples is excellent. For example, sample J ($LiCoO_2$ coated with aluminum oxide) delivers a capacity of 175 mAh/g even after 140 cycles.

Figure 4.24 shows that the capacity retention of a coated $LiCoO_2$ sample is basically independent of the metal oxide used. This is contrasted with the large differences in capacity retention of $LiCoO_2$ samples coated with different oxides reported by Cho *et al.* (2001b), which were correlated with the relative fracture toughness of the oxides. In reference 8, coating with ZrO_2 gives significantly better capacity retention

than coating with Al_2O_3 and other metal oxides. On the contrary, coating with Al_2O_3 gives slightly better cycling behavior here. Therefore, the mechanism for the capacity retention improvement proposed by Cho *et al.* is incorrect.

Both samples I and E are $LiCoO_2$ 010301 coated with zirconium oxide polymeric precursor. Compared with Figure 4.9d, Figure 4.24b shows similar excellent capacity retention. In addition, both samples have almost the same specific capacity. So for coating with zirconium polymeric precursor, methods D and E gave almost the same result.

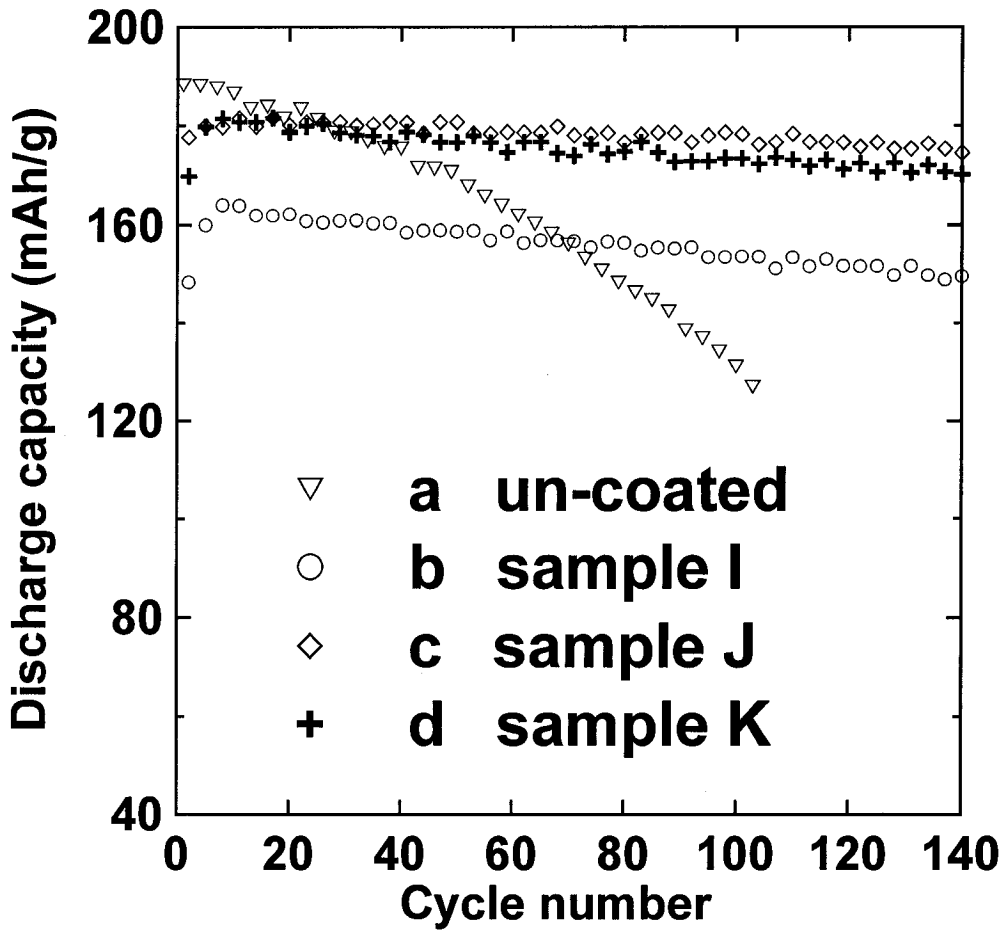

Figure 4.24 Specific capacity versus cycle number for (a) $LiCoO_2$ 010301 before coating, (b) sample I, (c) sample J, and (d) sample K (Chen Z. H. and Dahn J. R., 2003a).

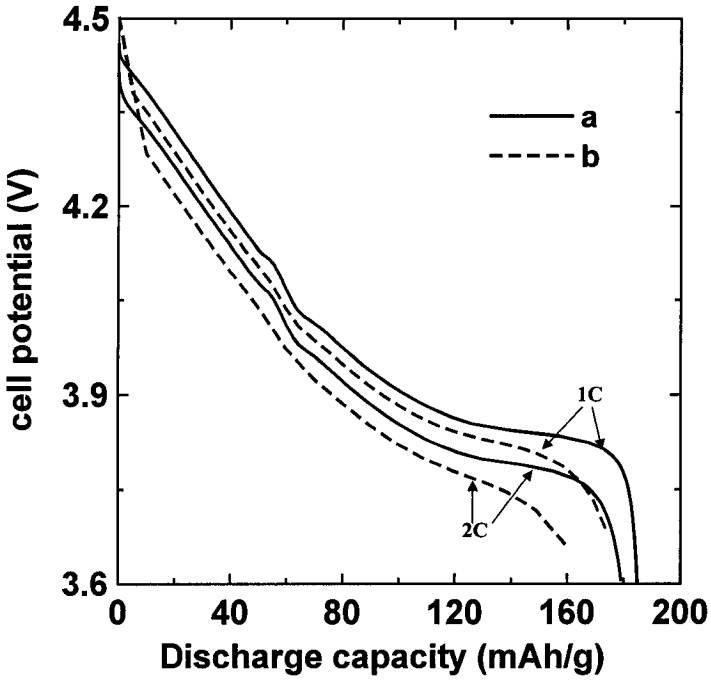

Figure 4.25 Voltage curves of (a) $LiCoO_2$ 010301 and (b) sample J discharged at a 1C or a 2C rate.

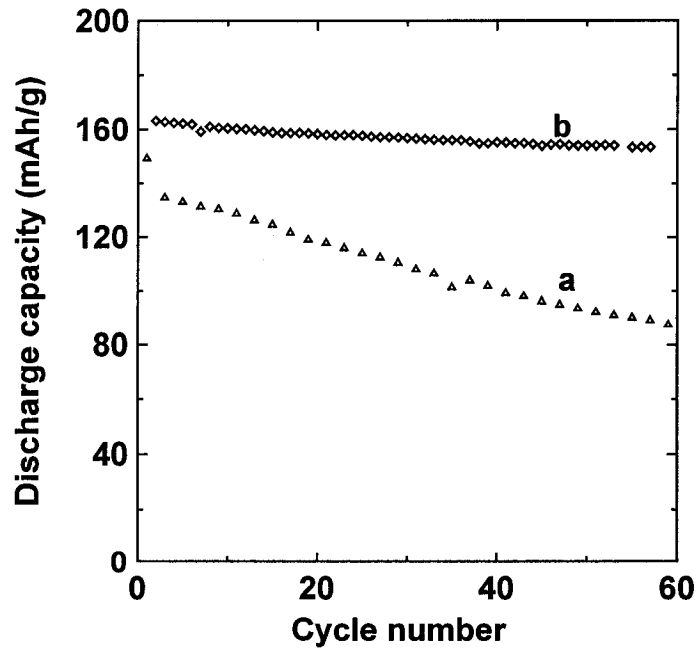

Figure 4.26 Specific capacity versus cycle number for (a) $LiCoO_2$ 611061 and (b) sample F cycled between 3.3 V and 4.4 V in a Li-ion cell.

With aluminum oxide polymeric precursor or poly(dimethylsiloxane), method E made excellent materials (samples J and K). As shown above by TEM (Figure 4.21b) and SEM (Figure 4.22a and 4.22b) studies, the coatings are smooth. There is no excess oxide left in either sample. Samples J and K deliver an initial capacity of more than 180 mAh/g.

Figure 4.25 shows the voltage curves of $LiCoO_2$, before and after coating with aluminum oxide, discharged at a 1C (140 mA/g) or 2C (280 mA/g) rate. The lower average potential for the coated sample indicates that the aluminum oxide coating causes a slight degradation in the rate capability of $LiCoO_2$. This degradation is probably due to larger surface impedance caused by the insulating oxide layer on the $LiCoO_2$ surface. By contrast, according to Cho *et al.* (2001a), the oxide coating also enhances the rate capability of $LiCoO_2$.

4.5 Capacity retention of coated $LiCoO_2$ in a Li-ion cell

Since the purpose of coating $LiCoO_2$ with oxide was to improve the energy density of Li-ion batteries, coated materials were also tested in Li-ion cells with meso carbon microbead (MCMB) electrodes as anodes. Figure 4.26 shows the capacity retention of sample F as an example. It is clear that, even in a Li-ion cell, coating with ZrO_2 improves the capacity retention of $LiCoO_2$.

4.6 Summary

Both $LiCoO_2$ samples used for coating were successfully coated with ZrO_2, Al_2O_3, and SiO_2. In the coated $LiCoO_2$ samples, ZrO_2 is present as nanocrystalline particles with a diameter of 10-30 nm, while Al_2O_3 and SiO_2 probably exist as an

amorphous phase. For all the coated samples, most of the surface of $LiCoO_2$ is covered with the coating. Some bare surface was observed, such as sample D as shown in Figure 4.5b. Except for samples J and K, coatings in other coated samples are not smooth and continuous.

Unlike for Cho *et al.*'s coatings on $LiCoO_2$, the capacity retention is independent of the fracture toughness of the coated oxide. Regardless of whether the coating layer is continuous and smooth or rough, and no matter which oxide is used for coating, any coated $LiCoO_2$ sample has an excellent capacity retention when charged to 4.5 V, even with a lower cutoff potential of 3.6 V. This proves that the coating improves the capacity retention of $LiCoO_2$ in some way other than preventing $LiCoO_2$ from expansion during cycling as proposed by Cho *et al.* (2001b).

With method E and aluminum oxide polymeric precursor or poly(dimethylsiloxane) as the coating precursor, materials with high capacity and excellent capacity retention were obtained. For example, $LiCoO_2$ coated with aluminum oxide delivers an initial specific capacity of 180 mAh/g with only a 3% loss over 140 cycles. The coating causes a slight degradation in rate capability instead of enhancing the rate capability as reported by Cho *et al.* (2001a).

Chapter 5 Understanding the effect of coating

5.1 Introduction

Chapter 4 demonstrated that $LiCoO_2$ samples coated with oxides have excellent capacity retention when cycled to 4.5 V with respect to Li metal, even with a lower cutoff as high as 3.6V. On one hand, our results confirm the results of Cho *et al.* (1999, 2000a, 2000b, 2001a, and 2001b) and other groups afterwards (Wang *et al.*, 2002a and 2002b; Liu *et al.*, 2002; Kannan *et al.*, 2002) and show further improvements to specific capacity and capacity retention of $LiCoO_2$ by coating with oxides. On the other hand, the mechanism for this improvement of the capacity retention is probably not suppression of structural instabilities as proposed by Cho and other researchers.

To investigate the effects on lattice expansion of $LiCoO_2$ by the oxide coating layer during a charge, *In-situ* X-ray diffraction was used to study an electrode made from sample E, a $LiCoO_2$ sample coated with ZrO_2. Contrary to the results of Cho *et al.* (2001), it was found that the lattice of coated Li_xCoO_2 expands just like un-coated Li_xCoO_2 as x is changed. Thus, the coating must work in some other way to improve the specific capacity and capacity retention of $LiCoO_2$.

In order to understand the mechanism for the improvement in capacity retention by oxide coating, it is useful first to understand the reason for capacity fading when $LiCoO_2$ is cycled above 4.2 V. This chapter also describes efforts made to understand why capacity fading occurs so rapidly when $LiCoO_2$ cycled above 4.2V. Based on the understanding of the capacity fading, the mechanism of the improvement by the coating

was understood. Furthermore, other approaches to improve capacity retention were developed.

5.2 An *In-situ* XRD study of $LiCoO_2$ coated with ZrO_2

In order to determine the effect of the oxide coating on the lattice expansion of $Li_{1-x}CoO_2$ during a charge, an *in-situ* XRD experiment on sample E was performed. During the charge, 13 XRD patterns were collected sequentially. There are two small plateaus in the 4.1 to 4.2 V range. These two plateaus correspond to the order/disorder transition that normally occurs during the charge of $Li/LiCoO_2$ cells (Reimers and Dahn, 1992).

Figure 5.1 shows the evolution of the XRD pattern in the scattering angle range between 58° and 67° during the charge. For clarity, each scan is offset by 300 counts from the previous scan. The splitting and intensity evolution of the (107) and (108) peaks during scans 3, 4, and 5 indicates that Li_xCoO_2 undergoes a first-order phase transition near the beginning of the charge, as is expected (Reimers and Dahn, 1992). The shifts of the (107) and (108) peaks to lower angle indicate that the *c*-axis of Li_xCoO_2 is expanding during the charge. There is also a slight shift of the (110) peak to higher angle during this period, which indicates that the *a*-axis of Li_xCoO_2 is contracting slightly. The splitting of the 107 peak near 127 mAh/g is caused by the order-disorder transition (Reimers and Dahn, 1992).

Figure 5.2 shows the lattice constants plotted versus capacity. The lattice constants were determined by least-square fitting to the measured positions of the Bragg peaks. Data for un-coated $LiCoO_2$ (Reimers and Dahn, 1992) are also included in the

figure. The results agree well with those reported on un-coated Li_xCoO_2 (Reimers and Dahn, 1992), proving that at least this ZrO_2 coating does not suppress the lattice expansion of Li_xCoO_2. The *in-situ* XRD results confirm the suspicion about Cho *et al.*'s explanation (Cho *et al.*, 2001b) discussed in Chapter 1. The coated materials tested here are not "zero strain" positive electrode materials, yet they still show improved cycling behavior to 4.5 V compared to un-coated materials.

Based on a TEM study, Wang (1999) claimed that individual $LiCoO_2$ particles in an electrode cycled 4.35 V versus Li metal are subject to widely varying degrees of damage which causes capacity fading. Based on study here, such structural damage is not typical for $LiCoO_2$ cycled to 4.5 V or does not necessarily cause capacity fading.

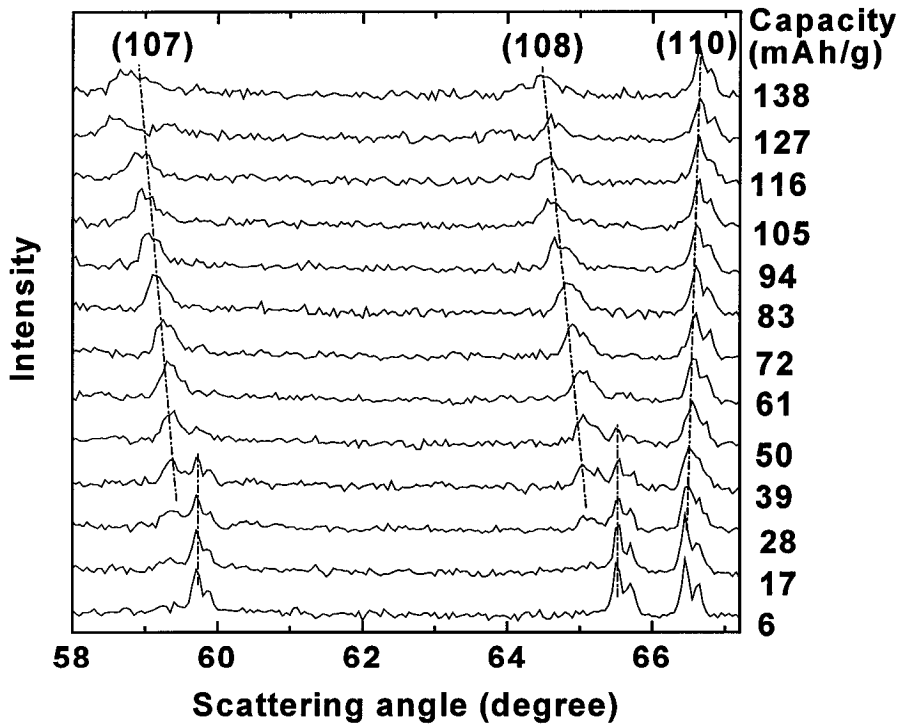

Figure 5.1 In-situ XRD patterns of the cathode made from sample E collected sequentially during the first charge. The scattering angle range between 58° and 67° is shown (Chen Z. H. and Dahn J. R., 2002b).

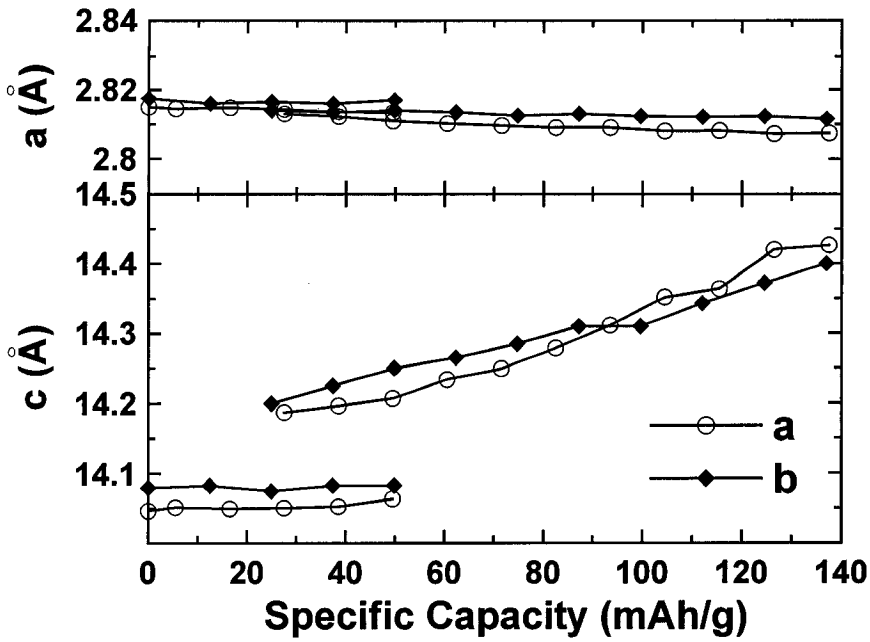

Figure 5.2 (a) The lattice constants, a and c, measured from the XRD patterns collected during the first charge. The measurements were made on ZrO_2-coated $LiCoO_2$ (sample E). (b) Data for un-coated $LiCoO_2$, from (Reimers and Dahn, 1992).

5.3 Impedance growth in cells repeatedly cycled to 4.5V

The inset of Figure 5.3 shows that $LiCoO_2$ 010301 has an initial specific capacity of about 180 mAh/g when cycled to 4.5 V. This is about 30% more than that used in a typical commercial Li-ion cell. However, the capacity fades quickly upon cycling, even with a lower cutoff potential of 3.0 V. Figure 5.3 shows the differential capacity plotted versus cell potential for cycle 5 and for cycle 100. For the first several cycles, the peaks corresponding to the phase transition between the two O3 phases during charge (at 3.92 V) and during discharge (at 3.88 V) are narrow and sharp. During extended cycling, these peaks becomes broader and broader and the charge and discharge peaks shift farther and farther apart. Figure 5.3 shows that after 100 cycles, the peak during charge becomes a very broad hump above 4.0V. The peak during discharge shifts far below 3.6 V and is

outside the range of the graph. Figure 5.3 shows that the impedance in the cell increases dramatically during the first 100 cycles. Because of the impedance growth, more and more discharge capacity of the cell shifts below the lower voltage cutoff. As a result, its measured discharge capacity above 3.0 V is reduced.

On the contrary, a similar impedance growth is not observed in cells using sample K, $LiCoO_2$ 010301 coated with SiO_2, as the positive electrode. Figure 5.4 shows that the differential capacity versus cell potential curve does not change significantly even after 100 cycles for the coated material. Therefore this coated $LiCoO_2$ has much better capacity retention, as shown by the inset of Figure 5.4.

Instead of a layer of a $LiZr_{1-x}Co_xO_2$ as proposed by Cho *et al.* (2001b), a ZrO_2 coating results in a layer of nanocrystalline ZrO_2 on the surface of $LiCoO_2$ (chapter 4). This nanocrystalline ZrO_2 layer does not suppress the lattice expansion and phase transitions of $LiCoO_2$ during charge-discharge cycling at all. Therefore, coating does not change the bulk properties of $LiCoO_2$, but it could change its surface properties. Figure 5.4 shows that whatever the changes to the surface, the impedance growth in the cell during the first 100 cycles is suppressed. Therefore, the impedance growth must be caused by some side reactions involving the surface of un-coated $LiCoO_2$. According to Aurbach *et al.* (2002), upon cycling or storage at elevated temperature, the capacity loss of $LiCoO_2$ electrodes cycled to 4.2 V is caused by the formation of surface films that cover the particles and may electronically isolate them from each other and from the current collector. When $LiCoO_2$ is cycled to 4.5 V, such an electronically resistive surface film may form even faster and cause quicker capacity loss than when the electrode is cycled to 4.2 V.

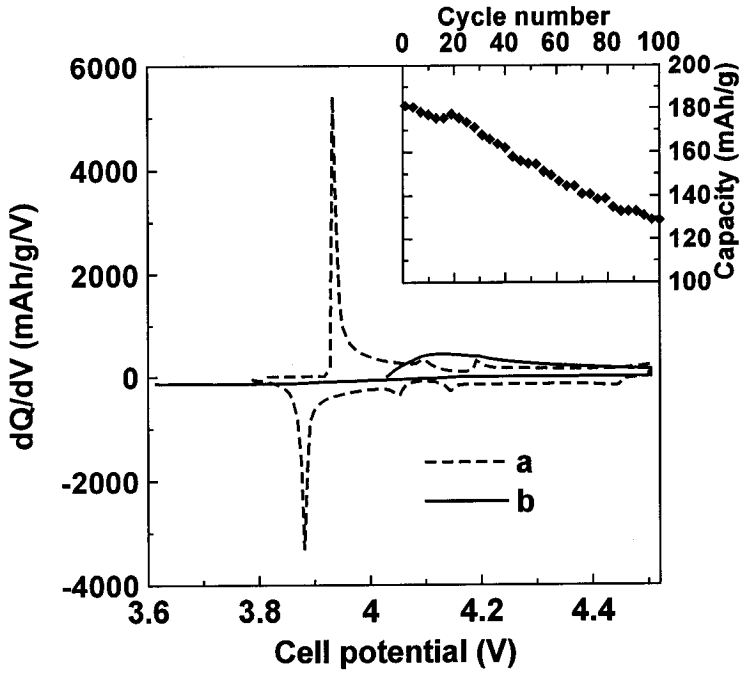

Figure 5.3 Differential capacity versus cell potential curve of FMC $LiCoO_2$ 010301 at (a) cycle 5; (b) cycle 100. The inset is the specific capacity versus cycle number. The cell was cycled at a C/3 rate between 3.6 and 4.5V for the first 18 cycles and between 3.0 and 4.5V thereafter (Chen Z. H. and Dahn J. R., 2003b).

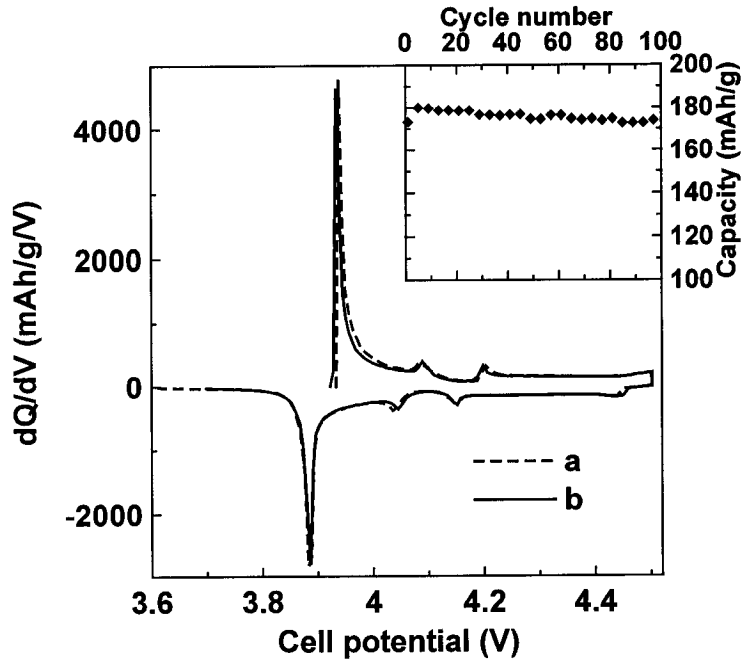

Figure 5.4 Differential capacity versus cell potential curve for sample K at (a) cycle 5 and (b) cycle 100. The inset is the specific capacity versus the cycle number of the cell.

Two key factors governing the resistive surface film formation are the surface chemistry of $LiCoO_2$ and reactivity of the electrolyte. If this is true, then changes to the surface of $LiCoO_2$ and/or changes to the electrolyte should affect the capacity loss of $LiCoO_2$ cycled to 4.5 V. Perhaps surfaces and electrolytes that suppress the formation of a high impedance film can be found and these could improve the capacity retention of $LiCoO_2$ cycled to 4.5V.

5.4 Effect of changing the surface of $LiCoO_2$

As a first trial, $LiCoO_2$ was ground by an auto-grinder to create freshly cleaved surfaces. SEM images showed that particles were broken and freshly cleaved surfaces were made after grinding. Figure 5.5 shows that the capacity retention of $LiCoO_2$ 611061 is significantly improved by just grinding. Figure 5.6 shows a similar effect of grinding on the capacity retention of $LiCoO_2$ 010301. Five other commercial $LiCoO_2$ samples listed in Table 2.1 were also ground and the same type of improvement was observed for all the ground samples.

The effect of grinding on capacity retention during cycling to 4.5V indicates that with at least some fresh $LiCoO_2$ surfaces, $LiCoO_2$ is able to be cycled to 4.5V with much better cycling behavior. This improvement indicates that some chemical species that is harmful to capacity retention may have formed on the surface of $LiCoO_2$ during storage. Since $LiCoO_2$ samples are commonly stored in air, this surface degradation may be caused by the adsorption of moisture and the resultant surface products. If this is the case, perhaps one can also remove the harmful species from the surface of $LiCoO_2$ by heating it at a certain high temperature.

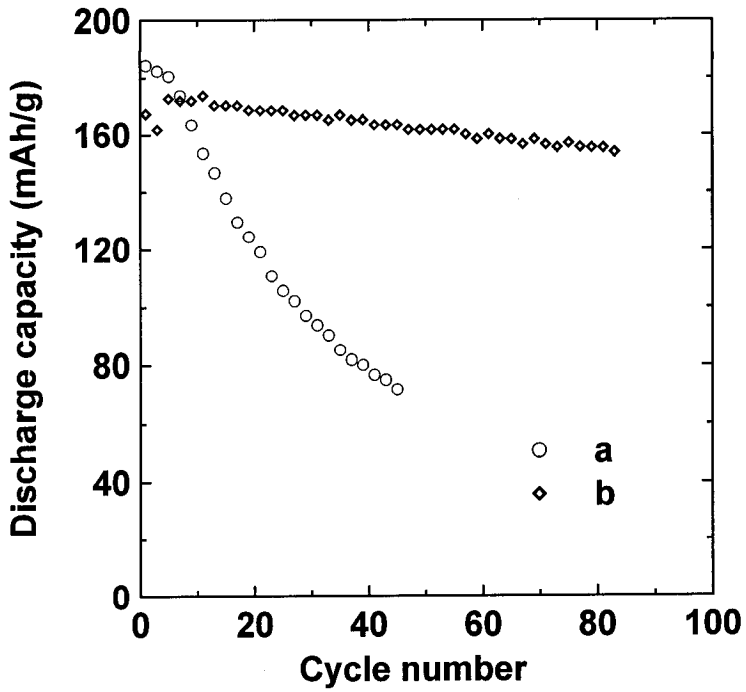

Figure 5.5 Specific capacity versus cycle number for (a) $LiCoO_2$ 611061 and (b) $LiCoO_2$ 611061 ground for 15 minutes.

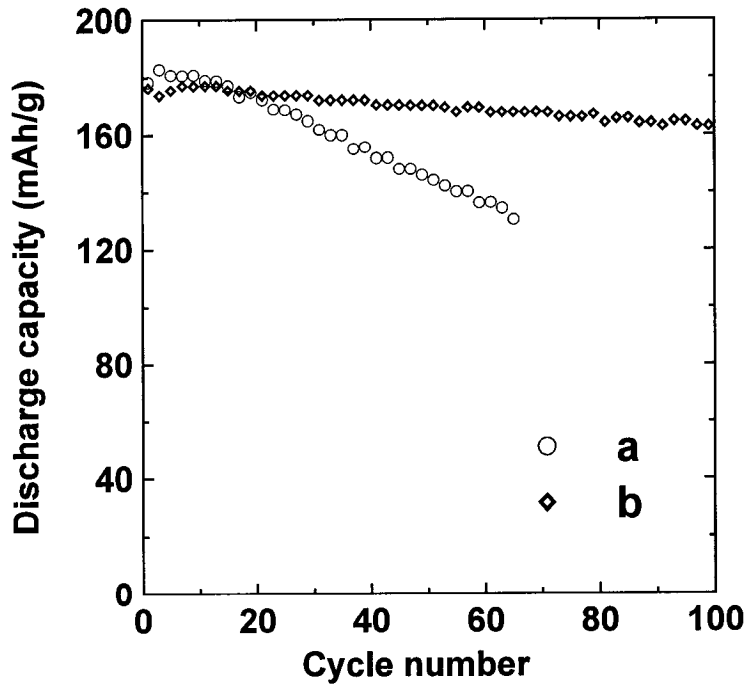

Figure 5.6 Specific capacity versus cycle number for (a) $LiCoO_2$ 010301 and (b) $LiCoO_2$ 010301 ground for 15 minutes.

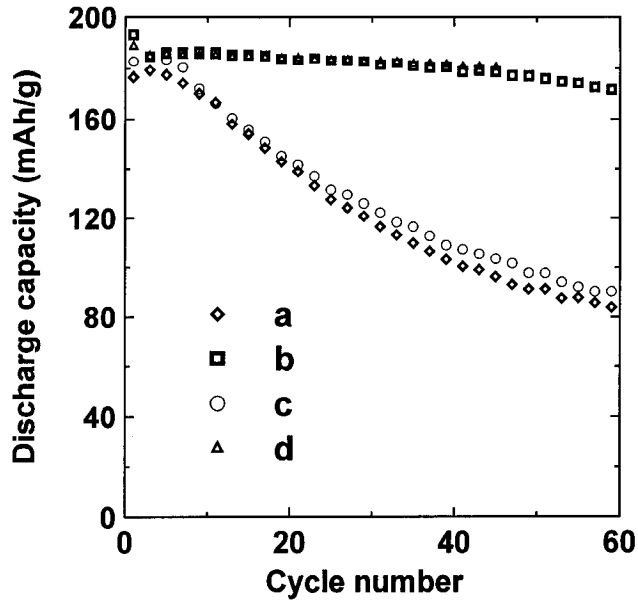

Figure 5.7 Specific capacity versus cycle number for (a) $LiCoO_2$ 00642, (b) $LiCoO_2$ 00642 heated at 550 °C, (c) $LiCoO_2$ 00642 that had been heat-treated to 550°C (like (b)) then exposed to water for one week, followed by drying at 150°C, and (d) $LiCoO_2$ 00642 that had been exposed to water (like (c)) then heated to 550 °C.

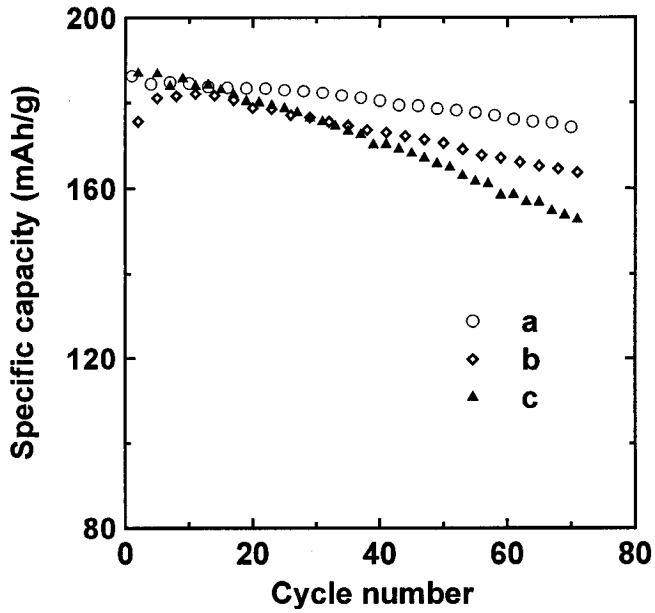

Figure 5.8 Specific capacity versus cycle number for $LiCoO_2$ 00642 heated to 800 °C for 3 hrs. The cell was made with an electrode made (a) without delay, (b) 42 hrs, and (c) 1 week after the heating. The heated powder was stored in a glass vial with the cap closed.

Figure 5.7 (curve b) shows a significantly improved capacity retention of heat-treated (550°C) FMC $LiCoO_2$ 00642 when cycled to 4.5 V. Six other commercial samples listed in Table 2.1 were heat-treated to 550°C and a similar effect was observed for all samples. In addition, heating to 800°C has essentially the same effect as heating to 550°C. As with grinding, heating $LiCoO_2$ samples creates fresh surfaces of $LiCoO_2$ that give good capacity retention when cycled to 4.5 V. The surface of untreated $LiCoO_2$ gives rise to impedance growth, and poor cycling, when cycled using the same conditions.

To show that the surface degradation of $LiCoO_2$ can be caused by moisture, a heated $LiCoO_2$ 00642 sample was subjected to severe moisture exposure by leaving the sample in water for one week. During the water exposure, some chemical species (e.g. LiOH, Li_2CO_3, Co_3O_4, spinel $LiCoO_2$, etc) may form on the surface. The sample was then dried at 150°C for 12 hours to eliminate residual water. X-ray diffraction showed no impurity peaks proving that bulk changes to the sample did not occur. The cycling behavior of this sample that had been exposed to water is shown by curve c in Figure 5.7. The sample now has almost the same poor capacity retention as the original $LiCoO_2$ 00642 sample (curve a in Figure 5.7). Curve d in Figure 5.7 shows that the poor capacity retention of the sample exposed to water was improved by heating again at 550°C. Thus, moisture exposure does apparently change the surface chemistry and cause severe damage to capacity retention for cycling to 4.5 V.

If the water exposure has such a harmful impact on capacity retention of $LiCoO_2$ cycled to 4.5 V, a period of exposure to air may also cause damage. Figure 5.8 shows the effect of the length of the period of time between heating and electrode making on

capacity retention of $LiCoO_2$ cycled to 4.5 V. Data set a in Figure 5.8 shows that with an electrode made right after the heating, $LiCoO_2$ has an excellent capacity retention. Data set b in Figure 5.8 shows that only a 42 hrs waiting time causes an apparent degradation on capacity retention of $LiCoO_2$ cycled to 4.5 V. Data set c in Figure 5.8 shows that further storage causes more degradation in capacity retention.

Since both the ground samples and the heated samples were handled in air and exposed to the air for a certain period of time (two days or longer), a slight degradation of their surface properties may have occurred. Thus their performance, although quite good, may be better if all air exposure could be eliminated. The results in Figures 5.5, 5.6, and 5.7 clearly show that structural instability is not responsible for capacity fading of $LiCoO_2$ cycled to above 4.2 V but below or equal to 4.5 V.

Gao *et al.* (2002) claim that the poor cycling behavior of $LiCoO_2$ is partially caused by localized cubic spinel-like structural phases that can be eliminated by quenching $LiCoO_2$ from high temperature. They showed that $LiCoO_2$ that had been cooled quickly had better capacity retention than $LiCoO_2$ that was slow-cooled. However, in experiments here, such an effect was not observed. Figure 5.9 shows that the FMC $LiCoO_2$ 00642 samples cooled at very different rates have almost the same capacity retention, which is much better than that before heating (Figure 5.7a).

During the oxide coating process, $LiCoO_2$ is heated to about 600°C or 550°C in chapter 4. Figures 5.7, 5.8, and 5.9 show that just by heating, the capacity retention of $LiCoO_2$ cycled to 4.5 V is improved significantly. Since all metal oxide coating recipes published in the literature involve a heat-treatment step, it is probably the heat-treatment, not the presence of the metal oxide, that is most important.

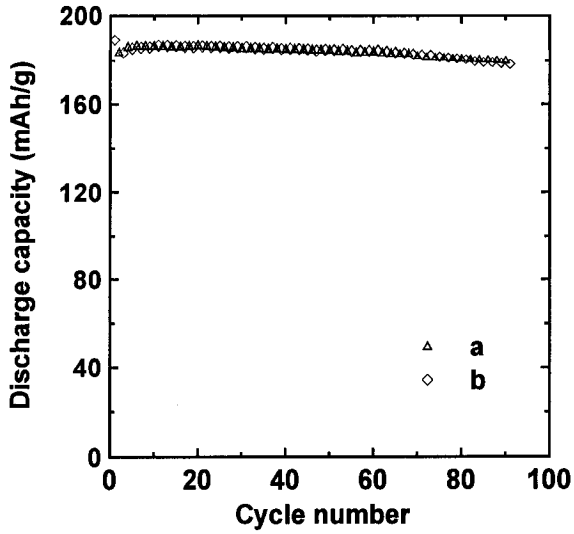

Figure 5.9 Specific capacity versus cycle number for $LiCoO_2$ 00642 heated to 950℃ and then (a) slow cooled by turning off the furnace and (b) cooled rapidly by removing the sample directly from the furnace (Chen Z. H. and Dahn J. R., 2003b).

5.5 Effect of changing the salt in the electrolyte

Changing the electrolyte may be another way to suppress the impedance growth on the surface of $LiCoO_2$ during cycling to 4.5V. It has been reported that moisture-related species are harmful to $LiPF_6$-based electrolytes (Aurbach *et al.*, 2002). $LiPF_6$-based electrolytes were used in the experiments reported here and in all cycle life tests on coated $LiCoO_2$ samples performed by other researchers. LiBOB is a newly introduced salt for Li ion batteries (Xu W. *et al.*, 2001; Xu K. *et al.*, 2001). According to experiments with LiBOB-based electrolyte, the capacity retention is indeed much better, while the polarization is larger than with $LiPF_6$-based electrolyte. Figure 5.10 shows that $LiCoO_2$ 010301 has a better capacity retention in a LiBOB electrolyte than in a $LiPF_6$ electrolyte. Figure 5.11 shows that heat-treated (800°C) $LiCoO_2$ 00643 has excellent capacity retention with a capacity about of 170 mAh/g when cycled to 4.5 V using LiBOB-based electrolyte.

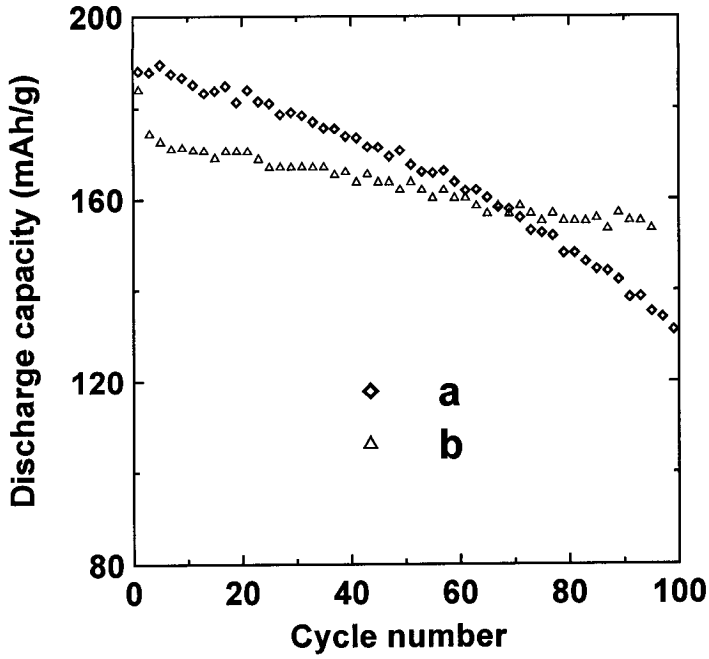

Figure 5.10 Specific capacity versus cycle number for $LiCoO_2$ 010301 tested in (a) 1 M $LiPF_6$ and (b) 0.7 M LiBOB in EC/DEC (1:2 v/v).

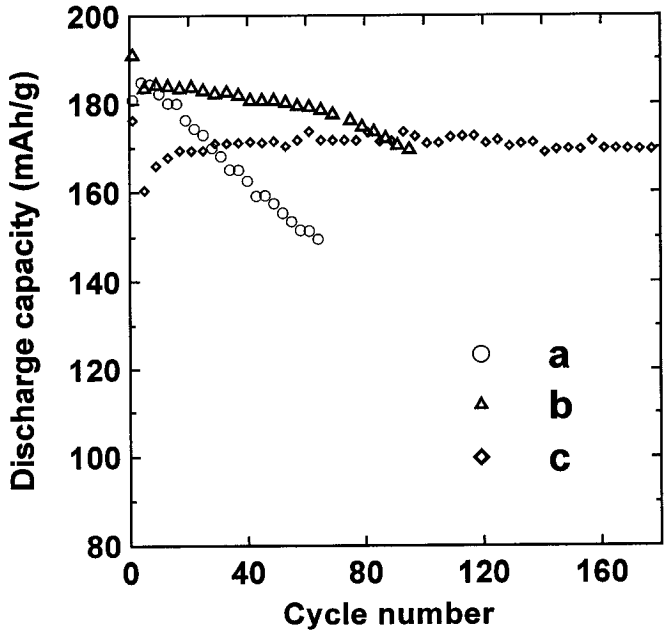

Figure 5.11 Specific capacity versus cycle number for (a) $LiCoO_2$ 00643 tested in 1 M $LiPF_6$ in EC/DEC (1:2 v/v), (b) $LiCoO_2$ 00643 heated at 800℃ then tested in 1 M $LiPF_6$ in EC/DEC (1:2 v/v), and (c) $LiCoO_2$ 00643 heated at 800℃ then tested in 0.7 M LiBOB in EC/DEC (1:2 v/v).

5.6 Summary

The poor capacity retention of $LiCoO_2$ cycled above 4.2 V (but below or equal to 4.5V) is caused by side reactions that cause the growth of a high impedance layer on the surface of the $LiCoO_2$ rather than by structural instability. The side reactions appear to involve moisture-related chemical species on the $LiCoO_2$ surface and $LiPF_6$-based electrolyte. By removing the harmful chemical species or using LiBOB-based electrolyte, significant improvement in the capacity retention of $LiCoO_2$ cycled to 4.5V was observed.

After a heat treatment to 550°C, the poor capacity retention of $LiCoO_2$ becomes better. After an exposure to water followed by drying at 150 °C, the capacity retention of previously heated $LiCoO_2$ becomes poor. Whatever surface species formed during the water exposure can apparently be eliminated by a subsequent heat treatment to 550°C, suggesting that they could be species like Li_2CO_3, LiOH, Co_3O_4 or spinel $LiCoO_2$. Surface science experiments, such as XPS, are required to determine the composition of such surface species.

Chapter 6 SiO_2 addition to $LiPF_6$-based electrolyte

6.1 Introduction

Chapter 5 has demonstrated that the heating process used when coating $LiCoO_2$ with oxides has a major effect on improving the capacity retention of $LiCoO_2$ cycled to 4.5 V. In a $LiCoO_2$ sample coated with oxide, there is usually 1 wt% oxide or more that is most likely located on the surface of $LiCoO_2$. This oxide on the surface of $LiCoO_2$ may also interfere with the side reactions that cause impedance growth and capacity fading during cycling to 4.5 V. To investigate the effect of the oxide coating on its capacity retention, $LiCoO_2$ was cycled to 4.5 V in 1 M $LiPF_6$ in EC/DEC (1:2 v/v) with fumed oxide (SiO_2 or Al_2O_3) added directly to the electrolyte. Surprisingly, SiO_2 addition results in a significant improvement in capacity retention of $LiCoO_2$ but Al_2O_3 addition has no effect. This chapter shows the effect of SiO_2 addition to the electrolyte on the capacity retention of $LiCoO_2$ in both Li metal cells and Li-ion cells.

6.2 Effect of SiO_2 addition on capacity retention of $LiCoO_2$ in Li metal cells

In order to obtain an intimate mixture of oxide powder and electrolyte, an oxide with a very fine particle size is needed. Therefore, fumed SiO_2 and Al_2O_3 were used. Figure 6.1 shows that the average particle size of the fumed SiO_2 is about 20-30 nm. Figure 4.12b shows that this fumed SiO_2 is amorphous. To investigate the effect of SiO_2 addition on the capacity retention of $LiCoO_2$, different amounts of SiO_2 were mixed with 1 M $LiPF_6$ in EC/DEC (1:2 v/v). Cells were made immediately after the mixing. Figure 6.2 shows specific capacity versus cycle number for $LiCoO_2$ 00640 cycled to 4.5 V in a

$LiPF_6$-based electrolyte with 5 different concentrations of added SiO_2. There is a steady improvement in performance as the concentration of fumed SiO_2 is increased from 0 to 2% by weight. Concentrations above about 2% by weight give no additional improvement.

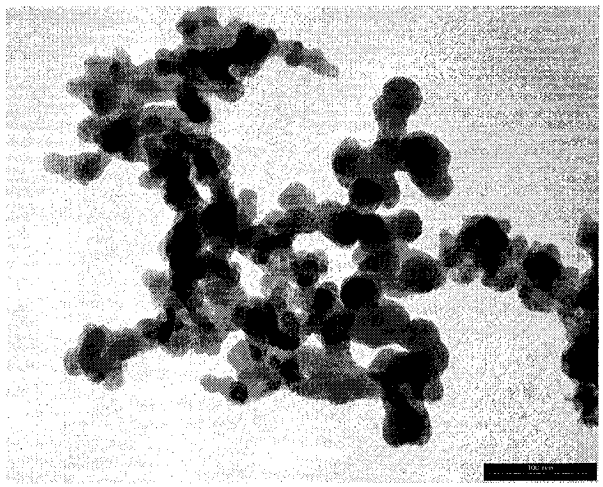

Figure 6.1 A TEM image of fumed SiO_2.

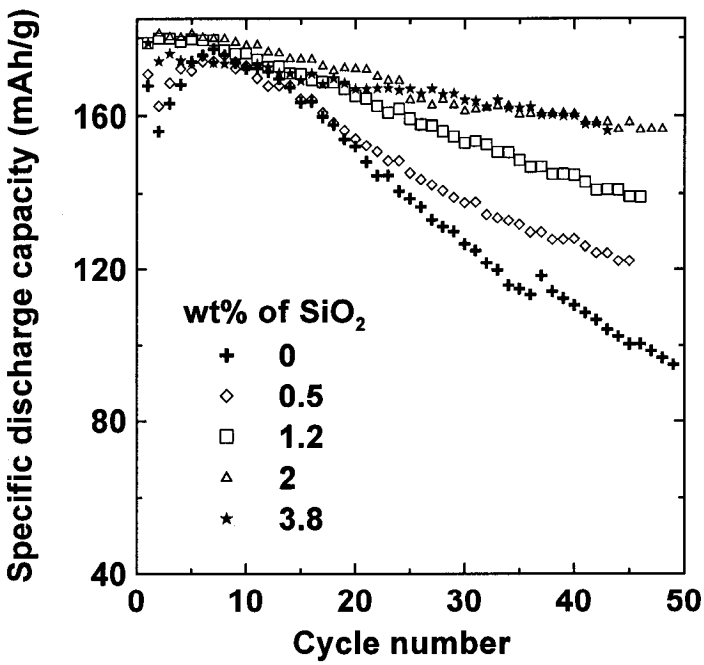

Figure 6.2 Specific discharge capacity versus cycle number for $LiCoO_2$ 00640 cycled to 4.5 V in 1 M $LiPF_6$ in EC/DEC (1:2 v/v) with different amounts of fumed SiO_2 added to the electrolyte.

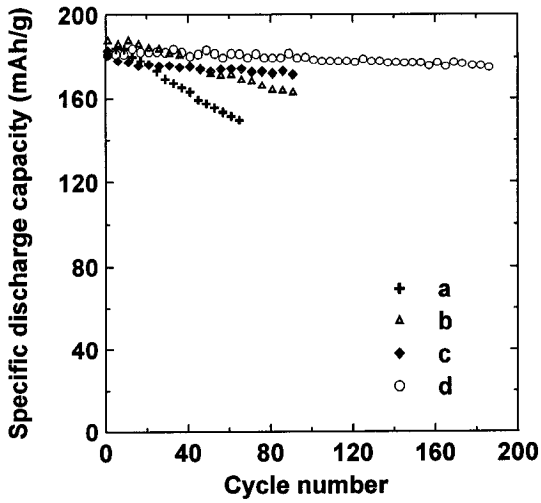

Figure 6.3 Specific discharge capacity versus cycle number for $LiCoO_2$ 00643 (a) cycled to 4.5V in 1 M $LiPF_6$ in EC/DEC (1:2 v/v), (b) cycled to 4.5 V in 1 M $LiPF_6$ in EC/DEC (1:2 v/v) with 2 wt% fumed SiO_2 added in the electrolyte, (c) cycled to 4.45 V in the same electrolyte as (b), and (d) $LiCoO_2$ 00643 heated to 800°C cycled to 4.5 V in the same electrolyte as (b).

For all seven $LiCoO_2$ samples listed in Table 2.1, a significant improvement in capacity retention was observed for cycling to 4.5 V when 2 wt% SiO_2 was added to the electrolyte. For example, data set b in Figure 6.3 shows that, when cycled to 4.5 V, $LiCoO_2$ 00643 has better cycling behavior with SiO_2 addition than without SiO_2 addition. Data set c in Figure 6.3 shows that even better capacity retention is obtained by lowering the upper cutoff potential to 4.45 V.

Chapter 5 has proved that a heat treatment can improve the capacity retention of $LiCoO_2$. The impact of a combination of both treatments was investigated. Data set d in Figure 6.3 shows the capacity versus cycle number of sample 00643 heated to 800°C and with 2 wt% SiO_2 added to the electrolyte. With both heat treatment and SiO_2 addition in the electrolyte, excellent capacity retention was obtained. $LiCoO_2$ 00643 delivers a capacity about 180 mAh/g with only about 3 % capacity fading over the first 180 cycles.

This improved capacity retention is about the same as that for $LiCoO_2$ 010301 coated with Al_2O_3 (sample J in chapter 4).

It was observed that some gases evolve from the mixture of the electrolyte and fumed SiO_2. The gas release lasts for 3 or 4 days. Simultaneously, the fumed SiO_2 is consumed so that the mixture becomes a clear liquid. This indicates that chemical reactions involving SiO_2 and the electrolyte occur after the SiO_2 is added to the electrolyte. Chapter 5 has demonstrated that capacity fading of $LiCoO_2$ cycled to 4.5 V is caused by side reactions involving moisture-related chemical species on the $LiCoO_2$ surface and $LiPF_6$-based electrolyte. The improvement in the capacity retention of $LiCoO_2$ caused by SiO_2 addition may be due to reactions consuming the harmful species in the electrolyte or cleaning the surface of $LiCoO_2$.

6.3 Effect of SiO_2 addition on the capacity of $LiCoO_2$ in Li-ion cells

Since the ultimate goal of this study is to improve the energy density of Li-ion batteries, the capacity retention of $LiCoO_2$ was also tested in Li-ion cells with fumed SiO_2 added to 1 M $LiPF_6$ in EC/DEC (1:2 v/v). Figure 6.4 shows both charge and discharge capacities versus cycle number for $LiCoO_2$ 00643 in a Li-ion cell using an electrolyte without SiO_2. Figure 6.5 shows both charge and discharge capacities versus cycle number for $LiCoO_2$ 00643 in a Li-ion cell using an electrolyte with 2 wt% SiO_2 addition. In contrast with the significant improvement by SiO_2 addition in Li metal cells, there is no apparent effect of SiO_2 addition on capacity retention of $LiCoO_2$ in the Li-ion cell. Furthermore, specific irreversible capacity for the first cycle of the cell is much larger (about 60 mAh/g) than that for the same cell without SiO_2 (about 25 mAh/g).

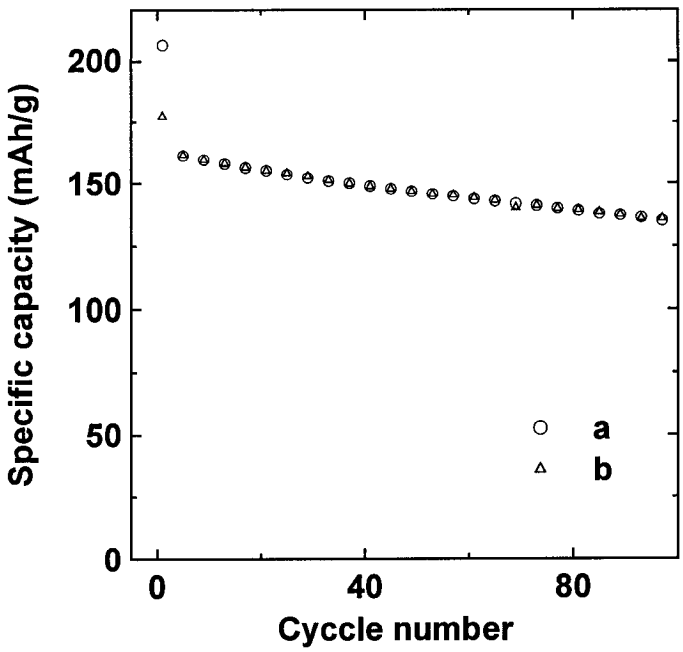

Figure 6.4 Specific (a) charge capacity and (b) discharge capacity versus cycle number for $LiCoO_2$ 00643 cycled to 4.4 V with respect to an MCMB electrode in 1 M $LiPF_6$ in EC/DEC (1:2 v/v). The charge/discharge cycle was started immediately after the cell was made.

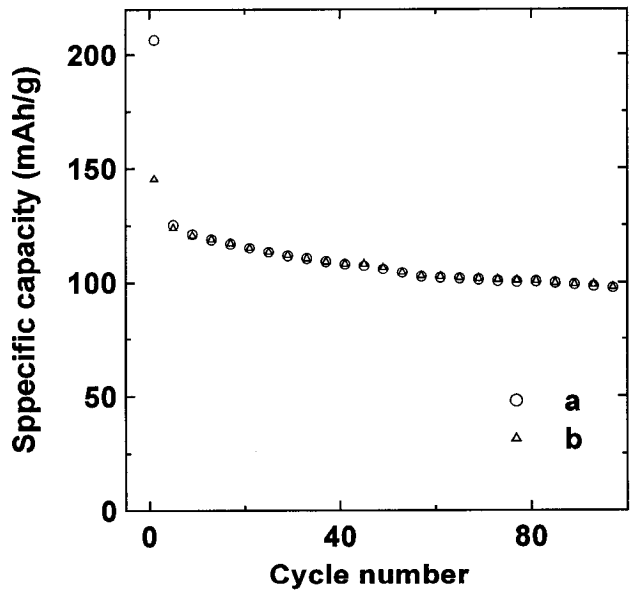

Figure 6.5 Specific (a) charge capacity and (b) discharge capacity versus cycle number for $LiCoO_2$ 00643 cycled to 4.4 V with respect to an MCMB electrode in 1 M $LiPF_6$ in EC/DEC (1:2 v/v) with 2 wt% fumed SiO_2 added to the electrolyte. The charge/discharge cycle was started immediately after the cell was made.

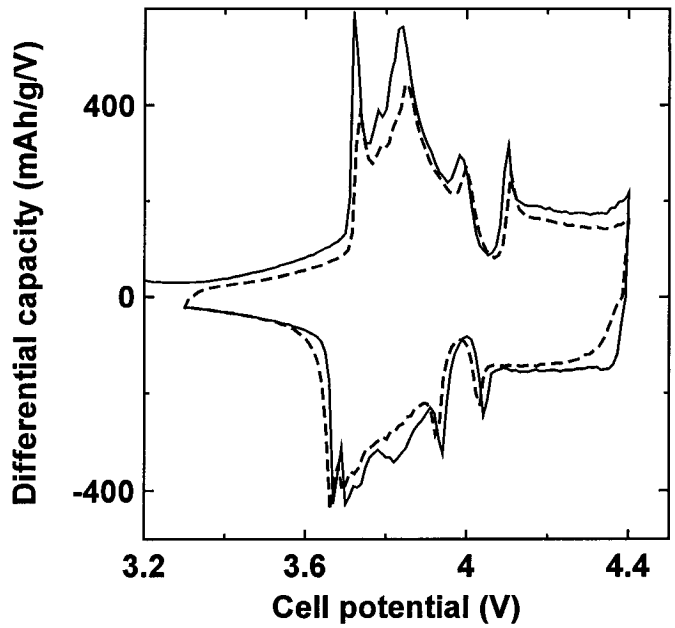

Figure 6.6 Differential capacity versus cell potential curves for the first two cycles of the same cell as in Figure 6.4. The solid line and the dashed line represent the first and second cycles, respectively.

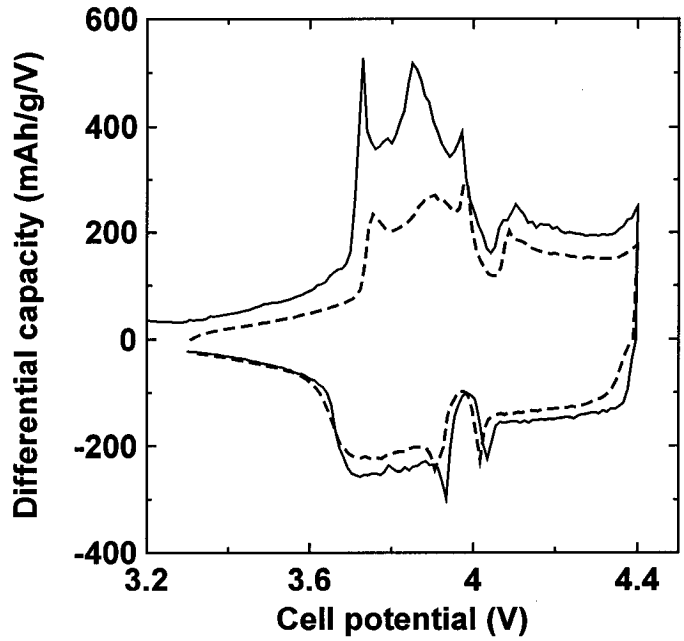

Figure 6.7 Differential capacity versus cell potential curves for the first two cycles of the same cell as in Figure 6.5. The solid line and the dashed line represent the first and second cycles, respectively.

Figures 6.6 and 6.7 show differential capacity versus cell potential curves for the first two cycles of the same cells in Figures 6.4 and 6.5, respectively. In Figure 6.6, there are four major peaks in the first charge curve. The two peaks at about 3.8 V correspond to the phase transition between the two O3 phases of Li_xCoO_2. The other two peaks at about 4 V correspond to the order/disorder phase transitions of Li_xCoO_2. The first discharge curve shows peaks corresponding to three reverse phase transitions as Li is reinserted into Li_xCoO_2. However, the two peaks corresponding to the O3/O3 phase transition have lower intensity than the two peaks at the same potential range in the first charge curve. This lower intensity is caused by loss of active Li atoms to the irreversible capacity of both electrodes. Because of the loss of Li atom and a larger specific current used (47 mA/g was used for the second cycle, 14 mA/g was used for the first cycle), the intensity of the second charge curve is slightly lower that of the first charge curve.

With 2 wt% SiO_2 addition in the electrolyte, the evolution of the differential capacity versus potential curve is much different. In Figure 6.7, the first charge curve, with four peaks, is similar to the first charge curve in Figure 6.6. However, in the first discharge curve in Figure 6.7, the two peaks corresponding to the O3/O3 phase transition becomes a flat plateau with lower intensity than the corresponding peaks in Figure 6.6. This indicates that more Li atoms were consumed chemically besides those lost as irreversible capacity of the electrodes. Therefore, SiO_2 addition causes a larger specific irreversible capacity in the first cycle in a Li-ion cell. Consequently, for the following cycles, the specific capacity of $LiCoO_2$ in a Li-ion cell with SiO_2 addition is lower than that in a cell without SiO_2, as shown in Figures 6.4 and 6.5. Figure 6.7 shows that the second charge curve has much lower intensity than the first charge curve.

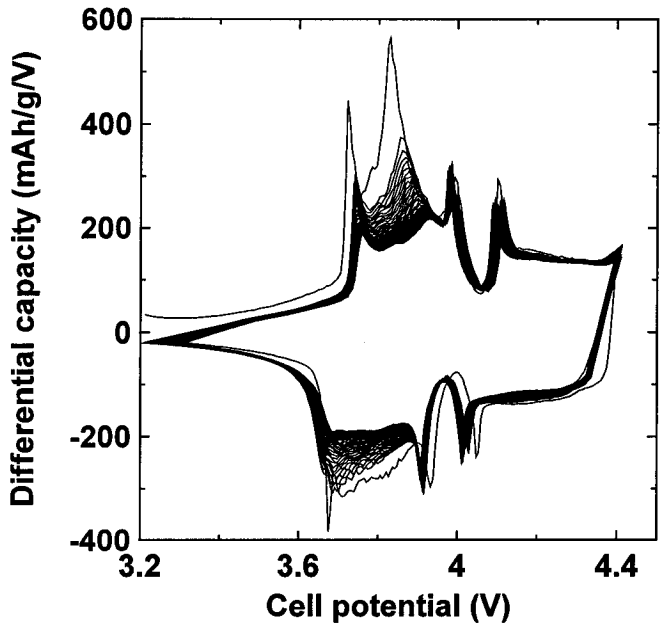

Figure 6.8 Differential capacity versus cell potential for a cell made with a $LiCoO_2$ 00642 positive electrode and an MCMB negative electrode cycled to 4.4 V in 1 M $LiPF_6$ in EC/DEC (1:2 v/v) with 0.5 wt% fumed SiO_2 added to the electrolyte. The charge/discharge cycle was started immediately after the cell was made.

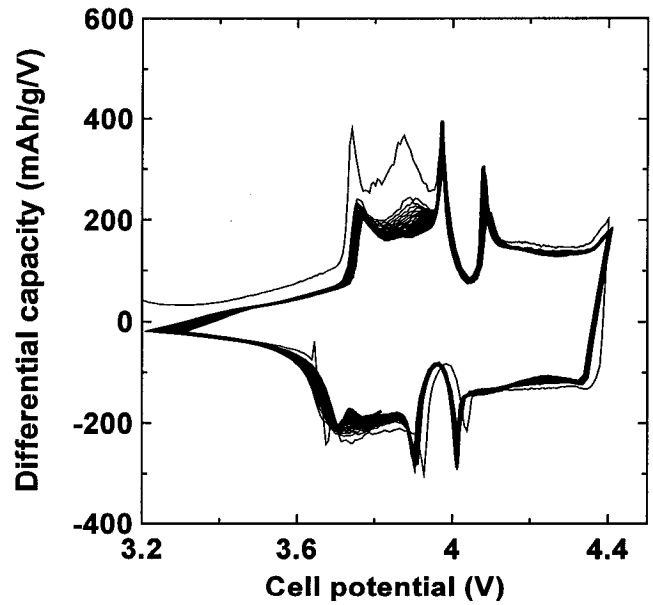

Figure 6.9 Differential capacity versus cell potential for a cell made with a $LiCoO_2$ 00642 positive electrode and an MCMB negative electrode cycled to 4.4 V in 1 M $LiPF_6$ in EC/DEC (1:2 v/v) with 0.5 wt% fumed SiO_2 added to the electrolyte. The charge/discharge cycle was started 2 days after the cell was made.

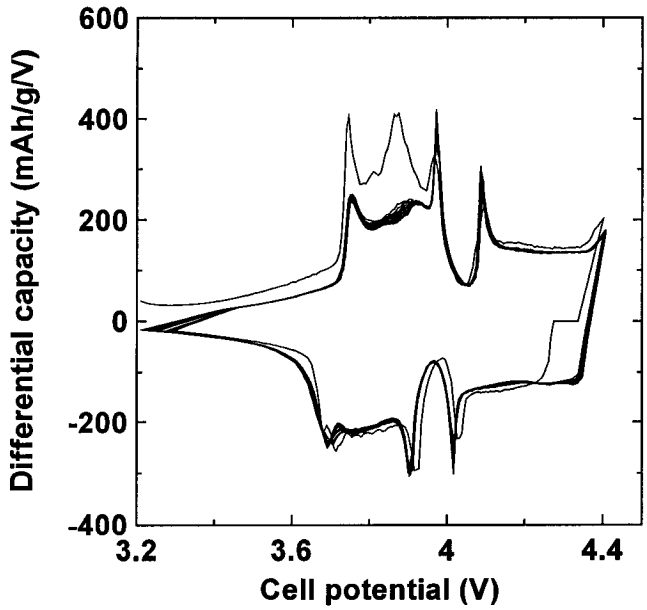

Figure 6.10 Differential capacity versus cell potential for a cell made with a $LiCoO_2$ 00642 positive electrode and an MCMB negative electrode cycled to 4.4 V in 1 M $LiPF_6$ in EC/DEC (1:2 v/v) with 0.5 wt% fumed SiO_2 added to the electrolyte. The charge/discharge cycle was started 4 days after the cell was made.

Figure 6.8 shows the differential capacity versus cell potential curve for a Li-ion cell made with $LiCoO_2$ 00642 with 0.5 wt% SiO_2 in the electrolyte. The difference between the charge curves for the first two cycles is much smaller than that in Figure 6.7. Therefore, with a lower SiO_2 concentration in the electrolyte, fewer Li atoms are consumed chemically in the first cycles. However, in the following cycles, the charge curve drops with a decreasing rate, which means that more Li atoms are gradually consumed during the following cycles.

Two more cells were made with the same materials and the same conditions as the one whose data are shown in Figure 6.8. However, the charge/discharge cycling for these two cells were started 2 and 4 days after they had been made, respectively, instead of immediately as for the cell in Figure 6.8. Figures 6.9 and 6.10 show the differential

capacity versus potential curves for the cells, respectively. According to Figures 6.9 and 6.10, for the cell that has rested for a longer period of time before starting the charge/discharge cycle, the two peaks at about 3.8 V in the second charge curve are lower. This indicates that Li is consumed more rapidly during the first cycle for this cell. Since reactions between the electrolyte and SiO_2 occur after they are mixed together regardless of whether the charge/discharge cycle has been started, longer resting time results in higher concentration of the products from the reactions. Thus the Li consumption is probably caused by some other reactions involving the products from the reaction between the electrolyte and SiO_2.

It is not clear what are the reactions between SiO_2 and the electrolyte and what are the reactions consuming Li atoms chemically in Li-ion cells with SiO_2 added to the electrolyte. The following reactions are speculated:

$$LiPF_6 \longrightarrow LiF + PF_5 \quad (3)$$

$$PF_5 + H_2O \longrightarrow 2HF + PF_3O \quad (4)$$

$$SiO_2 + 4HF \longrightarrow SiF_4\,(gas) + 2H_2O \quad (5)$$

$$SiF_4 + 4Li \longrightarrow 4LiF + Si \quad (6)$$

Since fumed SiO_2 has an extremely large surface area, there is possibly moisture absorbed on it even though it was heated to 200 °C in a furnace before mixing it with the electrolyte. A small amount of moisture can result in HF in the electrolyte by reactions such as in Equations (3) and (4). HF consumes SiO_2 and produces SiF_4 gas (Equation (5)). As a gas, SiF_4 can diffuse well in the cell and may react with Li in the graphite (the negative electrode), subsequently causing a large irreversible capacity in the Li-ion cell.

If Li atoms are chemically consumed by reactions such as Equations (3-6), the Li consumption stops once the SiO_2 is completely consumed. For the three cells, 0.5 wt% SiO_2 was added to the electrolyte. About 60 mg electrolyte and 8 mg $LiCoO_2$ were used for each cell. With such a ratio, the chemical Li consumption caused by the reactions results in about 60 mAh/g capacity loss for $LiCoO_2$. According to Figures 6.8, 6.9, and 6.10, no matter how fast Li is chemically consumed during the first cycle, the decreasing charge curve stops at about the same level. This experimental data supports the proposed reactions.

For a Li-ion cell with Al_2O_3 addition in $LiPF_6$-based electrolyte, there may be reactions that are similar to those shown in Equations (3-5). Since AlF_3 is a solid, there is no gas evolution in the mixture of Al_2O_3 and the electrolyte. Since AlF_3 is not as mobile as SiF_4 gas, the reaction between AlF_4 and Li in the negative electrode (graphite) could be much slower than that between SiF_4 and Li. This is probably the reason why there is no apparent irreversible capacity caused by chemical consumption of Li observed in a Li-ion cell with Al_2O_3 addition.

6.4 Delithiation of $LiCoO_2$ in the mixture of $LiPF_6$-based electrolyte and SiO_2

To confirm the chemical Li consumption by the mixture of the electrolyte and fumed SiO_2, 2 g of $LiCoO_2$ 00642 was put into a 10 ml mixture of $LiPF_6$-based electrolyte and fumed SiO_2 (3 wt% SiO_2) and stored for 3 weeks. During the storage, the color of the liquid turns pink and then becomes colorless again. In the mean time, there is a precipitation of some pink particles. After 3 weeks, solid was separated from the liquid and washed with DMC. Figure 6.11 shows the XRD pattern for the washed solid. In this

pattern, there are peaks from Li_2SiF_6. Li_2SiF_6 is possibly resulted from the following reaction.

$$2LiPF_6 + SiO_2 \rightarrow 2POF_3 + Li_2SiF_6 \qquad (7)$$

However, the splitting of the (003) peak of $LiCoO_2$ in the XRD pattern indicates delithiation of $LiCoO_2$, which cannot be explained by equation (7). Figure 6.12 more clearly shows that the (003) peak has split into three peaks. The one to the right is the original (003) peak from $LiCoO_2$. The two peaks at lower angle correspond to two phases of $Li_{1-x}CoO_2$ that have less Li. As shown by Reimers and Dahn (1992), as Li starts to be removed from $LiCoO_2$, the lattice constant c increases and the (003) peak shifts to a lower angle. Such a chemical delithiation causes irreversible capacity in a Li-ion cell but not in a Li metal cell where excess Li exists in the negative electrode.

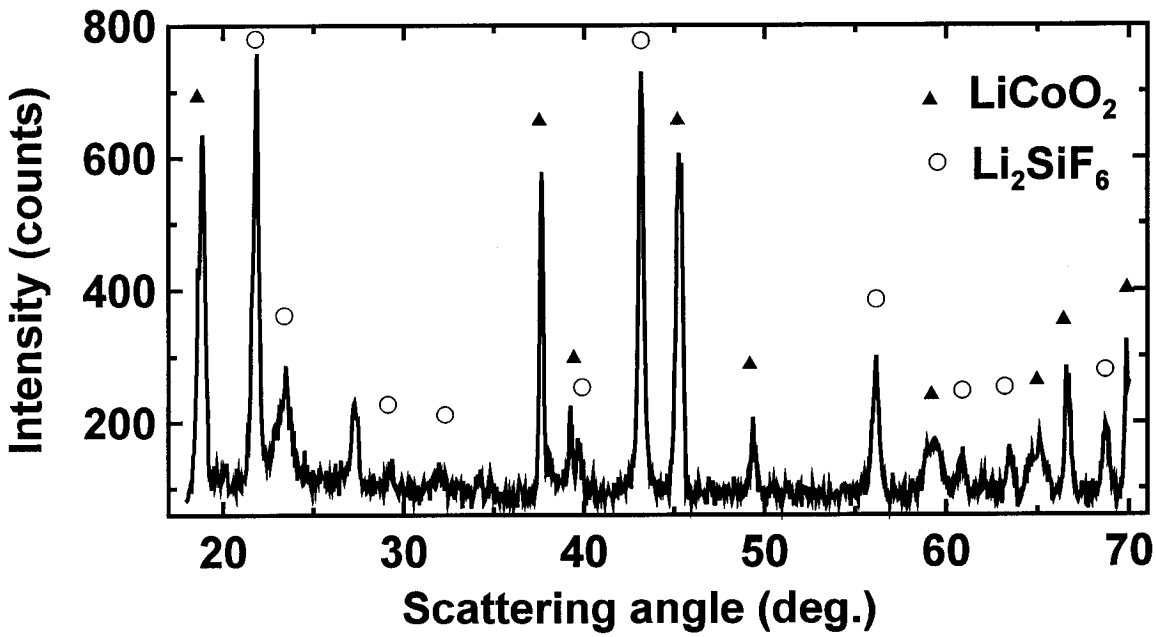

Figure 6.11 XRD pattern of the solid separated from an electrolyte with $LiCoO_2$ 00642 added and 3 wt% (with respect to the weight of the electrolyte) fumed SiO_2 added and left for 3 weeks. The electrolyte was 1 M $LiPF_6$ in EC/DEC (1:2 v/v). The solid was washed with DMC to remove $LiPF_6$.

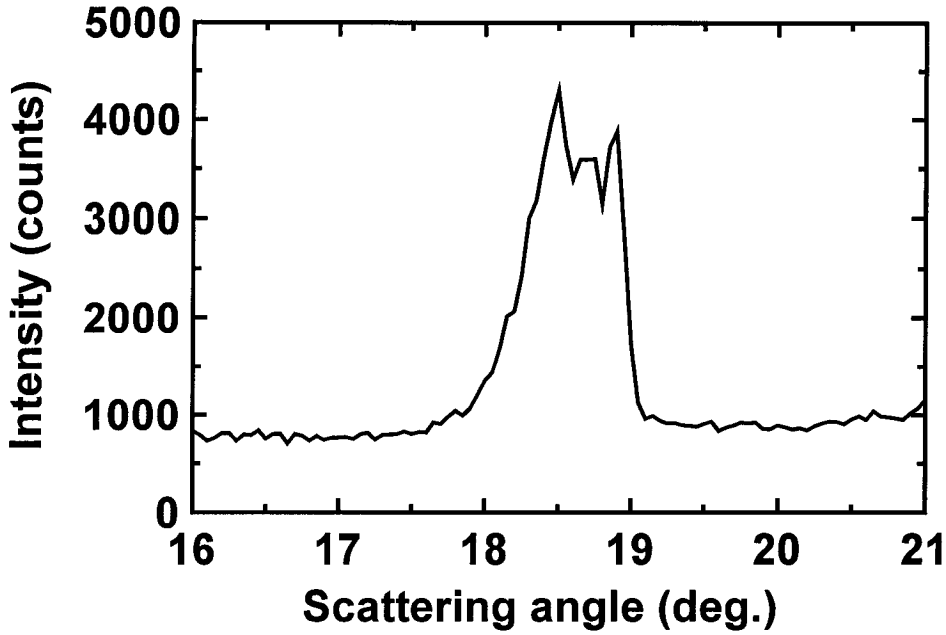

Figure 6.12 Part of the XRD pattern shown in Figure 5.10 in the scattering angle range between 16 to 21 degrees.

6.5 Summary

Addition of SiO_2 to the electrolyte significantly improves the capacity retention of $LiCoO_2$ in Li metal cells. However, it causes a larger irreversible capacity in Li-ion cells because some products from the reaction between the electrolyte and SiO_2 consume Li in $LiCoO_2$. Addition of Al_2O_3 in $LiPF_6$-based electrolyte has no apparent effect on the capacity retention of $LiCoO_2$ cycled to 4.5 V.

Chapter 7 Staging phase transitions in Li_xCoO_2

7.1 Introduction

Chapter 5 has shown that side reactions involving the surface of $LiCoO_2$ and $LiPF_6$-based electrolyte are responsible for the poor capacity retention of $LiCoO_2$ cycled to 4.5 V. When the harmful side reactions on the surface of $LiCoO_2$ are suppressed, $LiCoO_2$ can deliver a capacity of 180 mAh/g to 4.5 V with excellent capacity retention. To achieve even higher capacity, $Li_{1-x}CoO_2$ has to be charged to a potential higher than 4.5 V with respect to Li metal. However, a good capacity retention cannot be maintained when $LiCoO_2$ is cycled to a potential of 4.6 V or higher. For example, Figure 4.10 shows that the capacity retention of coated $LiCoO_2$ is poor when cycled with an upper cutoff 4.6 V or 4.7 V. In order to understand the reasons for the poor capacity retention of $LiCoO_2$ cycled above 4.5 V, the electrochemical behavior and structural changes of Li_xCoO_2 in the potential region above 4.5 V will be investigated in this chapter.

The electrochemical behavior and structural changes of $LiCoO_2$ in the potential region above 4.5 V have been investigated by other researchers. First, Ohzuku and Ueda (1994) performed *ex-situ* X-ray Diffraction (XRD) studies on $LiCoO_2$ electrodes that were charged to various potentials up to 4.8 V. After more than 0.75 Li was extracted from $LiCoO_2$, a new phase that formed from the O3 phase was observed. However, even when charged to 4.8 V, the O3 phase had not completely transformed to the new phase. In the XRD pattern of the purest new phase obtained, there were still some peaks from the O3 phase, such as the (003) and (104) peaks. All the peaks in this pattern were

indexed based on a monoclinic phase except for two peaks: the (003) peak from the O3 structure and a peak from polyethylene.

Using dry plastic Li-ion battery technology, Amatucci *et al.* (1996) performed an *in-situ* XRD study on a $LiCoO_2$ electrode charged to 5.2 V and then discharged to 3.0 V. They also observed the formation of the new phase after more than 0.75 Li was removed, and followed Ohzuku's indexing of the powder pattern. In addition, they observed another phase transition at higher potentials. They observed, for the first time, that Li_xCoO_2 converted to CoO_2, with an O1 structure, after charging to 5.2 V.

After the above experimental results were reported, Van der Ven and Ceder (1998a and 1998b) calculated the phase diagram of Li_xCoO_2 from first-principles. For $0.0 < x < 0.5$ in Li_xCoO_2, they predicted two new phases other than the O3 phase. The phase containing no lithium, at $x = 0.0$, is the O1 phase. This result agrees with the experiments of Amatucci *et al.* (1996). Van der Ven and Ceder also predicted that a *stage-2* compound, which they called "H1-3", would be the most stable phase in the range $0.12 < x < 0.19$. Their calculated XRD pattern of the *stage-2* phase agrees qualitatively with experimental XRD patterns for the same phase reported by Ohzuku's group and by Amatucci *et al.* (1996).

More recently, Sun *et al.* (2001) performed an *in-situ* XRD study on $LixCoO_2$ during a charge up to 5.2 V. From XRD patterns, they observed two phase transitions in the region between $0.0 < x < 0.28$. They agreed that the final phase with x=0 is the O1 phase. However, they did not think that the phase that appears near $x = 0.14$ is a monoclinic phase. They did not work out the structure of this phase and only called it

O1a. It is not possible to describe the diffraction pattern of this phase accurately using the Miller indices that they had assigned to the diffraction peaks.

To summarize the above experimental and theoretical work, removing Li from $Li_{0.5}CoO_2$ causes the structure of Li_xCoO_2 to change from the O3 phase to a new phase, and then from this phase to the O1 phase. To better understand the cycling of Li_xCoO_2 in the region of $0.0 < x < 0.5$, some questions still need to be answered. First, the two phase transitions were observed structurally with X-ray diffraction during the charge. However, only a single plateau was observed in this region in the voltage-composition curves presented by Amatucci *et al.* (1996). This leads one to ask if it is possible to observe both phase transitions electrochemically. Second, to use more Li per $LiCoO_2$ in a commercial cell, one hopes that these structural changes of Li_xCoO_2 are reversible. Are these two phase transitions reversible? Third, there are different opinions about the structure of the phase with $x \approx 0.14$. No profile refinement has been done to date on the XRD pattern of this phase yet. For convenience, this phase is called "X-phase" temporarily. What is the structure of X-phase?

Chapter 4 showed that $LiCoO_2$ coated with Al_2O_3 can be cycled repeatedly to 4.5 V with little capacity loss in the first 100 cycles. Therefore, Al_2O_3-coated $LiCoO_2$ may enable more careful studies of the structural and electrochemical changes of Li_xCoO_2 in the region $0.0 < x < 0.5$. To answer the three questions posed above, an *in-situ* XRD experiment was carried out on an Al_2O_3-coated $LiCoO_2$ electrode during charge and discharge in the region $0.0 < x < 0.25$ in Li_xCoO_2. An *ex-situ* XRD pattern of the X-phase was also obtained and a Rietveld refinement was performed on this pattern to determine the structure of X-phase.

7.2 Capacity fading of a coated $LiCoO_2$ sample cycled to 4.6 V

Figure 7.1 shows the capacity retention of $LiCoO_2$ 010301 and sample E ($LiCoO_2$ 010301 coated with ZrO_2) when cycled to 4.6 V in 1 M $LiPF_6$ in EC/DEC (1:2 v/v). With such a high upper cutoff potential, un-coated $LiCoO_2$ has an initial discharge capacity of 220 mAh/g. Curve a in Figure 7.1 shows that the capacity fades rapidly with cycling. Curve b in Figure 7.1 shows that the coating improves the capacity retention significantly. However, the improved capacity retention is much worse than that for the same material cycled to 4.5V.

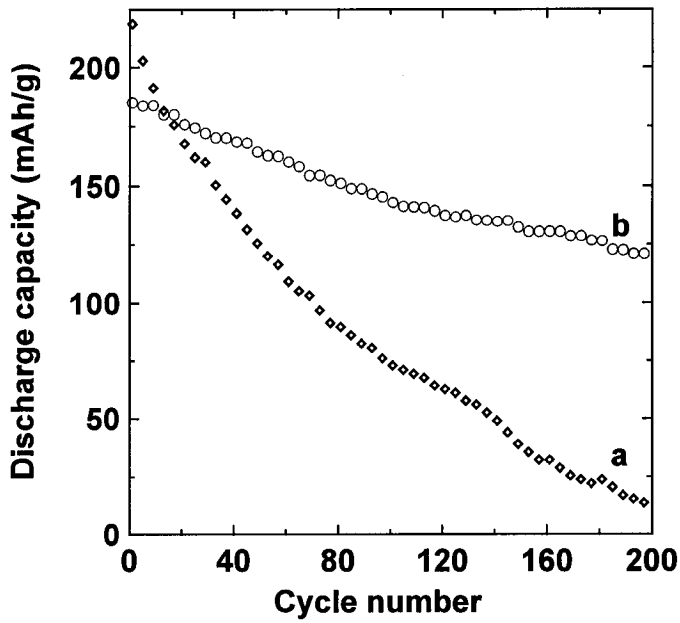

Figure 7.1 Specific capacity versus cycle number for (a) $LiCoO_2$ 010301 and (b) sample E in 1 M $LiPF_6$ in EC/DEC (1:2 v/v) cycled between 3.6 V and 4.6 V.

By studying the evolution of the differential capacity versus cell potential curves for both cells, one can understand the reasons for the capacity fading of both materials. Figure 7.2 shows the differential capacity versus cell potential curves of un-coated $LiCoO_2$ 010301 for four different cycles: cycles 5, 50, 100, and 200. The broadening and increased splitting between the two peaks corresponding to the phase transitions between

the two O3 phases near 3.9 V during charge and discharge indicate a rapid impedance growth in the cell upon cycling. This impedance growth is similar to that for un-coated $LiCoO_2$ cycled to 4.5 V except that it occurs more rapidly here. A higher cutoff potential probably causes faster side reactions and subsequently faster impedance growth in the cell.

By comparing the differential capacity versus cell potential curves for the same cycle for the un-coated (Figure 7.2) and coated $LiCoO_2$ (Figure 7.3), it is clear that the impedance growth in the cell made with coated $LiCoO_2$ is much slower. Figure 7.3 shows that the two peaks corresponding to the transitions between the two O3 phases also shift apart and become broad as cycling continues. However, the splitting between charge and discharge peaks in Figure 7.3 is much smaller than that in Figure 7.2 at the same cycle. This indicates that the impedance growth is much slower for the cell made with the coated $LiCoO_2$. In the differential capacity versus potential curve (Figure 7.3) for the discharge of cycle 200, the differential capacity at 3.6 V is still very small even though the peak at about 3.8 V is broadened and slightly shifted to lower potential. This indicates that the cell will deliver little more discharge capacity if it is further discharged below 3.6 V. Therefore, the slight impedance growth is responsible for only some of the loss in discharge capacity by polarization over 200 cycles. Similarly, in the curve for the charge of cycle 200, the peak at about 4.55 V shifts very little toward higher potential as cycling continues. Therefore, the slight impedance growth causes little loss of charge capacity by polarization over 200 cycles. For the coated $LiCoO_2$, the impedance growth is significantly suppressed by coating and it appears that the capacity loss caused by impedance growth is little over 200 cycles.

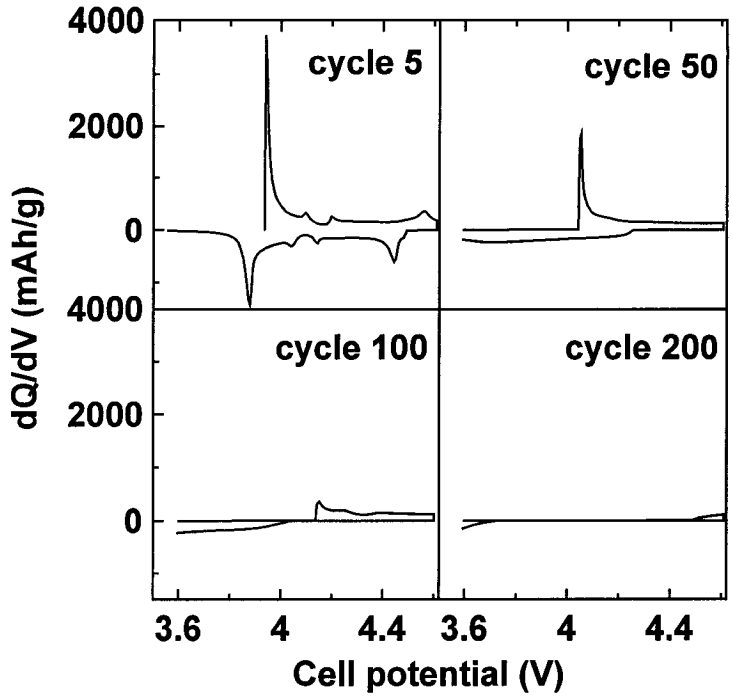

Figure 7.2 Differential capacity versus cell potential curve for four different cycles of a cell made with $LiCoO_2$ 010301.

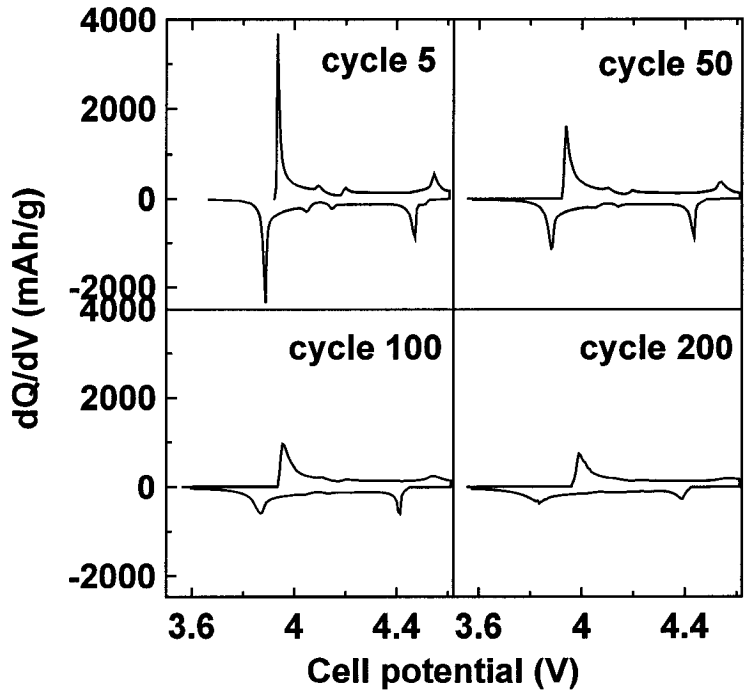

Figure 7.3 Differential capacity versus cell potential curve for four different cycles of a cell made with sample E.

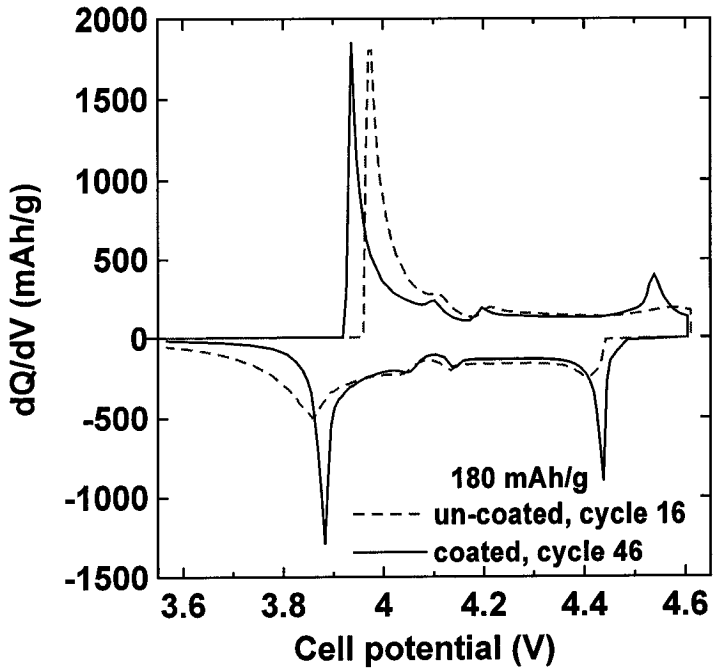

Figure 7.4 Differential capacity versus cell potential curves for two cells made with $LiCoO_2$ 010301 and sample E, respectively. For both cells, the specific capacity of $LiCoO_2$ is 180 mAh/g.

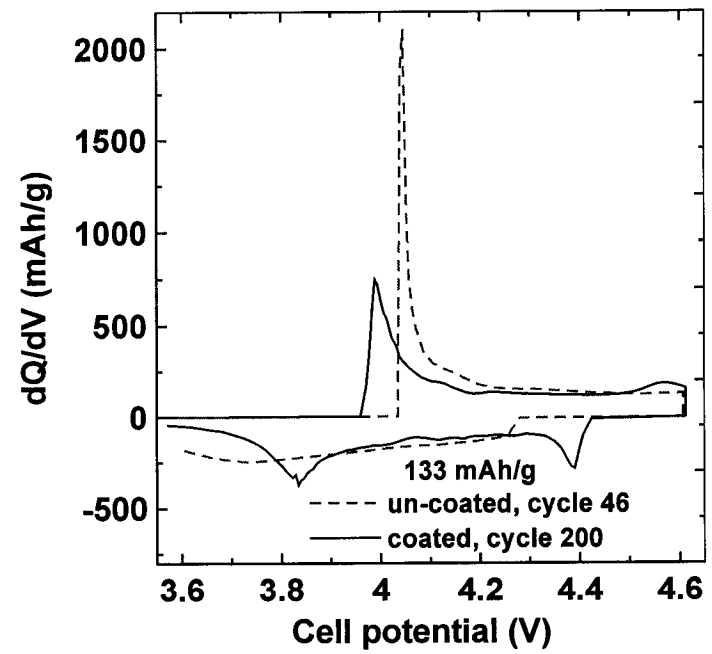

Figure 7.5 Differential capacity versus cell potential curves for two cells made with $LiCoO_2$ 010301 and sample E, respectively. For both cells, the specific capacity of $LiCoO_2$ is 133 mAh/g.

Figures 7.4 and 7.5 show a comparison between the differential capacity versus cell potential curves for the coated and un-coated $LiCoO_2$ having the same specific discharge capacity. Figure 7.4 compares cycles with a capacity of 180 mAh/g and Figure 7.5 compares cycles with a capacity of 133 mAh/g. By comparing the positions of peaks corresponding to a certain phase transition in both curves in Figure 7.4, it is clear that the cell made with the un-coated $LiCoO_2$ has larger impedance and hence has lost significant capacity by the impedance growth mechanism. This conclusion is also apparently supported by Figure 7.5.

The specific capacity of un-coated $LiCoO_2$ for cycle 46 is equal to that of the coated $LiCoO_2$ for cycle 200. Thus, both materials have lost the same amount of capacity up to the corresponding cycles. Since the un-coated $LiCoO_2$ has lost capacity by impedance growth, the coated $LiCoO_2$ must have lost more capacity by some other mechanism. Curve b in Figure 7.1 shows that the capacity decreases by about 30% after 200 cycles for the coated $LiCoO_2$. If the majority of the capacity loss was not caused by impedance growth, then perhaps it is caused by the loss of active material ($LiCoO_2$). The peaks at about 4.5 V in the differential capacity versus potential curve (as in Figure 7.4) indicate that $LiCoO_2$ experiences two more phase transitions (one during charge and another during discharge) when it is cycled to 4.6 V than when cycled to 4.5 V. The structural changes corresponding to the phase transitions which occurs during cycling above 4.5 V may cause some electrochemically active $LiCoO_2$ to convert into inactive material. Figure 7.6 illustrates the different mechanisms for capacity loss for both un-coated and coated $LiCoO_2$ cycled to 4.5 V and above 4.5 V respectively.

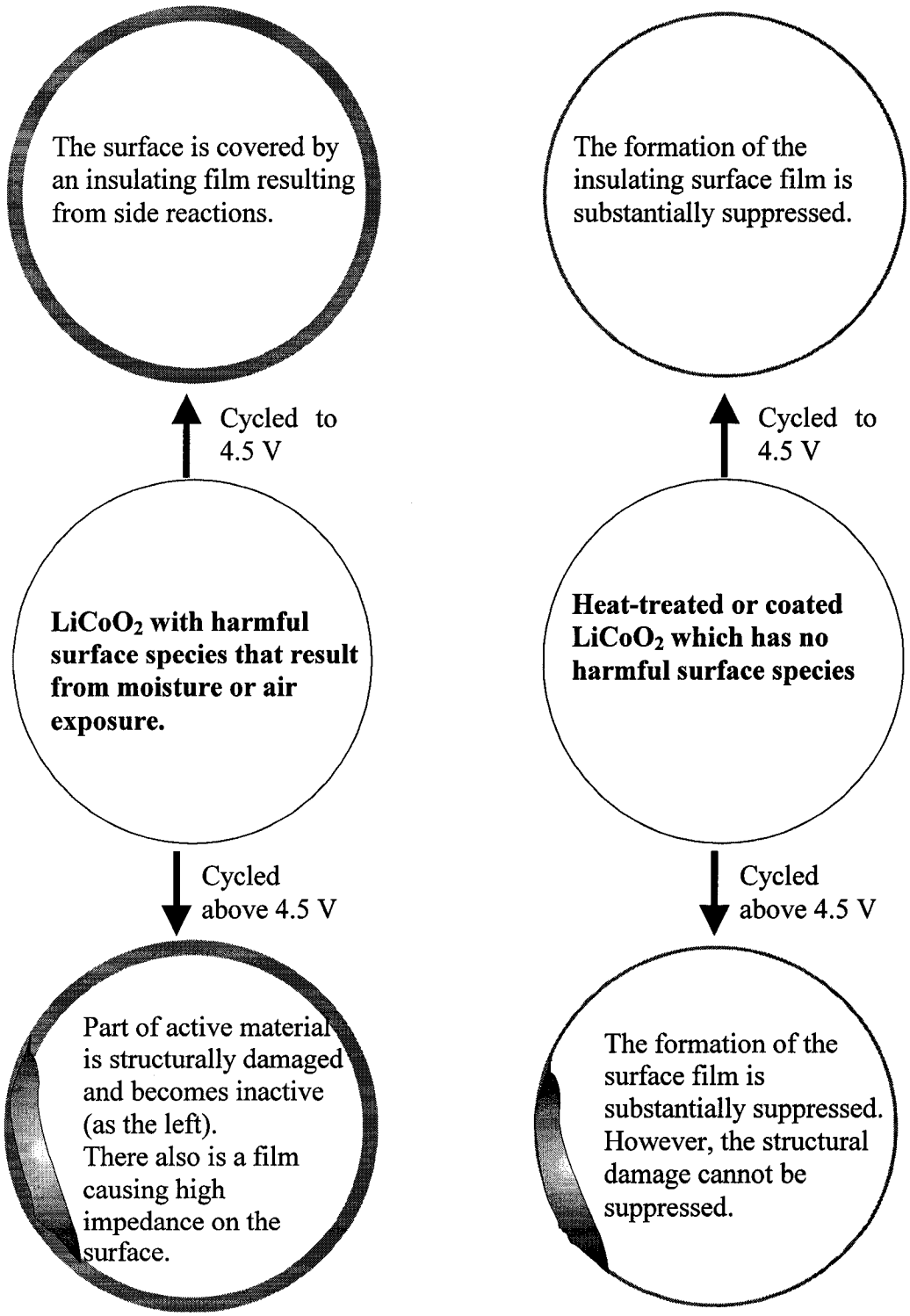

Figure 7.6 Schematic drawing showing the different capacity loss mechanisms for both un-coated and coated $LiCoO_2$ cycled to 4.5 V and to above 4.5 V.

7.3 Electrochemical behavior of coated and un-coated $LiCoO_2$ samples when cycled above 4.5 V

Figure 7.7 shows the voltage versus capacity for the first cycle of Li/$LiCoO_2$ cells using both un-coated and coated $LiCoO_2$ (sample J) with an upper cutoff potential of 5 V. The charge parts of both voltage curves are similar and the charge capacities for both materials are close to 270 mAh/g. This indicates that both materials were almost fully delithiated when charged to 5 V. In both charge curves, there are two small plateaus corresponding to the order-disorder phase transition near 135 mAh/g. The two plateaus at 4.55 and 4.63 V correspond to the two phase transitions from the O3 phase to the X-phase, and then to the O1 phase.

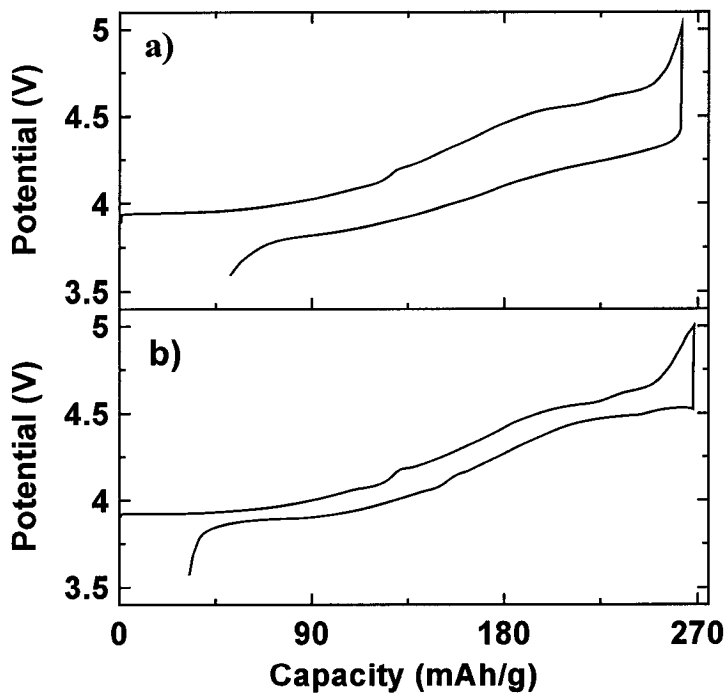

Figure 7.7 The voltage versus specific capacity for the first cycle of Li/$LiCoO_2$ cells with electrodes of (a) un-coated $LiCoO_2$ and (b) Al_2O_3 coated $LiCoO_2$, with an upper cutoff voltage of 5 V.

The discharge portions of the voltage-capacity curves for the two samples are quite different. There is no observable plateau in the discharge voltage profile for the un-coated $LiCoO_2$. In fact, the cell voltage dropped from 5 V to about 4.3 V immediately after the discharge began. The average potential of the discharge curve is much lower than the average potential of the charge curve. This experiment shows that un-coated $LiCoO_2$ cannot be reversibly cycled with an upper cutoff voltage of 5 V. On the contrary, the discharge curve of the coated $LiCoO_2$ shows much better reversibility. All the plateaus observed during charge have counterparts in the discharge curve of the coated sample.

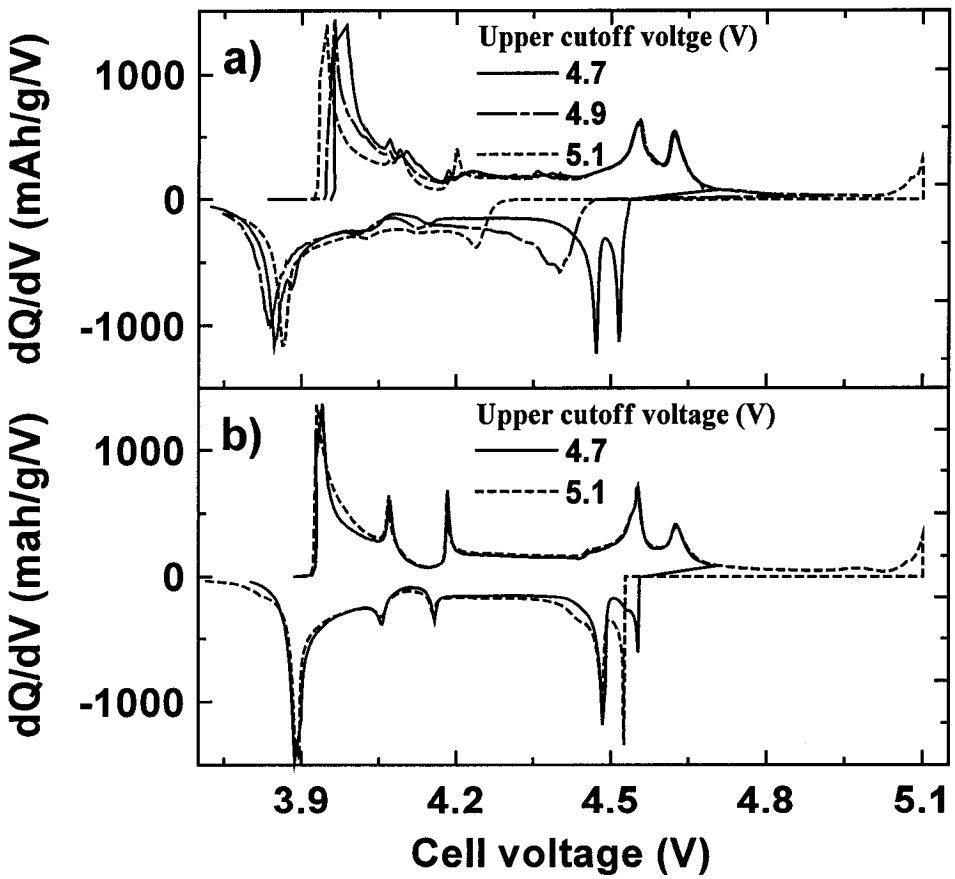

Figure 7.8 Differential capacity versus voltage for the first cycle of Li/$LiCoO_2$ cells with electrodes of (a) un-coated $LiCoO_2$ and (b) Al_2O_3 coated $LiCoO_2$, with different upper cutoff voltages (Chen Z. H. and Dahn J. R., 2002c).

When the differential capacity, dQ/dV, is plotted versus the cell potential, plateaus in voltage-capacity curves appear as peaks in dQ/dV. Figure 7.8 shows dQ/dV versus voltage for the first cycle of Li/$LiCoO_2$ cells having positive electrodes of un-coated $LiCoO_2$ and coated $LiCoO_2$ sample J. Different upper cutoff voltages were employed. In order to make the features in high voltage regions more apparent, the intense peaks near 3.9 V have been cut off for both materials. Figures 7.8(a) and 7.8(b) show that all the charge curves have two peaks at 4.55 and 4.63 V, respectively. These two peaks, corresponding to the two highest plateaus in the charge curves in Figure 7.7, represent the phase transitions from the O3 phase to the X-phase and then to the O1 phase. Therefore, these two phase transitions can be observed electrochemically.

Figure 7.8 suggests that if Li/$LiCoO_2$ cells are charged to 4.5 V, then Li_xCoO_2 is still in the O3 phase. If the cells are charged to 4.6 V, Li_xCoO_2 is in the X-phase. If the cells are charged to 4.7 V, most $LiCoO_2$ is in the O1 phase. Further increases to the upper cutoff potential did not uncover further reversible capacity. For the cells charged to above 5 V, the dQ/dV curve shows another peak for both materials. This peak is caused by electrolyte decomposition at high potential.

There are two peaks in the discharge part of some dQ/dV curves that correspond to the reverse reactions of the 4.55 and 4.63 V peaks in the charge curves. This indicates that the two phase-transitions are reversible under certain conditions. When the un-coated $LiCoO_2$ is charged to above 4.8 V, the two phase transitions are no longer reversible. The two sharp peaks near 4.5 V in the discharge curve become one broad peak. As the upper cutoff voltage increases to 5.1 V, the broad peak shifts to lower potential and becomes weaker. By contrast, for the Li/$LiCoO_2$ cell with the coated

$LiCoO_2$ electrode, there are two peaks in its discharge dQ/dV versus voltage curve even after charging to 5.1 V. This indicates that surface coating with Al_2O_3 improves the stability and reversibility of $LiCoO_2$ during cycling to high cutoff potentials. Therefore, coated $LiCoO_2$ was used for *in-situ* XRD studies.

7.4 *In-situ* XRD of coated $LiCoO_2$

As shown above, the two phase transitions from the O3 phase to the X-phase and then to the O1 phase during a charge are reversible for $LiCoO_2$ coated with Al_2O_3. Using the *in-situ* X-ray diffraction technique, this reversible process can be observed more directly. Figures 7.9 and 7.10 show the XRD patterns of Li_xCoO_2 coated with Al_2O_3 taken between 4.5 V and 4.75 V during the charge and between 4.75 V and 4.4 V during the discharge. In Figure 7.9, during the charge, the (003) peak from the O3 phase gradually disappears, and a peak from the X-phase simultaneously grows. After this phase transition is finished, the peak from the X-phase diminishes, while the (001) peak from the O1 phase grows. At 4.75 V, one can see the (001) peak from the O1 phase in the corresponding XRD pattern even though there is a broad shoulder on its left side that indicates the phase transition is not complete yet. During discharge, the phase transitions occur reversibly. Figure 7.10 shows a region of the *in-situ* XRD patterns at higher scattering angle. It also clearly shows these reversible phase transitions.

Amatucci *et al.* (1996) also performed *in-situ* studies during a discharge of Li/Li_xCoO_2 cells. In their experiment, the cell voltage dropped to 4.35 V as soon as the *in-situ* cell was placed on discharge after charging to 5.2 V. This phenomenon is very similar to that observed in Figure 7.8(a) for un-coated materials. In Figure 7.8(a), for the

cell made with un-coated $LiCoO_2$ and charged to 5.1 V, the cell voltage dropped to 4.32 V as soon as the discharge began. The two phase transitions from the O1 phase to the X-phase and then to the O3 phase are not apparent in the dQ/dV vs voltage data. Therefore, it is not surprising that Amatucci *et al.* (1996) did not observe these two phase transitions during the discharge of un-coated $LiCoO_2$ by *in-situ* X-ray diffraction.

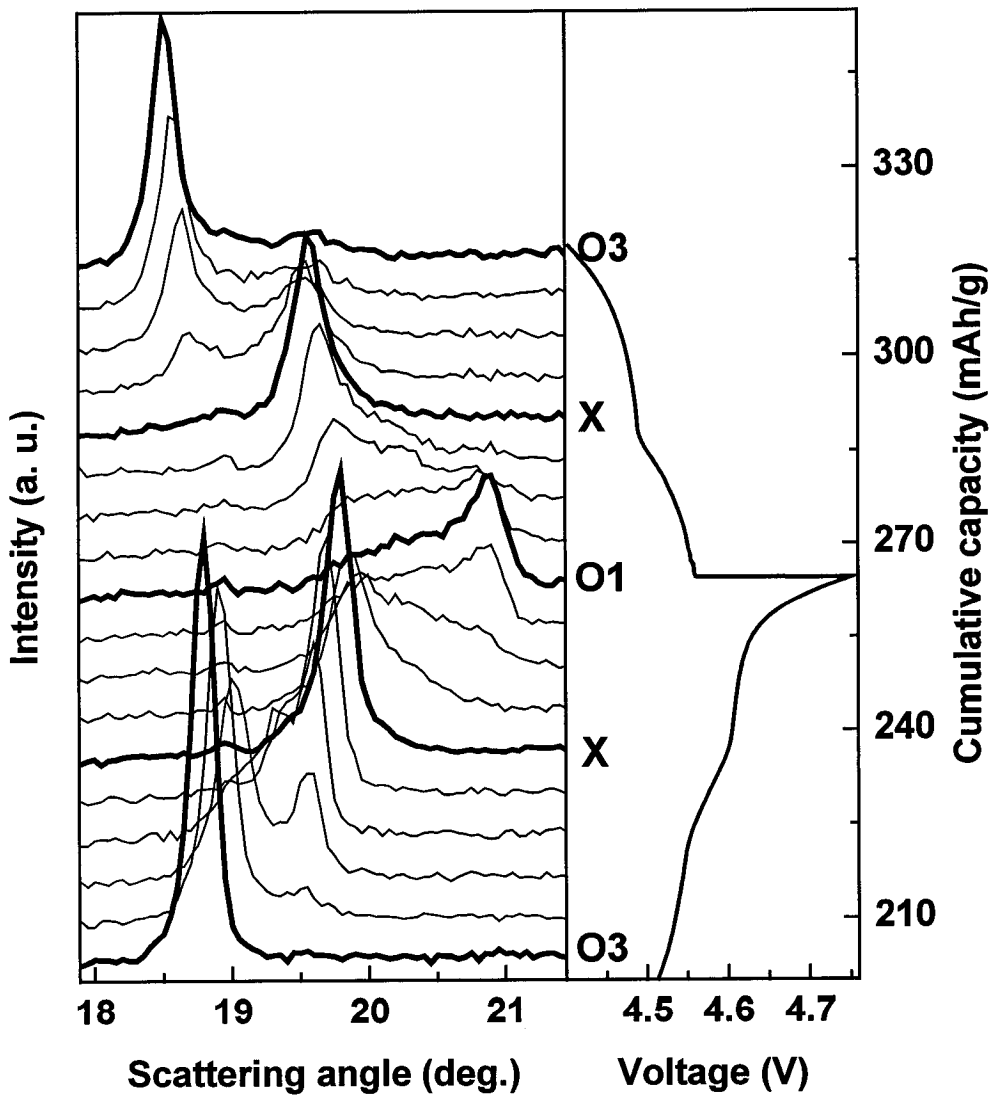

Figure 7.9 A selected range of the in-situ XRD patterns as well as the voltage-time curve of the in-situ cell (Chen Z. H. and Dahn J. R., 2002c).

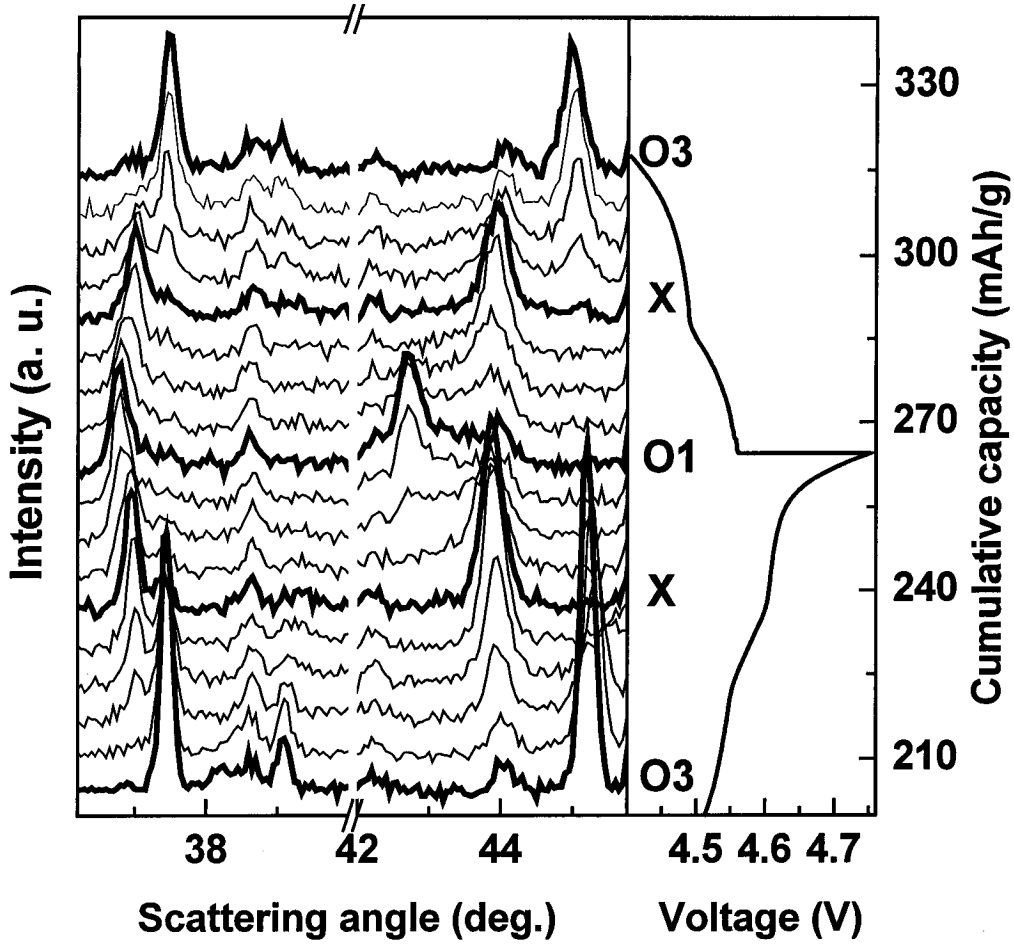

Figure 7.10 A selected range of the in-situ XRD patterns as well as the voltage-time curve of the in-situ cell.

7.5 Determination of the structure of X-phase by ex-situ XRD and Rietveld refinement

The *in-situ* XRD pattern for X-phase in this study is very similar to the corresponding XRD patterns from the *in-situ* results of Amatucci *et al.* (1996) and Sun *et al.* (2001). It also agrees qualitatively with the calculated pattern of the H1-3 phase from Ceder's work. This indicates that X-phase may have a H1-3 structure. To verify this, an *ex-situ* XRD pattern was obtained from an electrode charged to 4.6 V as described in the experimental section.

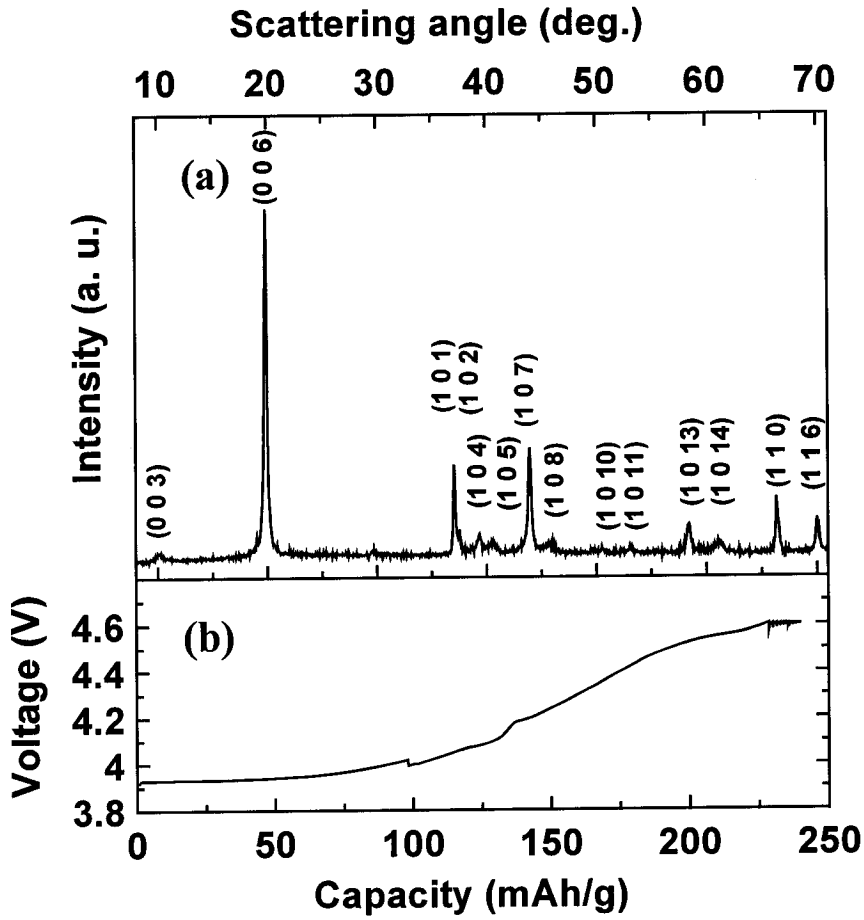

Figure 7.11 (a) Ex-situ XRD pattern indexed with the six-layer structure. (b) Voltage-capacity curve of the ex-situ cell used to collect the pattern in a).

Figure 7.11(b) shows the voltage profile of the cell that was used for the *ex-situ* analysis. The voltage drop at a capacity of about 100 mAh/g was caused by an interruption of the charge current. The plateau between 4.5 V and 4.6 V indicates that the O3 phase transformed to the X-phase. The best estimate of the composition of the X-phase is $Li_{0.12}CoO_2$, based on the results in Figures 7.9, 7.10, and 7.11. Figure 7.11(a) shows the XRD pattern obtained by adding the first three *ex-situ* scans together to obtain a better signal to noise ratio. According to Van der Ven *et al.* (1998a and 1998b), the structure of X-phase should be a *stage-2* structure. In the *stage-2* structure, lithium atoms

in every other Li layer in the O3 structure of Li_xCoO_2 are totally removed. According to Van der Ven, the adjacent CoO_2 sandwiches now shift to the stacking found in the O1 phase while the CoO_2 sandwiches that are still separated by lithium retain the original stacking arrangement found in the O3 phase. Since this is a "hybrid" of the O1 and O3 structures, Van der Ven *et al.* (1998a and 1998b) called it the H1-3 structure.

In the notation of hexagonal close packed layers the stacking of the oxygen (capital letters), cobalt (lower case letters) and lithium atoms (Greek symbols) in the H1-3 phase is

|BcA_BcAβCaB_CaBγAbC_AbCα|BcA,

where the vertical bars (|) span the repeating unit. Thus, six CoO_2 slabs are needed to form a unit cell of this structure. Figure 7.11(a) shows that this *ex-situ* XRD pattern can be well indexed as a single H1-3 phase. The lattice constants of this phase, determined by least-square fitting to the measured positions of the Bragg peak positions of the main peaks, are a = 2.823 ± 0.002 Å and c = 27.07 ± 0.03 Å. Table 7.1 shows a comparison between the measured peak positions and the calculated ones assuming the H1-3 structure.

The H1-3 phase takes the R-3m space group with Li occupying 3a sites, and Co and the two oxygen atoms in three different 6c sites. With this structural information and the lattice constants obtained above, a Rietveld refinement was performed for this *ex-situ* XRD pattern. The results are listed in Table 7.2. Figure 7.12 shows the *ex-situ* XRD pattern and the calculated pattern based on the best Rietveld fit. It was noticed that the *ex-situ* XRD patterns from consecutive one-hour scans were slightly different, which means that the H1-3 phase is not very stable even when sealed in the helium-filled holder.

Taking this into account, the refinement of the *ex-situ* XRD pattern with the H1-3 structure is very good. Based on this refinement, it is confirmed that X-phase has an H1-3 structure as predicted by Van der Ven *et al.* (1998a and 1998b). Based on the results of the refinement, Figure 7.13 was made to show the atom positions in the H1-3 structure.

Table 7.1 Experimental and calculated peak positions for the diffraction pattern of the H1-3 phase. The lattice constants used in the calculation were a = 2.823 Å and c = 27.07 Å.

h k l	2θ observed (degree)	2θ calculated (degree)	Difference (degree)
0 0 3*	9.9	9.804	
0 0 6	19.777	19.719	0.058
1 0 1	36.933	36.960	-0.028
1 0 2	37.432	37.424	0.008
1 0 4	39.220	39.230	-0.010
0 1 5*	40.4	40.488	
1 0 7	43.817	43.874	-0.057
0 1 11*	52.9	52.787	
1 0 13	58.287	58.305	-0.017
1 0 14*	61.0	61.112	
1 1 0	66.241	66.235	0.006
1 1 6	69.893	69.852	0.041

* Peak not used for the least-square fitting due to its weak intensity and uncertain peak position.

Table 7.2 Rietevld refinement results for the ex-situ XRD pattern. The space group used was R-3m. (The occupancy for Li is 0.24 and the occupancies for Co, O1 and O2 are 1.)

a = 2.8193 +- 0.0004 Å			c = 27.035 +- 0.011 Å	
R_B = 4.7%				
	site	x	y	z
Li	3a	0	0	0
Co	6c	0	0	0.42150 +- 0.00016
O1	6c	0	0	0.27671 +- 0.00045
O2	6c	0	0	0.11535 +- 0.00045

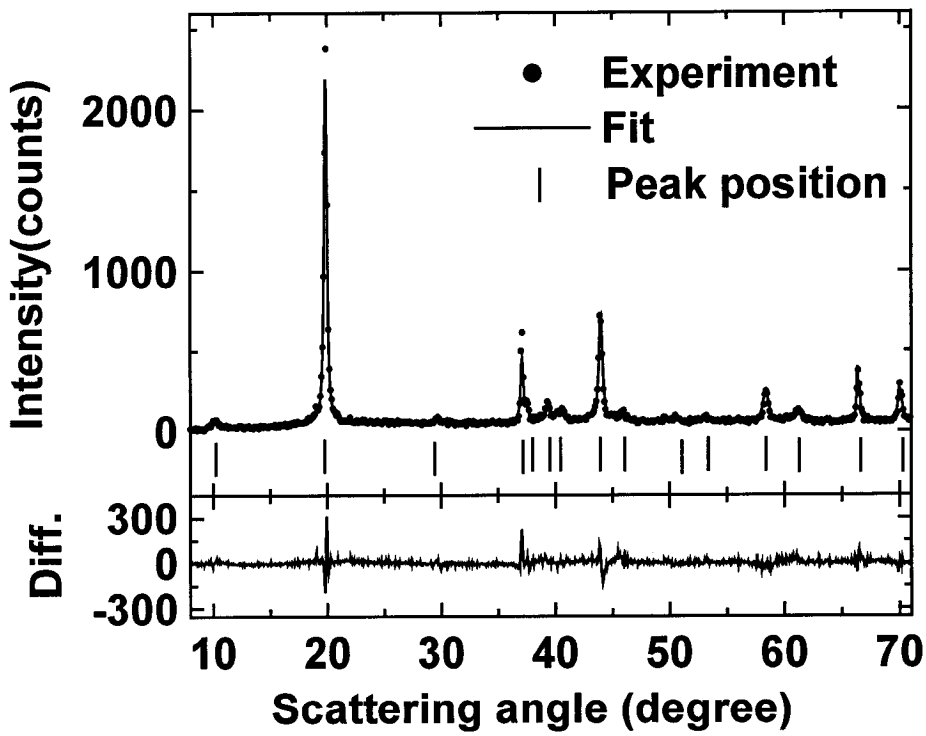

Figure 7.12 A comparison of the ex-situ XRD pattern and the calculated pattern from the best Rietveld refinement (Chen Z. H. and Dahn J. R., 2002c).

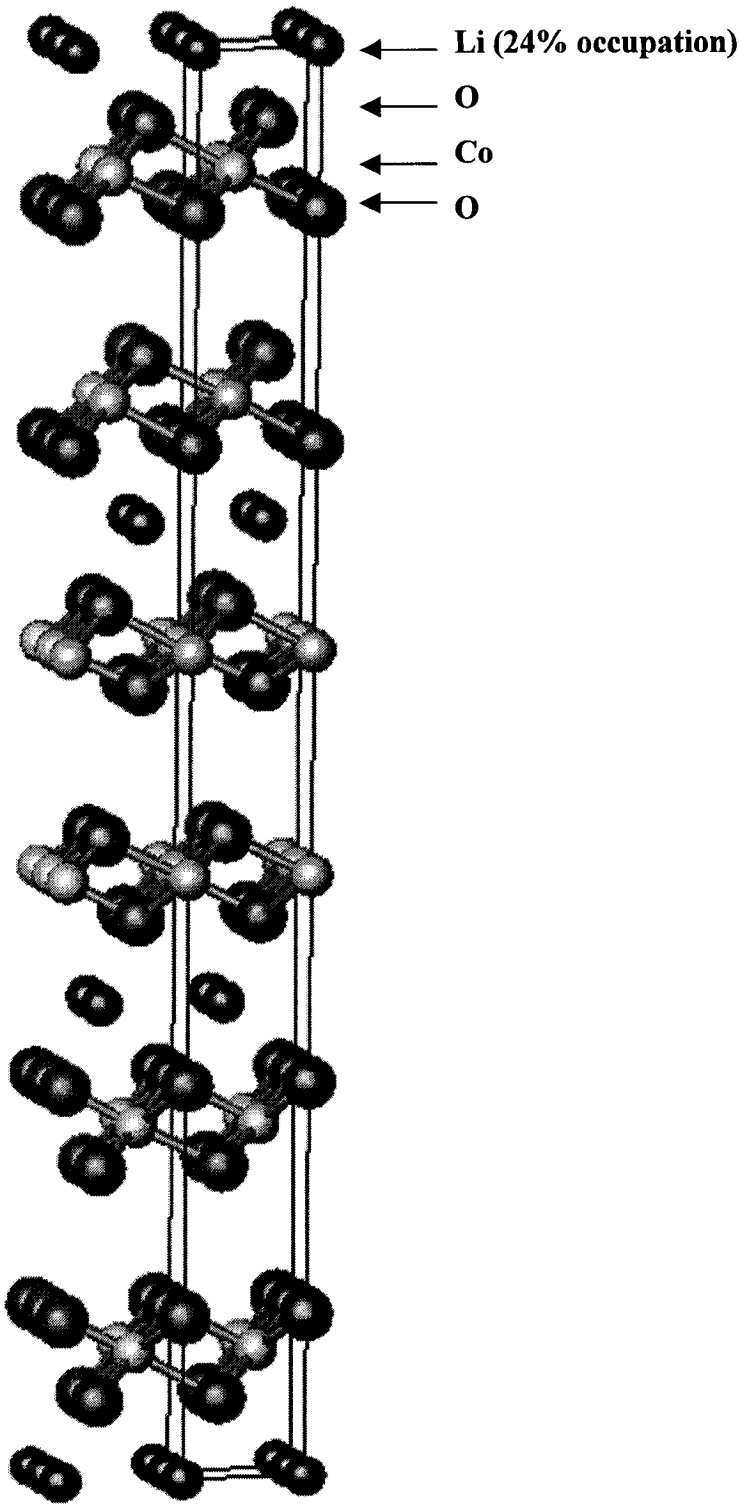

Figure 7.13 A view of the H1-3 structure calculated using the results of the best Rietveld refinement (Only about 24% of the Li sites in the Li-containing planes are occupied).

7.6 More staged phases?

It was confirmed above that there is a staging phase transition in Li_xCoO_2 during the charge of $Li/LiCoO_2$ cells to near 4.6 V. In addition to *stage-2*, other staged phases may appear. A careful investigation of Figure 7.9 reveals some interesting features. In the region of the phase transition from the O3 phase to the H1-3 phase during the charge, the two XRD patterns taken before the H1-3 phase was completely formed show a small peak between the (003) peak from O3 and the (006) peak from H1-3. This indicates that there may be another staged phase formed.

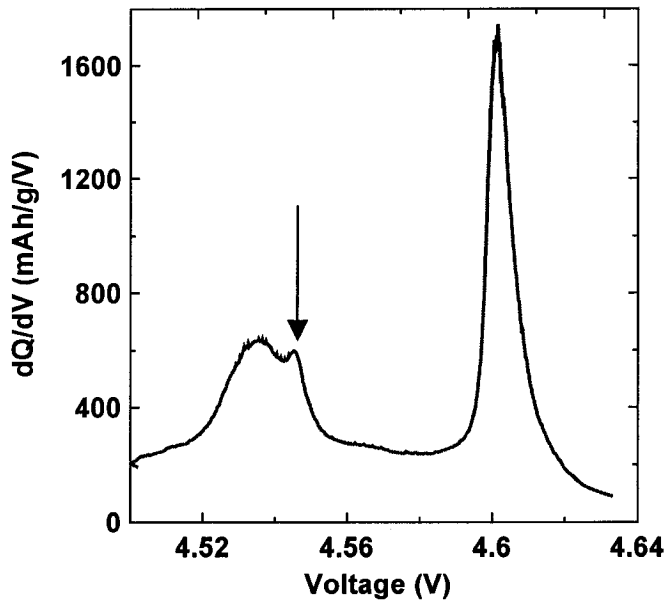

Figure 7.14 The differential capacity versus voltage of a $Li/LiCoO_2$ cell made with Al_2O_3 coated $LiCoO_2$ and charged with a current of 0.5 mA/g.

In order to observe further evidence for this multiple staging, a $Li/LiCoO_2$ cell was charged with a current of 0.5 mA/g above 4.5 V. Figure 7.14 shows the dQ/dV versus voltage curve for this cell. It shows the splitting of the peak representing the phase transition from the O3 phase to the H1-3 phase observed before. Therefore, there

may be multiple phase transitions during the transition from the O3 phase to the H1-3 phase during the charge. However, to be sure about this multiple phase transition, further work is needed.

7.7 Structural changes during a phase transition from the $Li_{1-x}CoO_2$ O3 phase to the H1-3 phase

Figures 7.15a and 7.15b schematically show the stacking of the O-Co-O slabs of the $Li_{1-x}CoO_2$ O3 phase and those of the $Li_{1-x}CoO_2$ H1-3 phase, respectively, in the c direction. In the O3 structure, Li atoms partially fill each interlayer space between the O-Co-O slabs while only every second interlayer space is filled with Li atoms in the H1-3 structure. In the O3 structure, any two O-Co-O slabs next to each other have an O3 type. The H1-3 structure is a hybrid structure of O1 and O3 structures. Each O-Co-O slab and one of its nearest neighbor slabs have an O3-type stacking with a Li layer between them. This slab and the other nearest neighbor slab in the opposite direction have an O1-type stacking without Li atoms between them. During a phase transition from the O3 phase to the H1-3 phase, the Li atoms in every second interlayer space must be completely removed to create an O1-type stacking for the two O-Co-O slabs next to the Li layer. Simultaneously, the two slabs shift with respect to each other by a distance of 1.62Å. This shifting happens to each O-Co-O slab with one of its nearest neighbor slabs. Compared with the structural changes below 4.5V, such as the O3/O3 phase transition and the order/disorder phase transitions, this structural change is more severe. Repeated structural changes like this during cycling above 4.5 V may cause irreversible damage to structure of $LiCoO_2$ and subsequently result in capacity fading.

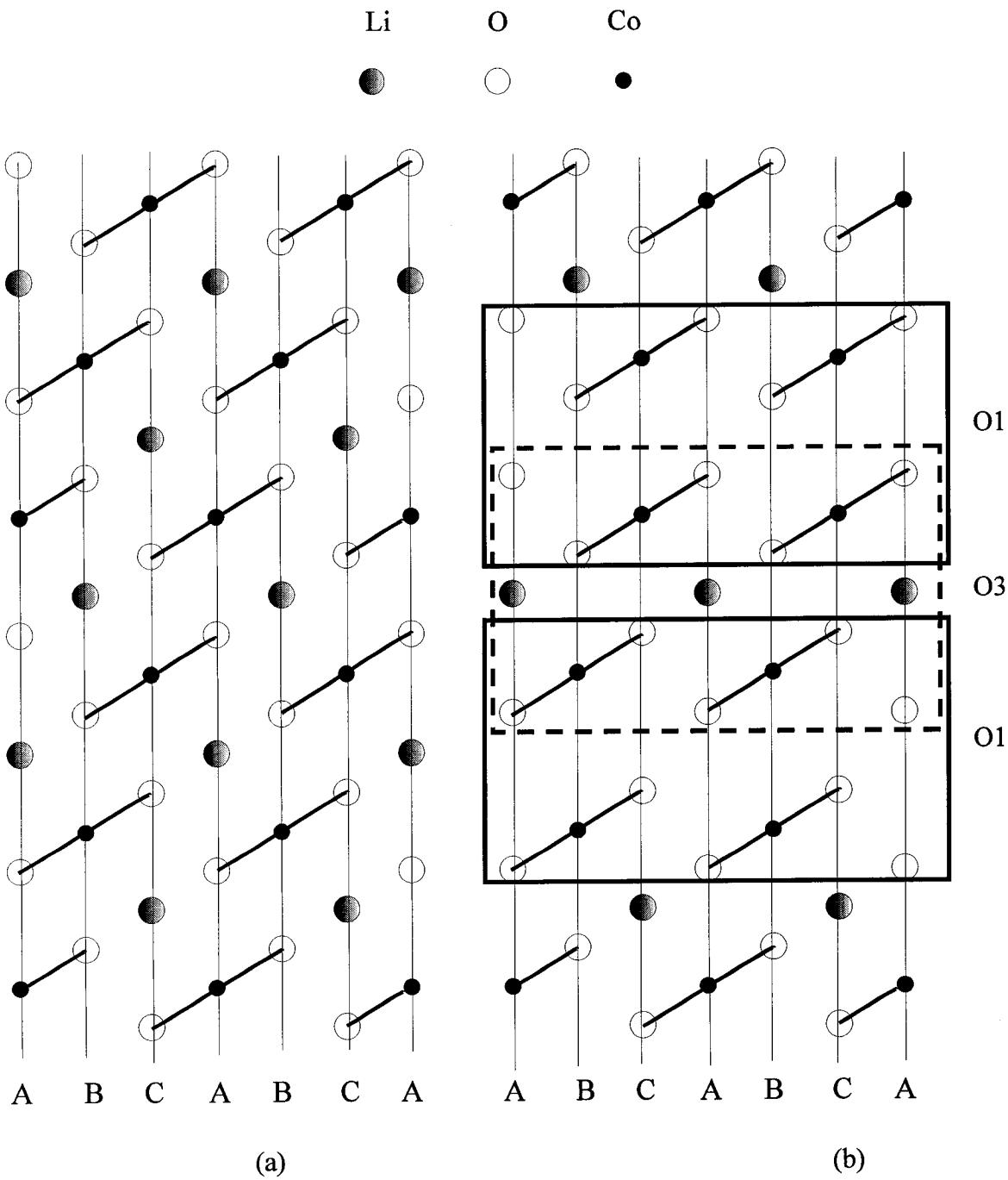

Figure 7.15 Schematic drawing of the stacking, in the c direction, of the O-Co-O slabs of $Li_{1-x}CoO_2$ in (a) the O3 phase and (b) the H1-3 phase.

Cycling to above 4.6 V involves a phase transition between the H1-3 and O1 structures. The structural changes involve removing all the rest of the Li atoms and

transforming the remaining O3-type stacking to O1-type stacking. These changes are similar to those during a phase transition from the O3 structure to the H1-3 structure.

7.8 Summary

The two plateaus above 4.5 V in the voltage-capacity curves of Li/$LiCoO_2$ cells, representing the sequential phase transitions from the O3 phase to the H1-3 phase and from the H1-3 phase to the O1 phase, have been observed for the first time. The two phase transitions are reversible for an upper cutoff voltage of 4.7 V, but not for 4.8 V or above for un-heated $LiCoO_2$. However, if the $LiCoO_2$ is coated with Al_2O_3, then the two phase transitions are reversible even with an upper cutoff voltage of 5.1 V. *In-situ* XRD experiments also show these two phase transitions during a charge of the coated $LiCoO_2$ to 4.75 V and the corresponding phase transitions during the subsequent discharge. A Rietveld refinement of an *ex-situ* XRD pattern obtained from an electrode charged to 4.6 V confirmed that this is the *stage-2* compound proposed by Van der Ven *et al.* (1998a and 1998b) from first-principles. It is believed that the composition of this phase is $Li_{0.12}CoO_2$. *In-situ* XRD results and differential capacity measurements of a Li/$LiCoO_2$ cell charged with a specific current of only 0.5 mA/g provide evidence for another phase transition near 4.54 V during the charge of $LiCoO_2$. Furthermore, it was speculated that the severe structural changes during the phase transition between the O3 phase and the H1-3 phase may be responsible for the capacity fading of $Li_{1-x}CoO_2$ cycled to 4.6 V when the impedance growth caused by side reactions is suppressed by coating or other methods.

Chapter 8 Conclusions and future work

8.1 Conclusions

Developing electrode materials with a higher energy density has been one of the major focuses for scientists and engineers in the battery field. Cho's recent work on coatings has inspired world-wide efforts to improve the energy density of $LiCoO_2$. The main focus of this thesis is also to improve the energy density of $LiCoO_2$ without sacrificing its capacity retention.

It has been proven that, with fresh surfaces, $LiCoO_2$ can be cycled to 4.5 V and deliver a capacity of about 180 mAh/g in a $LiPF_6$-based electrolyte with excellent capacity retention. The poor capacity retention of $LiCoO_2$ cycled to 4.4 or 4.5 V as reported is caused by impedance growth in the cell, which apparently results from side reactions involving $LiPF_6$-based electrolytes and surface species caused by air or moisture exposure. Therefore, for $LiCoO_2$ stored in air and possibly exposed to moisture, capacity retention when cycled to 4.5 V can be improved by suppressing these side reactions using the following methods:

(a) Creating fresh $LiCoO_2$ surfaces by grinding or heating to a high temperature (550°C or above was tested here).

(b) Fumed SiO_2 addition to a $LiPF_6$-based electrolyte for Li metal cells.

A combination of (a) with (b) can further improve the capacity retention. A heat-treated $LiCoO_2$ has even better capacity retention in a LiBOB-based electrolyte than in a $LiPF_6$-based electrolyte.

In addition, $LiCoO_2$ samples coated with ZrO_2, Al_2O_3, and SiO_2 have excellent capacity retention when charged to 4.5 V, even with a lower cutoff potential of 3.6 V. The capacity retention of coated $LiCoO_2$ is independent of the fracture toughness of the coated oxide. Since a heat-treatment alone substantially improves the capacity retention of $LiCoO_2$ cycled to 4.5 V whereas Al_2O_3 addition in the electrolyte has little or no effect, it is believed that the improvement in the capacity retention of $LiCoO_2$ cycled to 4.5 V by coating with oxides is mainly due to the heating process.

When charged to 4.5 V with respect to Li metal, $Li_{1-x}CoO_2$ has an O3 structure. With further charging, the structure changes from the O3 phase to an H1-3 phase, and then to an O1 phase when the Li is completely removed. These two phase transitions were observed both electrochemically and structurally for the first time. An XRD study confirmed that the phase between the O3 phase and the O1phase has an H1-3 structure, as predicted by Ceder's group using first-principles calculation.

The impedance growth in a $Li/LiCoO_2$ cell can be significantly suppressed for cycling to 4.6 V or above with respect to Li metal. However, the capacity retention of coated $LiCoO_2$ is still unacceptable for industrial applications. Structural changes between the O3 phase and the H1-3 phase are believed to cause structural damage and subsequent capacity fading.

Besides the work on $LiCoO_2$, an effort was also made to reduce the carbon content in a $LiFePO_4/C$ composite without sacrificing rate capability. It was found that coating with only about 3% carbon by weight maintains both a good rate capability and a high pellet density for the composite.

8.2 Future work

(a) Develop safe batteries with $LiCoO_2$ cycled to high potentials. Based on the conclusions, $LiCoO_2$ cycles well with an upper cutoff potential of 4.5 V and delivers a capacity of 180 mAh/g, which is more than that used in a commercial cell. However, for industrial applications, other factors, such as safety, must be considered. Considering the safety problem for large Li-ion batteries even with $Li_{1-x}CoO_2$ charged to only 4.2 V, the safety of batteries with $LiCoO_2$ charged to 4.5 V must be studied before commercialization. Despite its appealing energy density, more work is needed to determine how to make safe cells with $LiCoO_2$ cycled to above 4.2 V.

(b) Understand the chemical reactions occurring in a $LiCoO_2$ cell. It is certain that some chemical species on the surface of $LiCoO_2$, which are caused by exposure to air or moisture, cause the poor capacity retention of $LiCoO_2$ when cycled to 4.5 V. Surface analysis is needed to identify these species. To understand how the presence of these species and $LiPF_6$ cause impedance growth, the surface of $LiCoO_2$ cycled to 4.5 V for 100 times or more need to be studied by surface analysis. In addition, the mechanism of the improvement in capacity retention by the addition of SiO_2 needs to be understood. This requires an understanding of the chemical reactions between SiO_2, $LiPF_6$-based electrolyte, and the surface species on $LiCoO_2$.

(c) Improve capacity retention of $Li[Ni_xCo_{1-2x}Mn_x]O_2$. $Li[Ni_xCo_{1-2x}Mn_x]O_2$ has been reported as an positive electrode material for Li-ion batteries with a high specific capacity. It is a very safe material even when charged to high potentials (4.4 V or above). However, its capacity retention has to be improved before it can be widely commercialized. Preliminary work has indicated that coating with oxides is an effective

way to improve its capacity retention. To improve its capacity retention further, systematic work has to be done. With its improved cycling behavior, high specific capacity, lower price, and improved safety, it will be an attractive positive electrode material for Li-ion batteries.

(d) Investigating capacity retention of $LiCoO_2$ when cycled to 4.5 V with LiBOB or other salts. LiBOB was found helpful to suppress the impedance growth in the cell when $LiCoO_2$ is cycled to 4.5 V. However, for some $LiCoO_2$ samples having very poor capacity retention in $LiPF_6$-based electrolyte, LiBOB give no improvement. To improve the capacity retention of $LiCoO_2$ cycled to 4.5 V further, more understanding on the effect of substituting $LiPF_6$ with LiBOB or other salts is needed.

(e) Verifying the structure damage caused by cycling above 4.5 V. Chapter 7 has shown that the structure change during the phase transitions above 4.5 V is more severe than those during the phase transitions below 4.5 V. A XRD or TEM study on a completely discharged $LiCoO_2$ electrode which has undergone prolonged cycling to 4.6 V should be able to reveal phases other than O3 $LiCoO_2$ if there are any.

(f) Suppressing staging phase transitions by substituting Co. The order/disorder phase transition can be suppressed by 2 % substitution of Co (Reimers and Dahn, 1993). It is worthwhile to investigate if the staging phase transition can be suppressed in the same way and how the suppression of the staging phase transition will affect the capacity retention of $LiCoO_2$ cycled above 4.5 V.

References

Amatucci G. G., Tarascon J. M., Klein L. C., *J. Electrochem. Soc.*, **143** (3), 1114 (1996).

Aurbach D., Markovsky B., Rodkin A., Levi E., Cohen Y. S., Palchik O, Kim H. –J., and Schmidt M., *Electrochimica Acta*, **47**, 4291 (2002).

Caurant D., Baffier N., Garcia B., PereiraRamos J. P., *Solid State Ionics*, **91** (1-2), 45 (1996).

Chen Z. H. and Dahn J. R., *J. Electrochem. Soc.* 149(9), A1184 (2002a).

Chen Z. H. and Dahn J. R., *Elect. Solid-State Letts.* 5(10), A213-A216 (2002b).

Chen Z. H., Lu Z. H., and Dahn J. R., *J. Electrochem. Soc.* 149(12), A1604 (2002c).

Chen Z. H. and Dahn J. R., accepted for publication by *Elect. Solid-State Letts.* (2003a).

Chen Z. H. and Dahn J. R., Submitted to *Elect. Solid-State Letts.* (2003b).

Cho J. and Kim G., *Electrochem. Solid-State Lett.*, **2** (6), 253 (1999).

Cho J., Kim C. and Yoo S. I., *Electrochem. Solid-State Lett.*, **3** (8), 362 (2000a).

Cho J., Kim Y. J., and Park B., *Chem. Mater*, **12** (12), 3788 (2000b).

Cho J., Kim Y. J., and Park B., *J. Electrochem. Soc.*, **148** (10), A1110 (2001a).

Cho J., Kim Y. J., Kim T. J., and Park B., *Angew. Chem. Int. Ed.*, **40** (18), 3367 (2001b).

Cullity B. D., *X-ray Diffraction*, Addison-Wesley Publishing Company, Inc., Reading, MA (1967).

Dahn J. R., Py M. A., and Haering R. R., *Canadian Journal of Physics*, **60**, 307 (1981).

Gao Y., Yakovleva M., Wang H. H., Engel J. F., United States Patent Application, Pub. No.: US 2002/0015887 A1.

Godz A., Scmutz C., Tarascon J-M, Warren P., International Patent Application: PCT/US1994/08772.

Huang H., Yin S. C., and Nazar L. F., *Electrochem. Solid-State Lett.*, **4**, A170 (2001).

Kannan A. M., Rabenberg L. and Manthiram A., *Electrochem. Solid-State Lett.*, **7** (1), A16 (2002).

Liu L., Wang Z., Li H., Chen L., Huang X., *Electrochem. Solid State Ionics.*, **152**, 341 (2002).

Lu Z. H., Dahn J. R., *Electrochem. Solid-State Lett.*, **4**, A200 (2001).

Lu Z. H., Dahn J. R., *J. Electrochem. Soc.*, **149** (6), A778 (2002).

D. D. MacNeil, Z. Lu, Z. Chen, and J. R. Dahn, *J. Power Sources*, **108** (1-2), 8 (2002).

Matthews J., *ZDNetAsia,* "'Alien' substance caused Dell notebook battery to ignite", October 20, 2000.

Padhi A. K., Nanjundaswamy K. S., and Goodenough J. B., *J. Electrochem. Soc.*, **144**, 1188 (1997).

Ravet N., Goodenough J. B., Besner S., Simoneau M., Hovington P., and Armand M., Abstract 127, The Electrochemical Society and The Electrochemical Society of Japan Meeting Abstarct, Vol. 99-2, Honolulu, HI, Oct. 17-22 1999.

Ravet N., Chouinard Y., Magnan J. F., Besner S., Gauthier M., and Armand M., *J. Power Sources*, **97-98**, 503 (2001).

Reimers J. N. and Dahn J. R., *J. Electrochem. Soc.*, **139** (8), 2091 (1992).

Richard M. N., Koetschau I., Dahn J. R., *J. Electrochem. Soc.* **144**, 554 (1997)

Rietveld H. M., *J. Appl. Crystallogr.*, **22**, 151 (1967).

Obrovac M. N., Ph.D. Thesis, the Department of Physics, Dalhousie University (2001).

Ohzuku T. and Ueda A., *J. Electrochem. Soc.*, **141** (11), 2972 (1994).

Reimer L., *Transmission Electron Microscopy*, Springer-Verlag, Berlin (1984).

Sun X., Yang X. Q., McBreen J., Gao Y., Yahovleva M. V., Xing X. K., Daroux M. L., *J. Power Sources*, **97-98**, 274 (2001).

Takeshita H., The 20th International Seminar & Exhibit on primary & Secondary Batteries, March 17, 2003, Florida, United States.

Thackeray M. M, Dekock A., Rossouw M. H., Liles D., Bittihn R., Hoged D., *J. Electrochem. Soc.*, **139** (2), 363 (1992).

Van der Ven A., Aydinol M. K., and Ceder G., *Phys. Rev. B*, **58**, 2975 (1998a).

Van der Ven A., Aydinol M. K., and Ceder G., *J. Electrochem. Soc.*, **145** (6), 2149 (1998b).

Wang H., Jang Y., Huang B., Sadoway D. R., and Chang Y., *J. Electrochem. Soc.*, **146** (2), 473 (1999).

Wang Z., Wu C., Liu L., Chen L., Huang X., *Solid State Ionics.*, **148**, 335 (2002a).

Wang Z., Wu C., Liu L., Wu F., Chen L., Huang X., *J. Electrochem. Soc.*, **149** (4), A466 (2002b).

Warren B. E., *X-ray Diffraction,* Addison-Wesley Publishing Company, Inc., Reading, MA (1969).

Xu K., Zhang S., Jow T. R., Xu W., and Angell C. A., *Electrochem. Solid-State Lett.*, **5** (1), A26 (2001).

Xu W. and Angell C.A., Electrochem. *Electrochem. Solid-State Lett.*, **4**, E1 (2001).

Yamada A., Chung S. C., and Hinokuma K., *J. Electochem. Soc.*, **148**, 224 (2001).